12-2011

FABRICATION OF GROOVED HOLLOW FIBER MEMBRANE FOR NERVE REGENERATION: PROCESS MODELING AND PERFORMANCE EVALUATION

Jun Yin
Clemson University, juny@g.clemson.edu

Recommended Citation

Yin, Jun, "FABRICATION OF GROOVED HOLLOW FIBER MEMBRANE FOR NERVE REGENERATION: PROCESS MODELING AND PERFORMANCE EVALUATION" (2011). *All Dissertations*. 847.
https://tigerprints.clemson.edu/all_dissertations/847

FABRICATION OF GROOVED HOLLOW FIBER MEMBRANE FOR NERVE REGENERATION: PROCESS MODELING AND PERFORMANCE EVALUATION

A Thesis
Present to
the Graduate School of
Clemson University

In Partial Fulfillment
of the Requirements of the Degree
Doctor of Philosophy
Mechanical Engineering

---

by
Jun Yin
December 2011

Accepted by:
Dr. Yong Huang, Committee Chair
Dr. Nicole Coutris
Dr. Philip J. Brown
Dr. Gang Li
Dr. Richard Miller

ABSTRACT

Nerve injury is a general but intractable disease in traumatic injuries, leading to a significant reduction of functions in the nervous system. Extensive efforts are made on nerve injury rehabilitation. Since the appropriate connections between neurons and their targets are necessary, guiding axonal outgrowth is an essential step for neuron outgrowth in nervous system development, functioning, and regeneration. Besides the direct surgical nerve connection, an artificial means of guiding nerve regeneration called nerve conduits is widely applied in nerve injury rehabilitation. The main function of nerve conduits is to bridge the nerve gap, to help regenerating axons across damaged regions and guide them to appropriate targets. Recently, polymeric hollow fiber membranes (HFMs) have been studied as a potential nerve conduit for nerve regeneration and repair. In order to further improve the efficiency of HFMs, micropatterns such as aligned grooves are usually introduced on the inner surface of HFMs as an effective topographical guidance cue.

The goal of this study is to fabricate HFMs with aligned grooves on the inner surface and understand their effect on nerve regeneration and repair. Consequently, there is a need, first, to carefully design the fabrication process of HFMs introducing aligned grooves on inner surface and understand the groove formation mechanism; second, to better understand the role of defined grooves on the inner surface of HFMs as topographical guidance cues promoting axonal outgrowth.

The grooved HFMs were fabricated by means of a phase inversion-based spinning technique with a smooth and annular spinneret by carefully controlling the fabrication conditions. The effects of different operating conditions were experimentally studied, and the fabricated HFMs were also characterized. In order to explain the formation of grooves on the HFM inner surface, two different instability mechanisms were introduced: a hydrodynamic or Marangoni instability and an elastic or buckling instability. The results obtained between the experimental and the theoretical studies were compared in terms of the number of grooves under different operating conditions. Then, the fabricated HFMs with textured inner surface were used as nerve conduits. The effect of the geometry of the grooved inner surface on the axonal outgrowth was studied. A numerical model describing the motion and deformation of an axon moving on the grooved HMF inner surface was developed to study the effect of substrate geometry on axonal outgrowth.

This work developed the first theoretical model for the groove formation mechanism during the HFM fabrication. In this model, the Marangoni instability was first used to investigate the onset of instability in the HFM fabrication, and the buckling of instability magnification was also studied. This work also presented the numerical simulation of axonal outgrowth on a three-dimensional substrate, where the influence of the substrate geometry was taken into account. The work covered by this thesis will help to fabricate nerve conduits for better nerve regeneration and repair.

ACKNOWLEDGMENTS

First of all, I would like to thank my advisor Dr. Yong Huang for giving me the opportunity to pursue my Ph.D. in Mechanical Engineering at Clemson University. He also brought me into this exciting research topic, where I got the training on theoretical, numerical, as well as experimental studies. He gave me strong support in research and study, and his encouragement during the research was invaluable.

I would also like to appreciate other dissertation committee: Dr. Nicole Coutris, Dr. Philip J. Brown, and Dr. Gang Li for their advice and reviewing my thesis. I also would like to thank Dr. Xuejun Wen for his preliminary experimental design and Dr. Hai Yao for his help in experimental measurements.

Next, I would like to specially thank Dr. Coutris. Her expertise throughout this research makes the completion of this thesis possible. She gave me tremendous help on the research as well as personal development, and it has been a great pleasure to work with her.

Furthermore, I would like to thank my colleagues in the lab for their thorough discussion and critical feedback to my research. Especially, their help on my experimental research gave me an easy way to improve my experimental experience.

Finally, I would like to thank my parents for their unconditional support in the hard days during my study. I really appreciate their love and understanding to my choice.

They respect my decision and teach me to insist on realizing the goal.

Thanks to all the people who gave me good memories during my Ph.D. study!

TABLE OF CONTENTS

Page

CHAPTER THREE: ONSET INSTABILITY MODEL FOR GROOVED HFMS FABRICATION……………………………..…………………………..57

LIST OF FIGURES

LIST OF TABLES

CHAPTER ONE

INTRODUCTION AND MOTIVATION

This chapter gives the introduction and background of this research. The background of the nervous system and axonal outgrowth is introduced. The effect of the nerve conduit on promoting nerve regeneration is described, while different types of nerve guidance cues are reviewed. Since the semi-permeable hollow fiber membranes (HFMs) are used as nerve conduits, the fabrication of HFMs is introduced, and the effect of different fabrication conditions on the HFM morphology and geometry is reviewed. Then theoretical mechanisms of the groove formation are proposed. The current numerical models for axonal outgrowth are also presented. The motivation of this work and the organization of the thesis are presented at the end of this chapter.

1.1 Introduction

1.1.1 Nerve structure and damage

Generally, the nervous system consists of two parts: the central nervous system (CNS) and the peripheral nervous system (PNS). The nerve is an enclosed, cable-like bundle of nerve fibers from different neurons (Fig. 1.1). The nerve is wrapped in the main epineurium, and inside the epineurium is a group of axons, each axon being covered by Schwann cells [Filler2004]. In some cases, one neuron is also called a “nerve cell”. Three parts can be defined in typical neurons and are the critical parts of the nervous system: cell body (or soma), dendrites and axon (Fig. 1.1). The soma is the center part of the neuron. It contains the nucleus of the neuron, where most proteins are synthesized. The axon and dendrites are two types of protoplasmic protrusions that extend from the soma. The dendrites of a neuron are cellular extensions with many branches, where the majority of input signals to the neuron occurs. The axon is a finer long projection from the soma, which can carry nerve signals away from the soma. The dendrites and axon are referred to as neurites, and neurons must elongate their neurites to reach their targets.

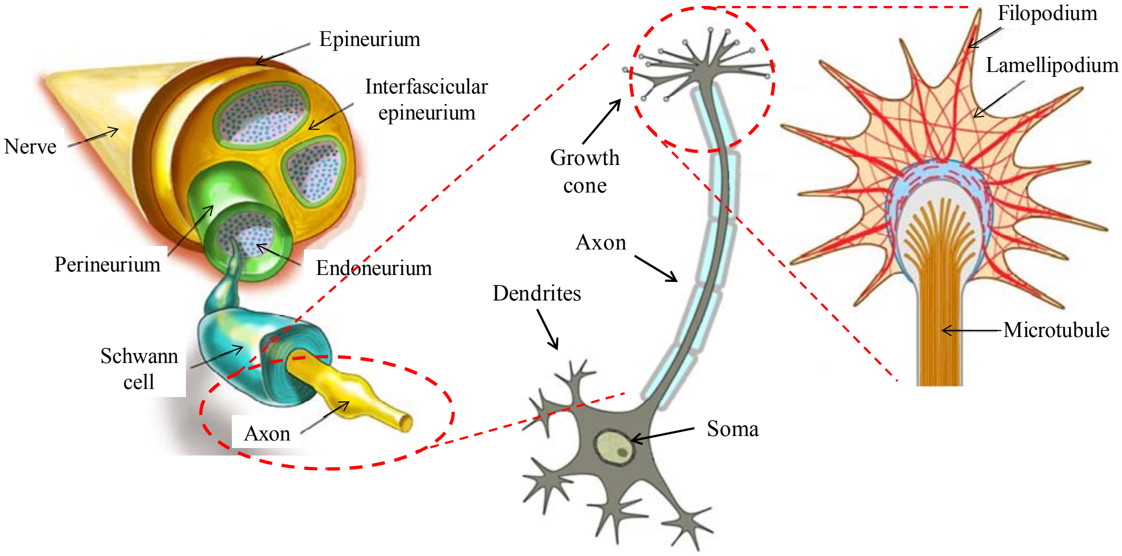

Fig. 1.1. Anatomy of nerve structure, the neuron and the growth cone (adapted from [Filler2004]).

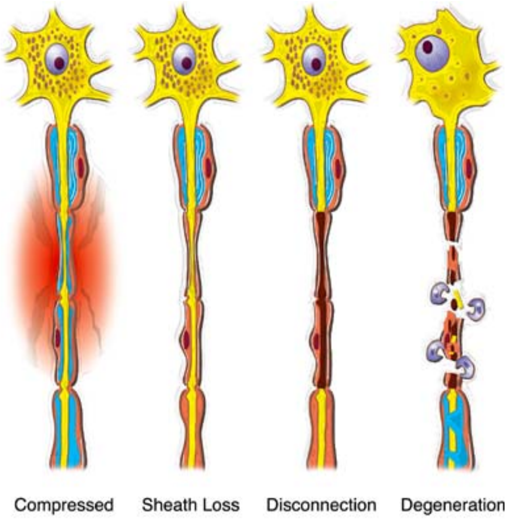

Fig. 1.2. Different types of nerve injury (adapted from [Filler2004]).

Damages to the nervous system, caused by mechanical, thermal, chemical, or ischemic factors, can impair various nervous system functions cancelling communications between nerve cell bodies and their targets. As shown in Fig. 1.2, different types of nerve injury can be classified as: compression, sheath loss, disconnection, and degeneration [Filler2004]. A simple compression on the nerve may disturb the connection of the nervous system, but the nerve can recover very rapidly; while the nerve sheath may be destroyed physically or chemically, and the recovery of this sheath loss may take a longer time. A more serious damage to nervous system is nerve disconnection, and in this case, the nervous system needs to regenerate, and the most serious nerve injury is the complete nerve transection. In this work, a nerve conduit based treatment is introduced to repair nerve breaks.

For nerve injuries, there are mainly two kinds of surgical treatments (Fig. 1.3): a direct end-to-end surgical reconnection, or the autologous nerve graft [Schmidt2003]. The direct end-to-end reconnection sutures two ends of the broken nerve cable, but it is only suitable for small defects and gaps (~3 cm) in the nerve. An autologous nerve graft method is used for longer nerve gaps, where a piece of healthy nerve is harvested from a donor site in the body, and grafted to the injured part. There exists a major drawback with autologous graft, because it partially deinnervates the donor site to reinnervate the injury site [Rutkowski2004]. Thus, bioengineering strategies, such as bridging the gap with nerve conduits are being developed to improve nerve regeneration.

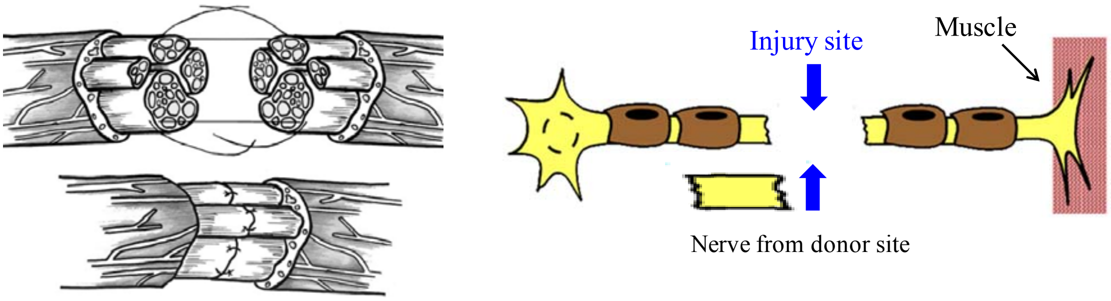

(A) (B)

Fig. 1.3. Clinical approaches for treating nerve injuries. (A) Direct end-to-end reconnection (adapted from [Schmidt2003]). (B) Autologous nerve graft.

1.1.2 Guidance cues and nerve conduit

After nerve injury, neurons most likely face a complex environment that contains different inhibitory factors. Since dense scar tissues easily form on the damaged parts, the neurites may grow to inappropriate targets and lose the correct connection in the nervous system [Zhang2005]. Therefore, to help regenerating axons cross the scar area to associated targets is a significantly important step during nerve regeneration [Long2008]. Currently, different guidance cues are found to significantly promote nerve regeneration efficiency. The guidance cues can be classified as contact-induced and chemo-induced guidance cues [Tessier-Lavigne1996]. Both contact-induced and chemo-induced guidance cues have two types: attractive or repulsive. Contact-induced guidance cues, also called topographical guidance cues, are mainly associated to nano- to micro-groove patterned substrates, such as edges, fibers, and grooves which adjust the orientation of neurons growing upon them [Zhou2009, Kofron2010]. Contact-induced guidance cues can be defined as physical guidance cues, while chemo-induced guidance cues mainly consists of chemical or biological factors. The chemical factors can be different molecules, such as neurotrophic factors, nerve growth factors, and fibroblast growth factors [Schmidt2003]. While biological factors can be Schwann cells, or astrocytes, which can promote neurite outgrowth and alignment.

Currently, bioengineering strategies associated with different kinds of guidance cues, are being developed as potential treatments to help regenerating axons across the scar area by guiding them to appropriate targets. Nerve conduits, which are usually fabricated as tubular structures, are being investigated as guidance channels to connect the gap between damaged nerves [Schmidt2003]. Such nerve conduit-based treatments for nerve injuries have the following advantages:

1. Nerve conduits allow the bridging of gaps between the cut ends and can permit the inclusion of neurotrophic factors [Vasconcelos2000];
2. Nerve conduits can provide a channel for the diffusion of growth factors secreted by the injured nerve ends and reduce the infiltration of scar tissue [Schmidt2003];
3. Nerve conduits can organize the fibrin cable and improve the outcome of peripheral and central nerve transection [Hoffman-Kim2010]; and
4. Nerve conduits can protect the nerve from the surrounding axons into the distal nerve stump [Pfister2007].

The nerve conduit essentially will serve as analogs of the extracellular matrix (ECM) to assist nerve regeneration and axonal outgrowth, while different guidance cues will significantly promote axonal outgrowth. Based on current investigations a number of researchers have concluded that the nerve conduit needs to be more than a simple tubular structure, and additional physical properties have to be incorporated for an ideal nerve conduit [Hoffman-Kim2010, Brushart1995]. As shown in Fig. 1.4, as an ideal nerve conduit, a) it should have a porous wall, which is semi-permeable; b) it should have the ability to deliver the growth factors for enhancing nerve regeneration; c) it may cooperate with supportive cells to improve neurite outgrowth; d) it can have electrical activity in order to stimulate nerve regeneration by electricity when conductive polymers are used; e) it may have multichannels in the lumen to mimic the structure of nerve fascicles; f) it may be fabricated with an oriented texture on the inner surface to improve the alignment of neurite for directional outgrowth [Schmidt2003].

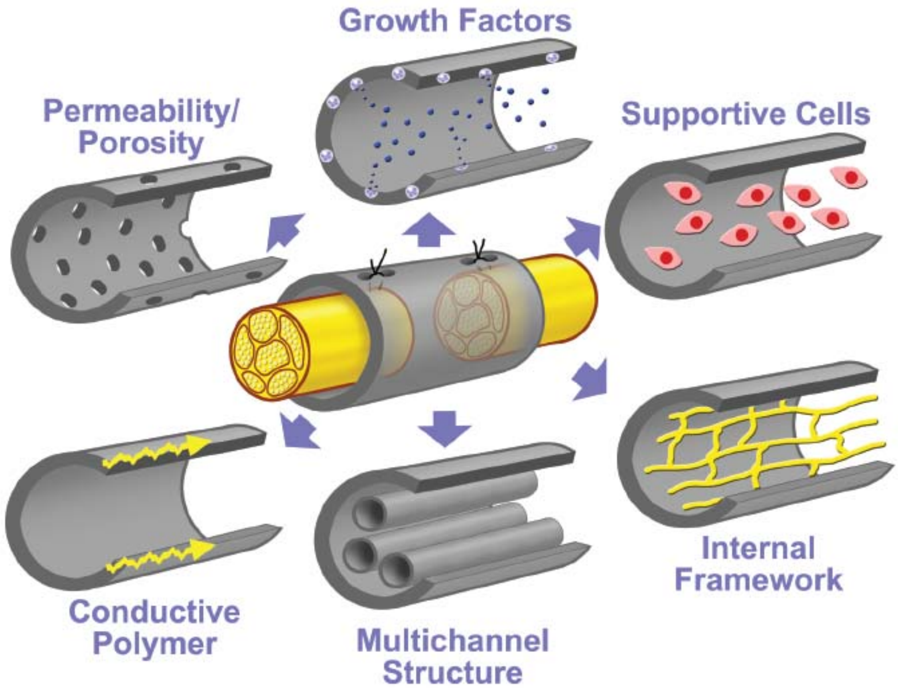

Fig. 1.4. Properties of an ideal nerve conduit (adapted from [de Ruiter2009]).

1.1.3 HFMs as a nerve conduit

One important aspect of guidance for nerve regeneration is the choice of materials for nerve conduits. Materials used to construct tubular guides can be classified into natural polymers or synthetic polymeric materials [Wang2010]. Natural polymers include materials such as collagen, chitosan, and gelatin, which have excellent biocompatibility and functions, and can reduce serious immune response. However, a lack of mechanical strength and a fast degradation *in vivo* [Wang2010] were observed for natural polymers. Thus, synthetic non-biodegradable or biodegradable polymeric materials are widely used in nerve conduit manufacturing. The latter group consists in polymer tubes made of poly($_{\mathrm{L}}$-lactide) acid (PLLA), poly(glycolic acid; PGA), polyglactin, or blends of these components. They have the advantage of degrading over time *in vivo*, and thus avoid the need for a second surgery to remove the scaffolding material [Ngo2003]. Furthermore,

1. Semi-permeable polymer conduits are more suitable than nonporous conduits, since semi-permeability allows reduction in infiltration of fibrous tissue;
2. It can increase the concentration of endogenous proteins inside the channel; and
3. It can permit or inhibit the diffusion of macromolecules between the neurons inside and the surroundings [Bregman1998, Tresco2000].

Therefore, biodegradable semi-permeable polymeric HFMs show promise in promoting axonal regeneration both *in vitro* and *in vivo* [Lu1999].

In surgical applications, fabricated nerve conduits must have the correct dimensions, and must be easy to handle and suture. Typical HFMs designed as nerve conduits usually have a diameter in the order of 1 mm, which is much larger than neurite physiological size (10 μm). For HFMs to be effective nerve conduits, different techniques have been used leading to a better orientation and outgrowth rate for regenerating neurites. For example, thin filaments (5 μm in diameter) have been assembled into HFMs to decrease HFM cross section [Wen2006], and recently, oriented assemblies of nano-fibers were also used in directing neurites [Yang2005]. An alternative approach to increase the guidance efficiency of semi-permeable HFMs is to generate aligned grooves on the inner surface of HFMs [Zhang2005, Hsu2007]. The effects of substrate topographical cues on neuron outgrowth have been extensively studied in the last decade [Rajnicek1997, Recknor2004, Johansson2006], and it was found that neurites can grow perpendicularly on the grooves to form a neurite bridge across grooves [Rajnicek1997, Goldner2006], and patterned substrates with certain groove size induces alignment and outgrowth of the chosen neuron in a particular direction associated with the pattern [Rajnicek1997, Johansson2006], improving nerve regeneration. As typical nerve conduits, HFMs are designed to bridge the gap of a sectioned nerve. For the HFM to be an effective nerve conduit, three dimensional (3D) textured micro-topology of the order of

10 μm has been introduced on the HFM inner surface to stimulate axonal outgrowth [Miller2001, Taylor2005]. It was found that aligned grooves (around 50 μm in full width of half maximum) can be formed on the inner surface of HFMs by carefully controlling the operating conditions, and such grooved HFMs have shown promising results in stimulating the rat dorsal root ganglion (DRG, a nodule on a dorsal root containing cell bodies of neurons in afferent spinal nerves) regeneration *in vitro* [Zhang2005]. Some *in vivo* studies also indicated that topography by itself, without additional biochemical cues, is capable of promoting nerve regeneration [Hoffman-Kim2010].

At the biological level, the topography of the substrate can affect [Hoffman-Kim2010]

1. The way the proteins interact with the surface and consequently the way cells bind to the surface;
2. The orientation and organization of the cytoskeleton of neuron to improve the alignment;
3. The localization of receptors, leading to different signaling behavior;
4. The shape and morphology of neurons; and
5. The gene expression in neurons, leading to behavioral and functional changes.

A great number of ideas have been proposed, but a few mathematical models have been developed that take into account different topographical mechanisms. Our goal is not to introduce the biological ideas, but to study the effect of a textured substrate on the axonal outgrowth and the dependence of the nerve regeneration on the texture from a numerical point of view based on the biological data in the literature.

1.1.4 Mechanism of axonal outgrowth

On the tip of neurites (both axon and dendrite), there is a terminal structure called growth cone. The growth cone comprises two types of protrusion: filopodia and lamellipodia (Fig. 1.1), which are full of actin. Filopodia are thin extensions that constantly initiate, extend, retract, and disappear from the growth cone periphery, while lamellipodia are sheet-like veils that are also highly dynamic, frequently initiating, extending, retracting, and disappearing between filopodia [Maskery2005].

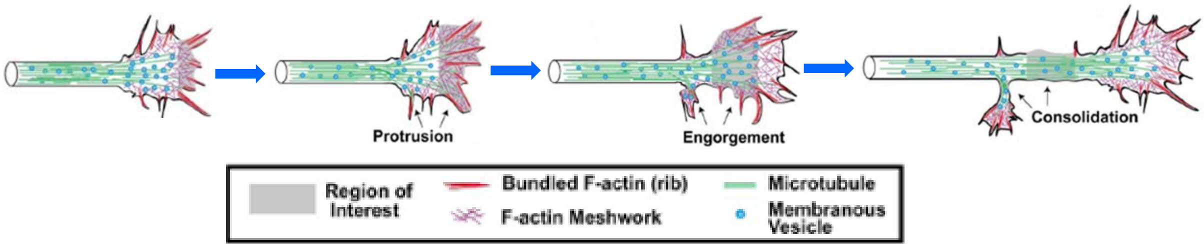

Fig. 1.5. Stage of axon outgrowth (adapted from [Dent2003]).

As a typical outgrowth process, the axonal elongation mainly can be divided into three stages: protrusion, engorgement, and consolidation (Fig. 1.5) [Dent2003, Mortimer2008, Lowery2009]. Protrusion occurs by the elongation of filopodia and lamellipodia on the growth cone, apparently through the polymerization of actin filaments [Dent2003]. Engorgement occurs due to the invasion of central domain with microtubules into extended peripheral region. Finally, a nascent axon segment becomes consolidated through the retraction of actin at the neck of the growth cone and the crosslinking of microtubules into a stable bundle [Mortimer2008]. These three continuous stages occur during the formation of nascent axons.

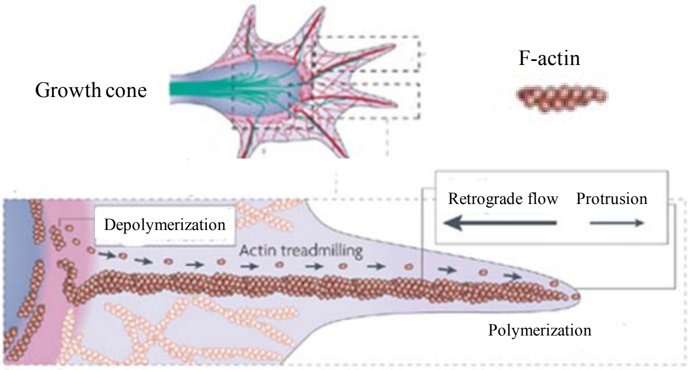

Fig. 1.6. Schematic of filopodium outgrowth (adapted from [Lowery2009]).

In the axon outgrowth process described above, a driving force of axonal elongation comes from the growth cone pulling force applied on the tip of the axon.

Therefore, the growth cone is of significant importance in both driving the axon forward, and sensing guidance cues during outgrowth. The asymmetric filopodial extension on the growth cone can steer the axonal outgrowth, which will reorientate the axonal outgrowth direction.

The filopodial structure can be featured as parallel actin filaments bundled by proteins, which constantly extend and retract. The free actin monomers, called G-actin, usually are added to the distal end of filaments as actin polymerization (the polymeric actin monomers are called F-actin); simultaneously, F-actin dissociates from the proximal end as depolymerization. The process, where the continual addition of actin subunits at the one end of an actin polymer and disassembly of the polymer at the other end, is called “actin treadmilling” [Lowery2009] (Fig. 1.6). Meanwhile, the entire actin filament is dragged back by myosin-like molecular motors into the central domain of the growth cone, which is called F-actin retrograde flow. Chan *et al.* [Chan2008] presented a model of filopodia motion based on the retrograde flow, called the “motor-clutch” model. In this model, filopodia are modeled as 1D rigid filaments, which are pulled at the end by molecular motors located in the center of the growth cone. Physical links between filopodia and the substrate are formed, which are called molecular clutches. By creating this physical coupling, filopodia are thought to experience the adhesion force from the substrate, which is regarded as a “traction force” [Ananthakrishnan2007]. The summation of all the traction forces gives a resultant force on the growth cone, which is exerted at the tip of neurites to pull the neurite forward. The traction force from the growth cone is one of the important driving mechanisms for neurite outgrowth.

1.2 State of the art

1.2.1 Fabrication of HFMs

As reviewed in [Su2007], the first artificial fibers were fabricated at the end of nineteenth century. Generally, there are several ways to prepare polymeric membranes, such as stretching, coating, and phase inversion, while most commercially available membranes are obtained by phase inversion methods [Mulder1996]. Phase inversion methods include a range of different techniques such as solvent evaporation, thermal precipitation, and immersion precipitation. The most popular technique among the phase inversion methods is the immersion precipitation, where the polymer solution is immersed into a coagulation bath containing a nonsolvent. The diffusion and convection-induced mass transfer between the solvent and nonsolvent leads to the phase separation and decomposition of the homogenous polymer solution into one polymer rich phase with a high polymer concentration, and one polymer lean phase with a low polymer concentration. Since the glass transition temperature of polymer solution increases with the polymer concentration, when the glass transition temperature reaches the ambient temperature, the polymer solution solidifies and the polymer rich phase develops into a polymer dense matrix; while the polymer lean phase develops into macrovoids. Therefore, the immersion precipitation-induced phase-inversion is a process whereby a polymer is transformed in a controlled manner from a liquid to a solid state [Mulder1996].

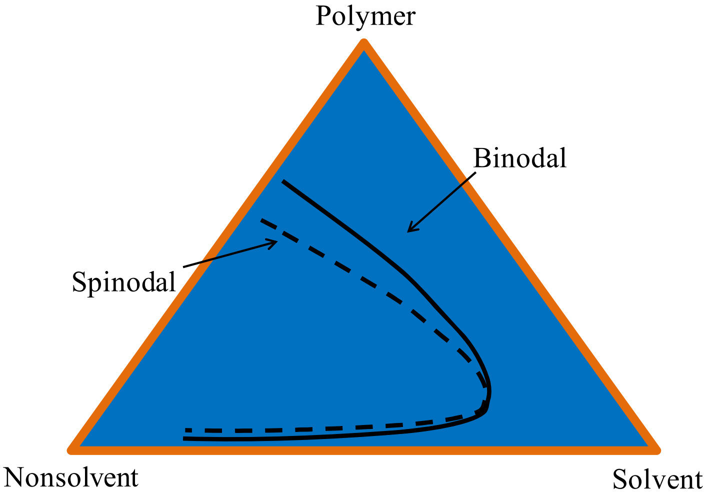

Fig. 1.7. Schematic polymer/solvent/nonsolvent a ternary phase diagram.

The relation between polymer/solvent/nonsolvent during phase inversion generally is presented by a ternary phase diagram (Fig. 1.7). In Fig. 1.7, three corners of the triangle represent the pure components, three axes stand for three possible binary combinations, and one point inside the triangle is a ternary mixture [Long2008]. There are one binodal and one spinodal lines as shown in Fig. 1.7. The phase inversion begins with a solution on the border of polymer/solvent, and the solution stays homogenous outside the binodal line. The region between binodal line and spinodal line is a metastable region [Wang2009], where liquid-liquid demixing of the polymer solution takes place. When the solution composition enters the region inside the spinodal line, rapid demixing will occur. Finally, the polymer rich phase solidifies leading to a membrane.

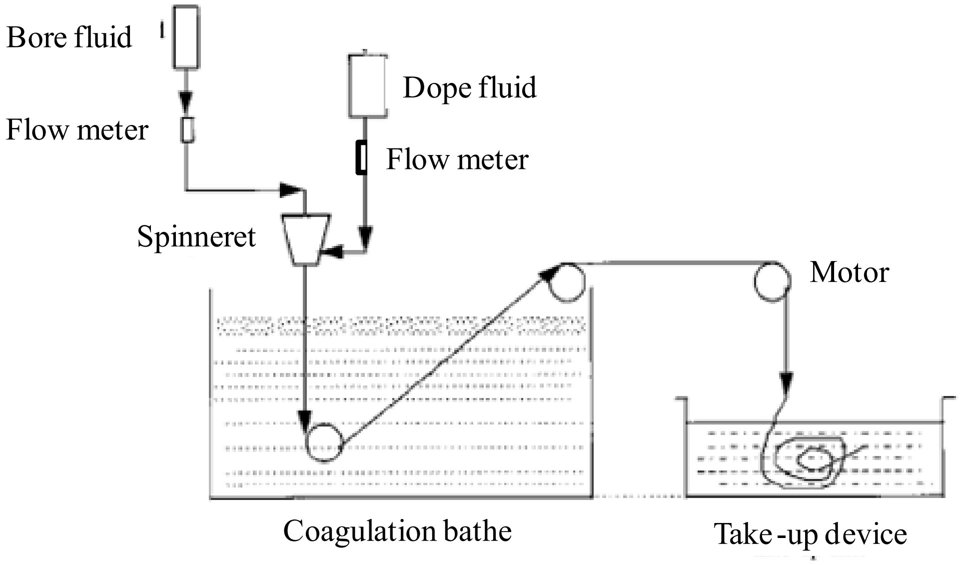

Fig. 1.8. Schematic of a commercial setup of fiber fabrication.

In the recent years, HFMs are more and more commercially utilized in various industrial processes because of the commonly recognized reason that HFMs have a larger surface area to volume ratio than flat sheet membranes. An illustration of a commercial fiber fabrication setup is shown in Fig. 1.8. There are two inflow points: one for bore fluid, the other for dope fluid (polymer solution), and two flow meters usually are used to monitor and control bore and dope flow rates. The dope and bore flows are extruded by the spinneret and enter the coagulation bath, which are full of nonsolvent. After precipitation in the coagulation bath, the solidified polymeric membrane is collected by a motor driven take-up device.

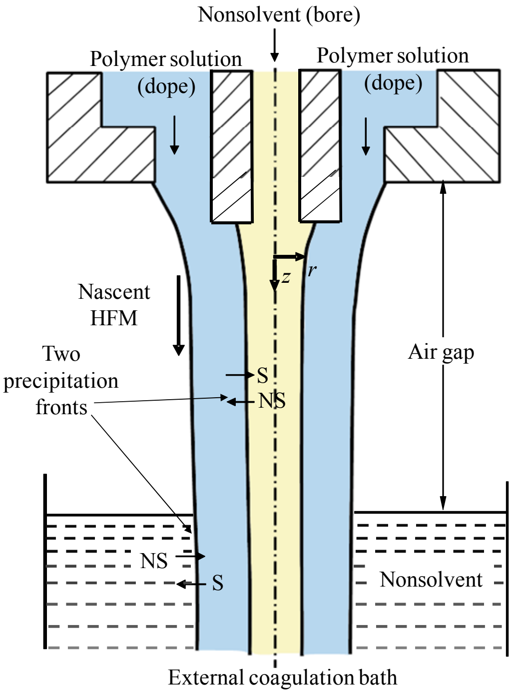

Fig. 1.9. Schematic of dry-jet wet polymer fiber spinning process (S: solvent, NS: nonsolvent).

The fabrication process of HFMs (Fig. 1.8) can be classified into two types according to extrusion and quench. If the extrudate is pure polymer without solvent, the process is called “melt” spinning, while if polymer solutions are co-extruded with one or more solvents, it is called “solution” spinning [Su2007]. For “solution” spinning process, both “wet” and “dry-jet wet” spinning can be defined based on the existence of coagulation bath in the spinning process. If the polymer solution and nonsolvent flows just pass through an air gap, do not immediately contact the coagulation bath, it is called “dry-jet wet” spinning (Fig. 1.9). If the polymer solution and nonsolvent flows enter the coagulation bath immediately after extrusion from spinneret, it is called “wet” spinning.

In the general dry-jet wet spinning process, three types of material are used: polymer, solvent, and nonsolvent. Before the spinning process, the polymer is dissolved into solvent to form the polymer solution, which will be co-extruded with nonsolvent through the spinneret. When the polymer solution contacts the nonsolvent during the air gap and in the coagulation bath, phase inversion occurs, and then the polymer solution solidifies to form a polymeric membrane. In this process, the inner nonsolvent (bore) flow induces the solvent/nonsolvent mass transfer between polymer solution and nonsolvent, resulting in the phase inversion close to the inner surface of nascent HFMs during the air gap. Meanwhile, the inner nonsolvent flow also keeps the fiber open to form hollow fibers, and contributes to the determination of the inner diameters of HFMs.

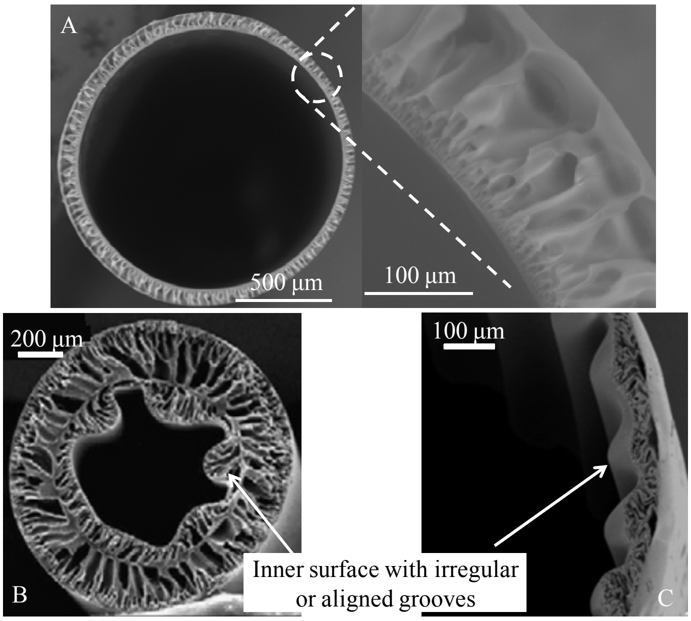

Fig. 1.10. Cross sectional view of HFM. (A) Smooth inner surface; (B) irregular [Bonyadi2007], or (C) axially grooved [Long2008] inner surface.

Generally, HFMs are fabricated using a spinning process with an annular and smooth die, but both inner and outer cylindrical surfaces can have a circular or non-circular cross section. The presence of an air gap in the setup leads to HFMs with a smooth outer surface and a smooth or a grooved inner surface depending on the fabrication conditions. HFMs with a uniformly thick wall and a smooth inner surface are shown in Fig. 1.10A, while HFMs with deformed inner surface also can be obtained under selected fabrication conditions. It is found that both irregular (Fig. 1.10B) and regular (Fig. 1.10C) deformed inner surfaces can be formed depending on the materials, experimental setup and operating conditions. HFMs, with regular deformed inner surface exhibiting aligned grooves along the longitudinal direction, are used as nerve conduits [Zhang2005].

As investigated, the groove formability and size are influenced by different fabrication conditions, such as the polymer solution flow rate, inner nonsolvent flow rate, polymer solution concentration, air gap distance, and take-up speed. Chung, *et al.* [Chung1997] studied the effect of the air gap distance on the morphology and thermal properties of polyethersulfone (PES)/N-methyl-2-pyrrolidone (NMP)/water hollow fibers. They fabricated HFMs with a deformed inner surface in the absence of air gap, and found that the deformation can be suppressed when the air gap distance increases from 0 to 14.4 cm. Shi *et al.* [Shi2007] obtained irregular inner surface in the case of poly(vinylidene fluoride-co-hexafluropropylene) (PVDF-HFP)/NMP/water HFMs. Shi *et al.* also studied the effect of NMP (solvent) added in the bore fluid, and observed a deformed irregular inner surface for a low concentration of NMP in the bore fluid. Pereira *et al.* [Pereira2000] also reported deformations and corrugations on the inner surface of poly (ether imide) (PEI)/NMP/water HFMs when NMP was added to water. Some other conditions to obtain deformed inner surface have been considered by Santoso *et al.* [Santoso2006]. They manufactured polysulfone (PSU)/NMP/water HFMs, and observed deformed HFMs with a high take-up speed, or a low bore fluid flow rate, and also found as [Shi2007, Pereira2000] that the deformation of the HFM cross section can be obtained by decreasing the concentration of NMP in bore fluid (NMP/water mixture). A more extensive study on the effect of operating conditions on the HFM geometry was carried out by Bonyadi *et al*. [Bonyadi2007], who considered the effects of air gap distance, solvent concentration in bore fluid, polymer concentration, external coagulant, and take-up speed on polyacrylonitrile (PAN)/NMP/water and PVDF/NMP/water HFMs fabrication. They obtained deformed inner surface with both regular and irregular grooves. They found a longer air gap can eliminat the deformation. While a larger take-up speed, or a lower polymer concentration was found to lead to more grooves on the HFM inner surface. They also observed that when NMP concentration increases from 0 to 60% in the bore fluid (NMP/water mixture), the groove number increased, but no grooves were observed when the NMP concentration the further increases to 80%. They showed that by replacing water with iso-propanol (IPA) as the external coagulant, the deformation of the HFM cross section can be eliminated. Zhang *et al*. [Zhang2005] also obtained regular aligned grooves on polyurethane (PU)/dimethyl sulfoxide (DMSO)/water HFMs for different polymer solution and nonsolvent flow rates. They discussed the influence of these fabrication conditions and found that the groove height increases with polymer solution flow rate but decreases with nonsolvent flow rate.

Following [Zhang2005], Long *et al.* [Long2008] worked on PU/DMSO/water HFMs fabrication, and found that more grooves formed on the inner surface of HFMs when the nonsolvent flow rate increase, or when the polymer solution flow rate or the concentration decreases.

It can be deduced from previous works that the fabrication conditions play an important role in obtaining HFMs with grooved inner texture. The different fabrication conditions need to be carefully chosen, and currently no systematic studies have been performed in order to understand the process. Furthermore, most of the works are focused on the elimination of corrugations on the inner surface of HFMs, so less effort is spent on the design of grooved geometry. In order to be used as nerve conduits, textured HFMs with defined grooves serving as topographical guidance cues on the inner surface need to be produced, therefore, the effect of different fabrication conditions on the grooved geometry as well as material properties such as material strength should be investigated.

1.2.2 Mechanism of groove formation on the inner surface of HFMs

It is well recognized that the grooves on the inner surface of HFMs are caused by process-induced instability during the fabrication. The possible process-induced instabilities can develop in the longitudinal (along the spinning direction) or in the circumferential direction. The longitudinal instability, which appears as melt fracture, draw resonance [Su2007], necking [Bonyadi2007], may lead to fiber breakage during the spinning. The circumferential instability may lead to a deformed HFM cross section, non-uniform wall thickness, or corrugated/grooved inner surface [Bonyadi2007, Long2008]. Therefore, the circumferential instability plays a critical role in groove formation on the HFM inner surface.

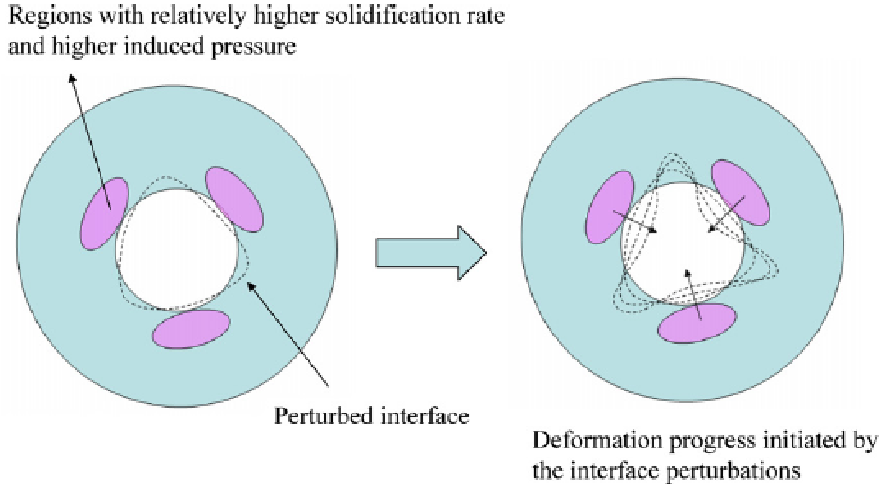

Fig. 1.11. Instability associated with proposed hydrodynamic mechanism (adapted from [Bonyadi2007]).

Bonyadi *et al.* [Bonyadi2007] recently have pioneered two different circumferential instability mechanisms for groove formation: an hydrodynamic instability (Fig. 1.11) and a buckling (Fig. 1.12). The first one is associated to the onset of instability before solidification, while the second one takes place during the solidification after the polymer solution enters the coagulation bath. As shown in Fig. 1.11, the polymer solution/bore fluid interface is perturbed and penetrates into the fluid differently depending on regions and contact area. The region with a deeper penetration and an increasing contact area can promote the solvent-nonsolvent exchange in this region, leading to a higher precipitation-induced pressure. Due to the non-uniform distribution of high penetration regions, the pressure inward will generate the deformation of HFM inner surface.

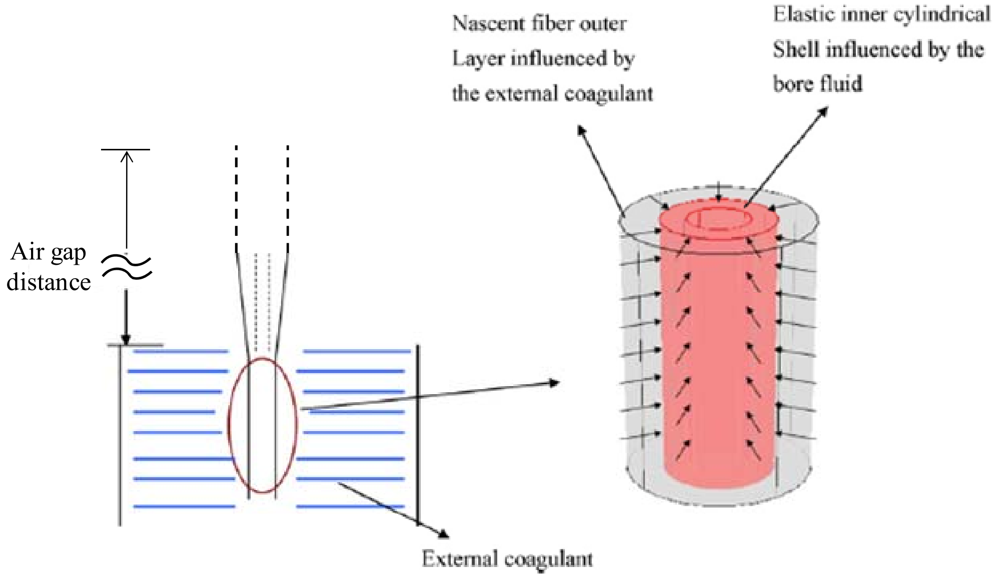

Fig. 1.12. Schematic of buckling mechanism [Bonyadi2007].

The other mechanism for groove formation is the buckling of HFMs during solidification (Fig. 1.12). Bonyadi *et al.* assumed that HFMs can be considered as a six-layer elastic shell, and postulated that an inward pressure is induced by the shrinkage of the HFM outer surface during solidification in the coagulation bath. When the inward pressure exceeds the critical buckling pressure of the inner layer of the nascent HFM, the inner surface will deform to form grooves.

However, currently no theoretical model has been presented to predict the deformation of HFMs during fabrication and to study the groove formation. Therefore, a model needs to be developed to study the groove formation process based on both hydrodynamic instability and buckling, and to investigate the effect of different fabrication conditions.

1.2.3 Modeling of axonal outgrowth

Currently, just a few numerical models can be found to simulate the axonal outgrowth on a substrate. In order to study the axonal outgrowth, the material type of the axon has to be defined first. Generally, materials can be classified based on the deformation responding to stimuli, where materials may stretch like springs, termed as elastic materials, or may flow as fluids, termed as viscous materials. Based on previous experimental studies, it is found that the axonal deformation refers both elastic stretching and viscous deformation. Under an external force, the axonal elongation response to a tensile force can be described as a viscoelastic one including three stages: first the initial elastic stretching, then the delayed stretching, and finally the elongation at a constant rate

[Dennerll1989, Lamoureux2010]. In order to model the 1D deformation of axon, a viscoelastic fluid is generally described as a series of Burgers elements (Fig. 1.13), where a spring (E_1), a Voigt element (a spring E_2 and a dashpot η_2 in parallel), and a dashpot (η) are connected in series.

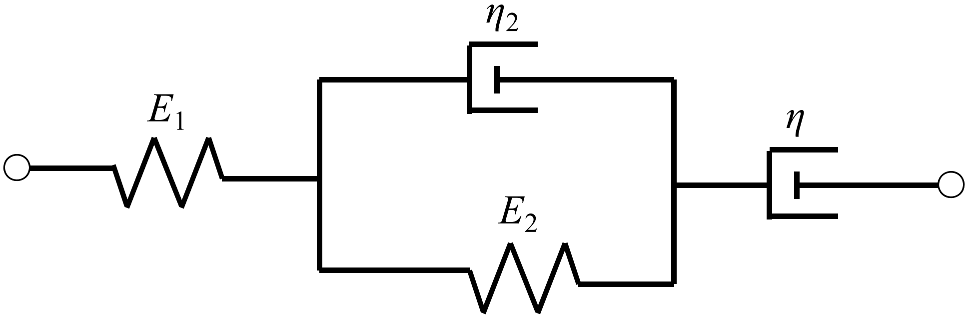

Fig. 1.13. Schematic of a Burgers element.

O'Toole *et al.* [O'Toole2008] studied the 1D axon elongation, and Aeschlimann [Aeschlimann2000] studied the two dimensional (2D) motion of an axon on a planar surface (Fig. 1.14). In the former study, the axon is modeled as a series of dashpots, and in the latter one, the axon is treated as a series of elastic segments. While the axonal elongation was modeled considering a viscoelastic fluid behavior [O'Toole2008] and a viscoelastic solid behavior [Aeschlimann2000], respectively, in both works the axon and substrate interaction was defined as a friction force proportional to the axonal velocity. As O'Toole *et al.*'s work introduced only the stretching for the axonal 1D elongation, Aeschlimann studied the stretching and bending in the 2D motion of axon on a planar surface.

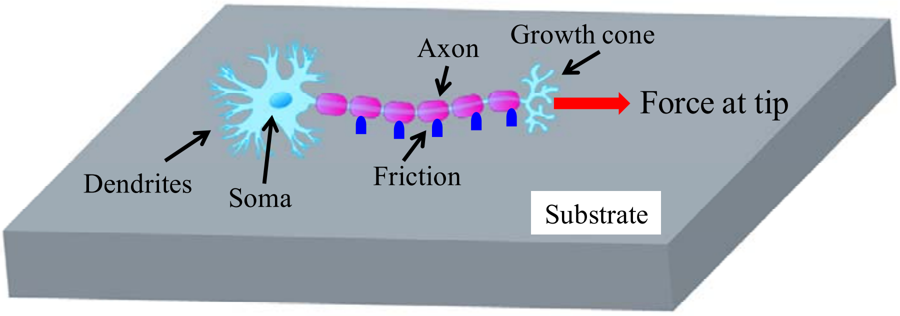

Fig. 1.14. Schematic of the axonal outgrowth on a planar surface.

Numerous experimental investigations have proved the effectiveness of the micropatterned 3D structure in promoting nerve regeneration with tubular nerve conduits [Rutkowski2004, Zhang2005, Hsu2007]. However, these two models, mentioned above, cannot be applied in the case of the axonal outgrowth on a micro-patterned 3D surface. In order to study the axonal outgrowth on the curved geometry, the 3D deformation and motion of an axon need to be taken into account in the new numerical model, where not only the stretching and bending but also the rotation of the axon will be considered. The interaction between axon and substrate also need to be improved. Based on this model, the effect of substrate geometry on axonal outgrowth can be predicted.

1.3 Motivation and goals

The main goal of this research is to manufacture HFM-based biomimetic nerve conduits with designed grooved textures on their inner surface as guidance cues to assist nerve regeneration. In order to achieve this goal,

1. There is a need to fabricate HFMs with well aligned grooves, which is the target inner structural geometry. Based on previous studies [Bonyadi2007, Long2008, Santoso2006, Pereira2000, Shi2007], grooved HFMs form during dry-jet wet solution spinning. However, most of the works focus on the elimination of grooves. Therefore, it is essential to study the effect of fabrication conditions on the HFM inner surface to control the groove geometry and the strength of the fabricated membranes.
2. A model describing the predominant mechanism leading to groove formation during HFM fabrication has to be defined. In order to manufacture HFMs with aligned grooves with a specific geometry on their inner surface, it is necessary to understand the groove formation mechanism. Based on Bonyadi *et al.*'s study [Bonyadi2007], the groove on HFM inner surface is formed due to process-induced instability: an hydrodynamic instability or a buckling. However, there is no theoretical work on the instability modeling and its characterization. Since the instability is found to be influenced by different operating conditions as well as materials, a detailed theoretical model for groove formation has to be developed.

3. A model of axonal outgrowth in the grooved nerve conduit needs to be deduced. As grooved HFMs are used in nerve regeneration as a nerve conduit, the choice of the substrate geometry and its effect on axonal elongation is a major concern. Though, experimental works [Zhang2005, Hsu2007] have been reported for neurite outgrowth on a grooved substrate, no numerical modeling has been reported to investigate the substrate geometry effect on axonal outgrowth. Therefore, the mechanism of interaction between axon and grooved substrate needs to be addressed, in order to study the axonal outgrowth on a grooved substrate. To achieve this goal, the motion of an axon on a grooved substrate described as a 3D motion of a beam on a surface has to be studied.

In this thesis, the fabrication of HFM-based nerve conduits and the axonal outgrowth have been studied theoretically, numerically and experimentally, in order to explain and control the formation of aligned grooves on the inner surface of HFMs serving as nerve conduits and also to give some understanding of the effect of the topographical guidance cue on the axonal outgrowth.

1.4 Structure of the dissertation

As shown in Fig. 1.15, this project covers different studies on the fabricated HFMs with aligned grooves on the inner surface, and on the ability of grooved HFMs as a nerve conduit to provide a solution for nerve regeneration and repair.

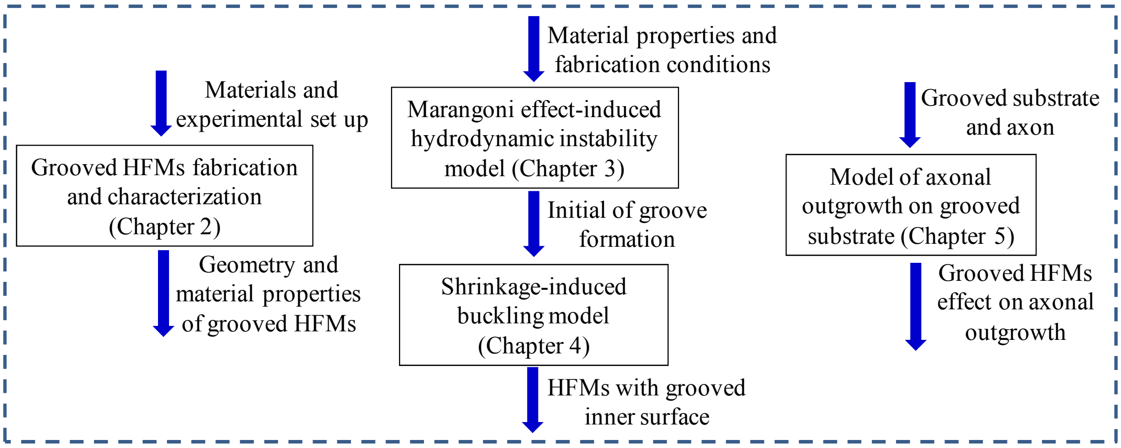

Fig. 1.15. Flowchart of the work in this thesis.

The dissertation is organized as follows. In Chapter 1, the background of HFM fabrication and characterization, and neuron outgrowth under topographical guidance cues are introduced. Then, the motivation and goal of this work are given. In Chapter 2, the experimental part of this thesis dedicated to grooved HFM fabrication and characterization under different fabrication conditions, such as air gap distance, polymer solution concentration, flow rates of polymer solution and inner nonsolvent flows is reported. The relation between fabrication conditions and HFM geometry and morphology is studied. In Chapter 3, an hydrodynamic insatiability, the first instability mechanism which may lead to groove formation, is studied. It characterizes the onset of instability and is driven by the Marangoni effect. In Chapter 4, the buckling of a multilayer structure of HFMs, the second instability mechanism, which may lead to groove formation, is theoretically modeled. The effect of an air gap distance on the groove number is accurately predicted by the model. In Chapter 5, HFMs with aligned grooves on the inner surface will be used as a nerve conduit, grooves working as a topological guidance cue. An axon is numerically modeled as a 1D Cosserat beam [Antman1995]. The interaction between axon and substrate is introduced to study the influence of substrate geometry on axonal outgrowth. Finally, Chapter 6 deals with the conclusions, and highlights the contribution and the future work.

CHAPTER TWO

HFM FABRICATION WITH GROOVED INNER SURFACE

In this work, PAN/DMSO/water HFMs are fabricated as nerve conduits using a phase inversion method, where the aligned grooves are formed due to process-induced instability. Based on the experimental observation, it is found that the geometry, morphology, and material properties of fabricated HFMs depend on different fabrication conditions, such as polymer concentration, polymer solution flow rate, nonsolvent flow rate, and air gap distance. The effect of these fabrication conditions on the texture and the strength is carefully examined in order to control the process.

The general method for HFM fabrication is the immersion precipitation-induced phase inversion [Mulder1996]. The grooved HFMs can be obtained by typical dry-jet wet spinning process (Fig. 1.9), where the polymer solution (dope) is co-extruded with an inner nonsolvent flow (bore) through the spinneret and passes an air gap before entering the coagulation bath. HFMs are obtained with deformed inner surface, including grooved textures, using smooth and annular spinnerets [McKelvey1997, Pereira2000, Santoso2006, Shi2007, Long2008]. Numerous studies have shown that the inner surface morphology is sensitive to the spinning conditions such as the air gap distance [Shi2007, Bonyadi2007], the bore fluid composition [McKelvey1997, Pereira2000, Shi2007, Bonyadi2007] and flow rate [Santoso2006, Long2008], the polymer solution composition

[Pereira2000, Bonyadi2007, Long2008] and flow rate [Long2008], the external coagulant [Bonyadi2007], and the take-up speed [Santoso2006, Bonyadi2007], to name a few. Most studies on grooved HFMs aimed to eliminate the circumferential instability to form a smooth inner surface for applications such as ultrafiltration and pervaporation. As so, few works have examined systematically the relations between the fabrication conditions and the development of circumferential instabilities. So the circumferential instabilities are studied in this chapter to control the texture of groove.

2.1 Experimental setup

2.1.1 Materials and experimental design

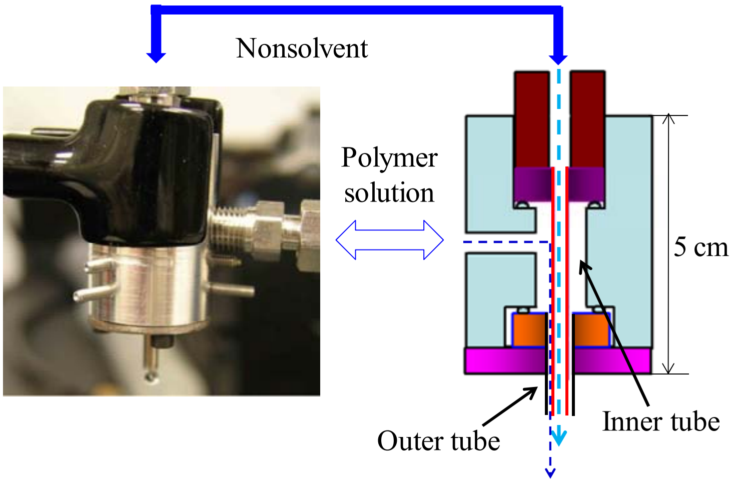

Fig. 2.1. Spinneret design.

The polymer solution (dope) was prepared by dissolving PAN (*Mw* = 150000 Da, Pfaltz & Bauer, Waterbury, CT, USA) in DMSO (Sigma-Aldrich, Milwaukee, WI, USA) through continuous stirring for 8 hours. The solution viscosity was measured using a Brookfield viscometer (DV-I prime, Brookfield Engineering, MA, USA). The bore fluid and the precipitant in the coagulation bath was deionized water.

Table 2.1. Spinning conditions of HFM fabrication

Materials	Controlled factors	Spinneret geometry
• Polymer: PAN • Solvent: DMSO • Nonsolvent: de-ionized water	• Polymer solution flow rate: 0.4-2.4 ml/min • Nonsolvent flow rate : 0.8-3.6 ml/min • Polymer concentration: 7-9 w/w% • Air gap distance: 1-20 cm	• Inner tube inner diameter: 1.4 mm outer diameter: 1.64 mm • Outer tube Inner diameter: 3.38 mm

The spinneret used in the experiments is shown in Fig. 2.1, and the characteristics of inner and outer tubes are listed in Table 2.1. No take-up speed device was used. The following fabrication conditions including the polymer solution flow rate and concentration, nonsolvent flow rate, and air gap distance were varied as shown in Table 2.1. Once fabricated, the HFMs were kept in deionized water for 48 hours to remove the residual solvent before characterization. When studying the HFM morphology and the inner surface detail in the air gap, the coagulation bath was also replaced by a bath of liquid nitrogen to fully preserve the morphology of nascent fibers as used by Tsai *et al.* [Tsai2006].

The structure and morphology of fabricated HFMs were characterized using a scanning electron microscope (SEM, S-3400N, Hitachi, Japan). Samples were prepared by fracturing fibers in liquid nitrogen before SEM testing. The mechanical properties such as the Young's modulus and fracture tensile stress of HFMs were measured using a Bose tension test machine (Electroforce 3200, Bose, MN, USA) with a crosshead speed of 10 mm/min and a clamp distance of 10 mm.

2.1.2 Grooved HFM characterization

During the spinning process, once the polymer solution and the nonsolvent (deionized water herein) are brought into contact at the spinneret outlet, the phase inversion occurs almost immediately at the nonsolvent/polymer solution interface, forming the inner surface of HFM. When the polymer solution, partly solid and partly liquid, enters the external coagulant bath, a second phase inversion occurs along the outer surface of this nascent fiber. The nascent fiber can thus be considered as a multilayer shell with inner and outer skin layers in contact with the nonsolvent. Due to the shrinkage of the outer surface induced during solidification, the newly formed elastic inner skin layer may buckle and further develop into a grooved inner surface. The formability of grooved inner surface depends on the fabrication conditions including spinneret design, fluids, air gap distance, composition of dope, and bore and dope flow rates. The influence of the air gap distance, polymer solution concentration, and polymer solution (dope) and nonsolvent (bore) flow rates for a given set up and fluids has been studied.

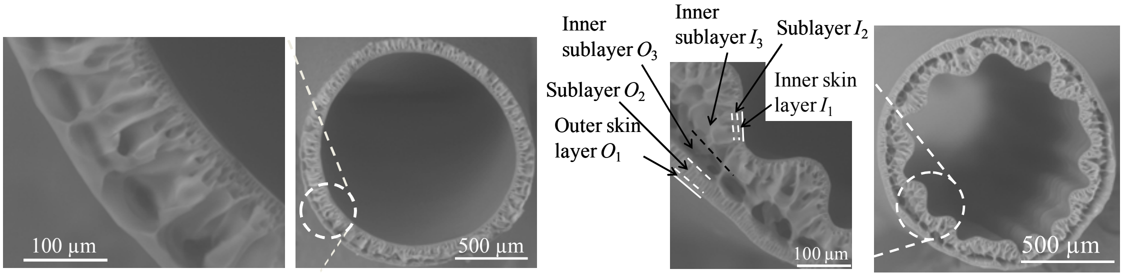

(A) (B)

Fig. 2.2. (A) HFM with smooth inner surface (nonsolvent flow rate 4 ml/min, polymer concentration 9 w/w%, polymer solution flow rate 1 ml/min, air gap 8 cm) and (B) HFM with grooved inner surface (nonsolvent flow rate 2 ml/min, polymer concentration 7 w/w%, polymer solution flow rate 1 ml/min, air gap 5 cm).

Both smooth (Fig. 2.2A) and grooved (Fig. 2.2B) HFMs can be obtained using PAN/DMSO/water by carefully controlling the fabrication conditions. As shown in Fig. 2.2B, the grooved HFMs, similar to those observed in other studies [Bonyadi2007, Machado1999], can be divided into six layers: two thin dense inner (I_1) and outer (O_1)

skin layers, two fingerlike layers (I_2 and O_2) and two spongelike layers with large macrovoids (I_3 and O_3). It should be pointed out that some layers may merge or disappear under certain fabrication conditions.

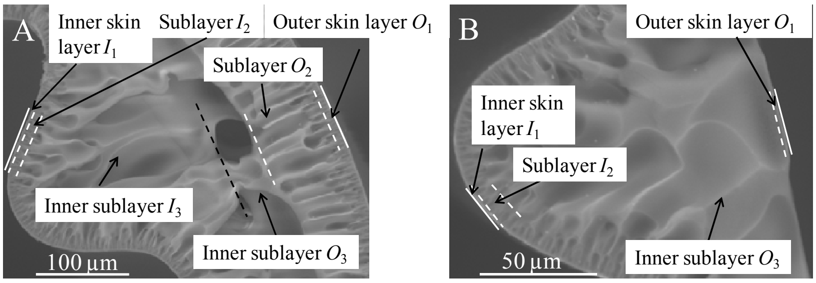

Fig. 2.3. HFMs with different morphologies at (A) polymer solution flow rate = 1.4 ml/min, and (B) polymer solution flow rate = 0.7 ml/min, and other conditions are: 9 w/w% polymer concentration, 8 cm air gap, and 2.0 ml/min nonsolvent flow rate.

As shown in Fig. 2.3, two distinct morphologies are formed under different polymer solution flow rates. There is a typical six-layer cross section with the presence of an obvious fingerlike layer (O_2) just below the outer surface when the polymer solution flow rate is high (Fig. 2.3A), and when the polymer solution flow rate is low enough, a five- or four-layer cross section is obtained(Fig. 2.3B). The inner layers in Fig. 2.3B are similar to those in six-layer morphology (Fig. 2.3A), while the fingerlike layer under the outer skin disappears. The following sections will discuss more in detail the morphology changes due to fabrication conditions.

2.2 Experimental observations

2.2.1 Groove forming region

It is of interest to fabricate HFMs with aligned grooves on the inner surface, as they can serve as nerve conduits. According to spinneret geometry and fluids properties, fabrication conditions to obtain such HFMs can be specified. It has been found that 1) Too large a polymer solution flow rate (> 3.0 ml/min) or too high a polymer concentration (> 13 w/w%) will easily block the spinneret outlet during fabrication, while too small a polymer solution flow rate (< 0.4 ml/min) and too large nonsolvent flow rate (> 10 ml/min) will reduce the HFM wall thickness, leading to broken HFMs; 2) Too small a nonsolvent flow rate (< 0.8 ml/min) will generate a small inner diameter that the inner surface may collapse with an irregular contour, while too low a polymer concentration (< 5 w/w%) will produce a very flexible membrane, which is not suitable for further measurement and applications. As shown in Fig. 2.4, a “fabrication region” in a four dimensional space built with the nonsolvent flow rate, the polymer solution flow rate, the polymer concentration and the air gap distance can be obtained based on the experimental observations. Inside this domain, a groove forming region can be delimited to define the conditions to obtain textured HFMs with regular grooves on their inner surface.

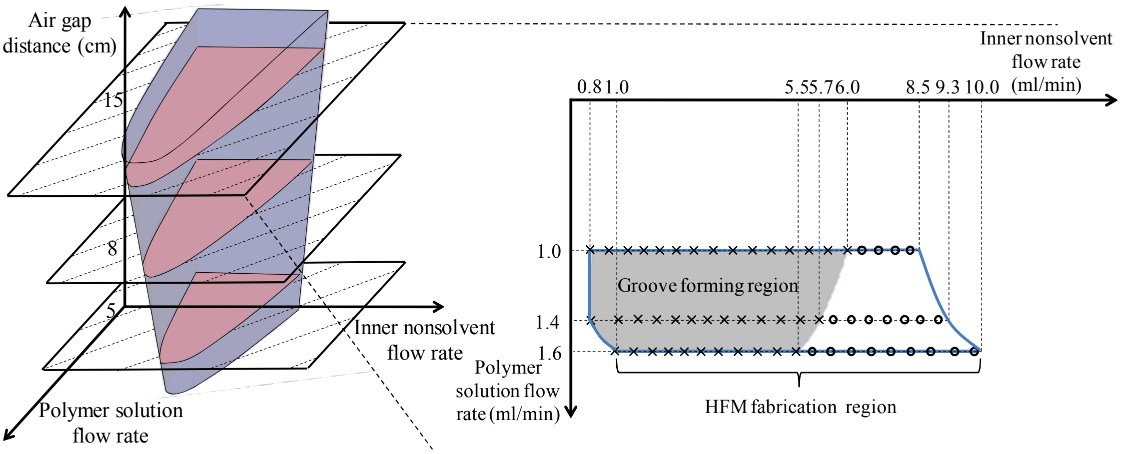

Fig. 2.4. Groove forming region (shaded) for a 9 w/w% polymer solution, under a 15 cm air gap. Points ‘x’ indicate the fabrication region of grooved HFMs while points ‘O’ the fabrication region of smooth HFMs, for a polymer solution flow rate between 1.0 and 1.6 ml/min.

For a given polymer concentration, it is possible to find a groove forming zone. It can be seen from Fig. 2.4 that under different air gap distances, grooves can be formed for nonsolvent and polymer solution flow rates falling into a specified domain, and this domain shrinks when the air gap decreases from 15 to 5 cm. Furthermore, for a short air gap less than 3 cm, the groove forming region disappears, and the inner surface of HFMs becomes smooth. Under the conditions of a 15 cm air gap and a 9 w/w% polymer concentration, the Fig. 2.4 inset further illustrates the groove forming region and its boundary inside the HFM fabrication domain. By increasing the polymer solution flow rate from 1.0 to 1.6 ml/min, the HFM fabrication region expands, whereas the groove forming region shrinks. The groove forming regions have been also obtained under different polymer solution concentrations. For a given polymer solution concentration (7, 8, or 9 w/w%), increasing the air gap distance enlarges the groove forming region.

2.2.2 Effect of air gap on groove formation

The effect of air gap was intensively investigated, for three different polymer concentrations (7, 8, and 9 w/w%), and the detailed experimental conditions and results can be seen in Table 2.2. As shown in Fig. 2.5 for a 7 w/w% polymer concentration, the HFM inner surface is smooth for a 2 cm air gap, but with increasing air gap distance the fiber becomes grooved with an increasing groove number and overall the membrane gets thinner. The groove height first increases when grooves appear, and then a longer air gap distance leads to more grooves of smaller height. A similar tendency has also been observed for two other polymer concentrations investigated (8 and 9 w/w%).

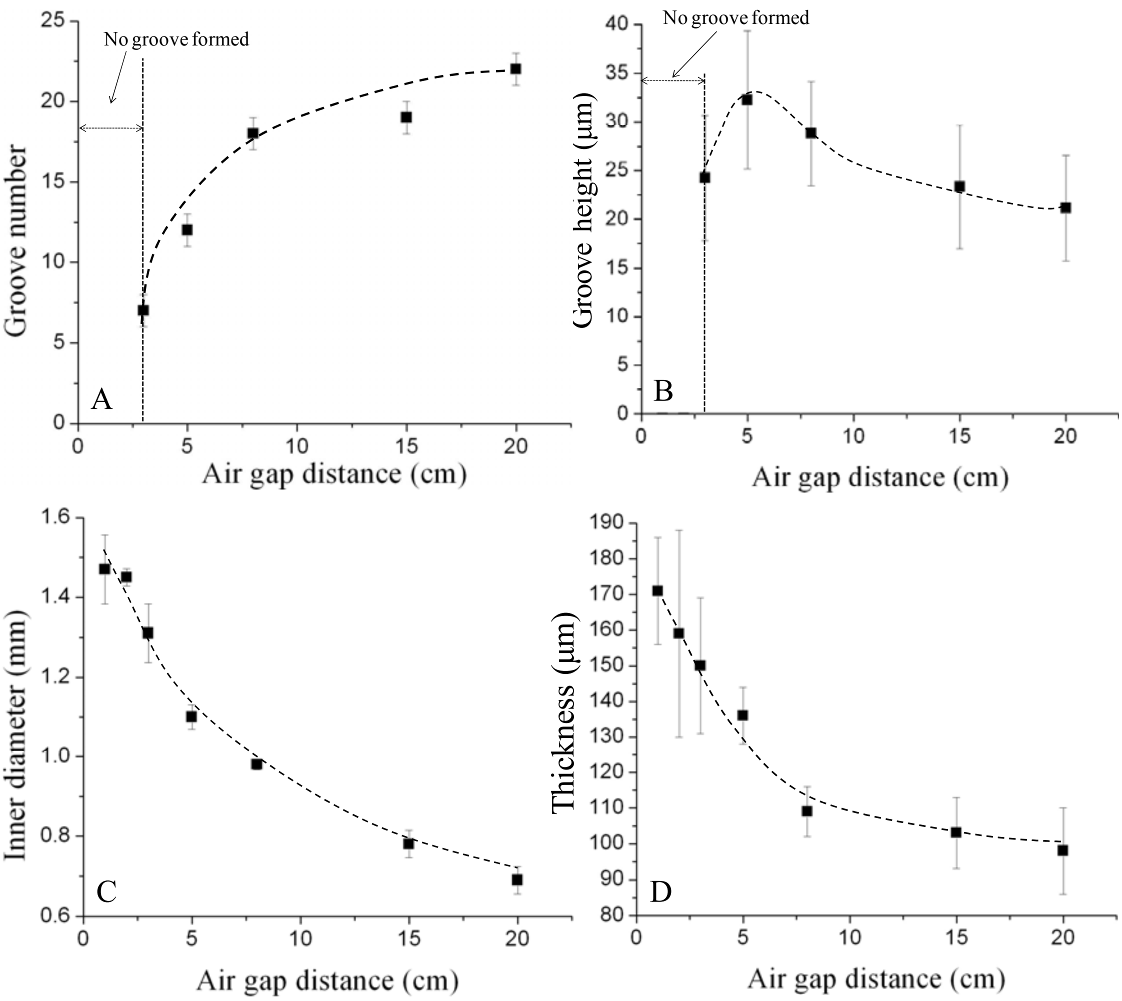

Fig. 2.5. Effect of air gap distance on (A) groove number, (B) groove height, (C) HFM inner diameter, and (D) HFM thickness (Nonsolvent flow rate 2 ml/min, polymer solution flow rate 1 ml/min, and polymer concentration 7 w/w%).

During the dry-jet wet process, the outer surface of the membrane is first exposed to humid air in the environment and then to nonsolvent in the coagulation bath. Both evaporation of solvent and intake of water vapor may occur within the air gap, leading to vapor-induced phase separation (VIPS). Since the solvent DMSO has a high miscibility with water and a low volatility [Cheng2003], the water intake due to humid air in the air gap might be apparent, and mass transfer between the polymer solution and water in the air gap may lead to phase inversion on the outer surface. This VIPS process and its role in the morphology control of HFMs were studied by Tsai *et al.* [Tsai2006] who introduced the concept of transient gel to explain the disappearance and reappearance of macrovoids close to the outer surface in case of PSU HFMs with very long air gaps up to 60 cm. The presence of the gel layer [Tsai2006] may suppress the solvent-nonsolvent exchange on the outer interface, makes the first coagulation at the inner surface predominant. Since fingerlike pores are formed mainly due to the instantaneous demixing of polymer solution, a solvent/nonsolvent combination with high affinity between each other, such as DMSO/water, is a very strong factor to form fingerlike morphology [Mulder1996]. Thus, the fingerlike morphology only forms due to a fast exchange of solvent and nonsolvent in the coagulation bath. During the air gap period, the distinct precipitation rates on the inner and outer surfaces make the morphology of HFM cross section more and more asymmetric as the air gap increases. As shown in Fig. 2.6, when the air gap distance increases, the fingerlike pore layer no longer exists close to the outer surface, the outer skin layer gets thicker, two layers have merged, and the shape of macrovoids also changes as they move closer to the outer surface.

Table 2.2. Effect of air gap distance for different polymer concentrations.

Fabrication conditions: • Polymer solution flow rate = 1.0 ml/min • Nonsolvent flow rate = 2.0 ml/min		Inner diameter (mm)	Outer diameter (mm)	thickness (μm)	Groove number	Groove width (μm)	Groove height (μm)
7.0 w/w% polymer solution concentration	Air gap (cm)						
	1	1.47±0.087	1.81±0.040	171±15	0	-	-
	2	1.45±0.022	1.77±0.036	159±29	0	-	-
	3	1.31±0.073	1.61±0.036	150±19	7±1	611±144	24±6
	5	1.10±0.031	1.37±0.024	136±8	12±1	288±15	32±7
	8	0.98±0.013	1.20±0.008	109±7	18±1	180±5	29±5
	15	0.78±0.034	0.98±0.045	103±10	19±1	134±2	23±6
	20	0.69±0.034	0.89±0.031	98±12	22±1	101±7	21±5
8.0 w/w% polymer solution concentration	Air gap (cm)						
	1	1.45±0.054	1.84±0.023	193±15	0	-	-
	3	1.40±0.051	1.78±0.036	187±48	0	-	-
	4	1.40±0.027	1.73±0.005	176±14	7±1	629±111	20±10
	5	1.20±0.032	1.48±0.030	141±8	9±1	449±33	39±6
	8	0.94±0.038	1.18±0.045	121±5	14±1	217±24	28±5
	15	0.80±0.027	1.03±0.034	113±4	18±1	146±10	25±8
	20	0.75±0.006	0.95±0.015	100±7	19±1	127±6	23±3
9.0 w/w% polymer solution concentration	Air gap (cm)						
	1	1.51±0.003	1.88±0.012	189±10	0	-	-
	4	1.46±0.014	1.80±0.011	170±12	0	-	-
	5	1.23±0.078	1.57±0.062	168±17	7±1	599±60	26±6
	8	1.10±0.076	1.41±0.056	154±24	11±2	315±81	38±10
	15	0.94±0.031	1.21±0.056	137±28	14±1	212±9	30±6
	20	0.86±0.056	1.11±0.006	127±26	15	184±12	25±7

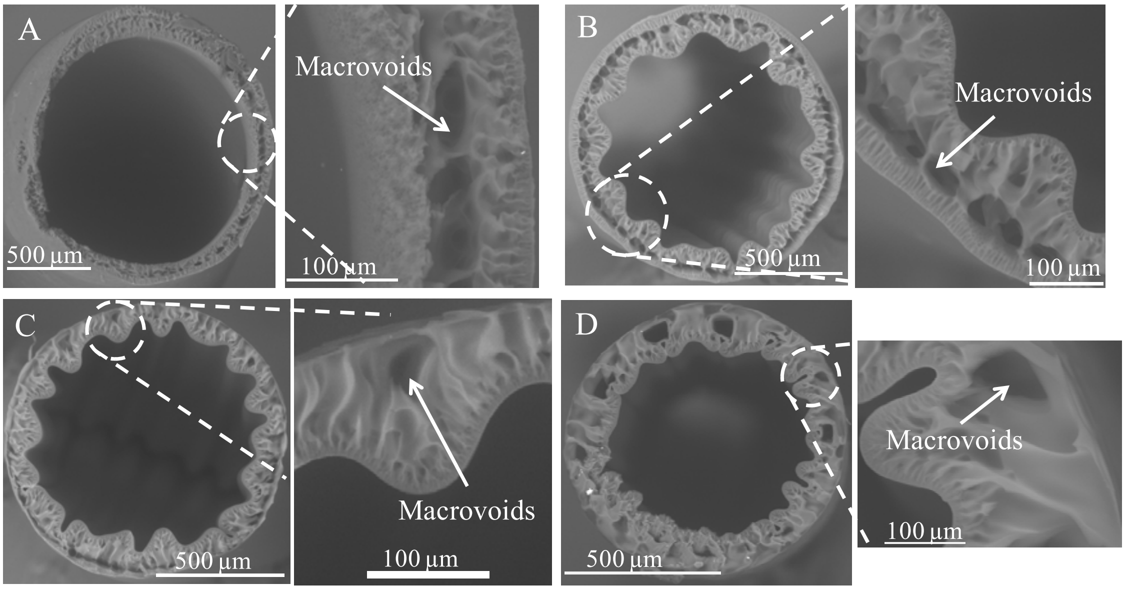

Fig. 2.6. Cross section and morphology of HFM under different air gaps distances: (A) 1 cm, (B) 5 cm, (C) 8 cm, and (D) 20 cm (7 w/w% polymer concentration, nonsolvent flow rate 2 ml/min, and polymer solution flow rate 1 ml/min).

Table 2.2 shows that the groove width decreases as the air gap increases from 3 to 20 cm. By increasing the air gap and controlling the polymer concentration and flow rates, a groove width of the order of 100 µm can be obtained. Such a groove size is suitable for nerve conduit applications [Zhang2005]. As seen from Table 2.2, by varying the air gap distance, grooves can form on the HFM inner surface and the groove size as well as the groove number can be controlled to a certain extent. It is also observed (Fig. 2.6) that when the air gap increases from 1 to 20 cm the morphology close to the inner surface has only slight variations, since the first phase inversion mainly takes place in the air gap. However, Figs. 2.6B, 2.6C and 2.6D show significant changes in the morphology close to the outer surface.

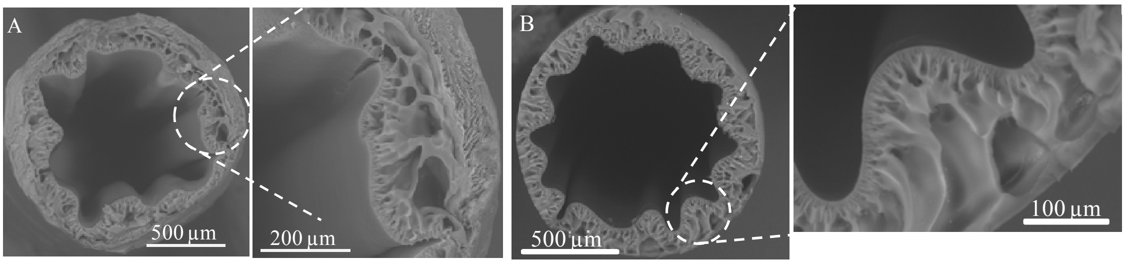

Fig. 2.7. The nascent fiber formed (A) by quenching the polymer solution in liquid nitrogen and (B) in the coagulation bath, after a 8 cm air gap. (Nonsolvent flow rate 2 ml/min, polymer solution flow rate 1 ml/min, and polymer concentration 9 w/w%).

In order to understand how the air gap influences the microstructure and what happens when the membrane enters the coagulation bath, the polymer solution was directly injected into a liquid nitrogen bath after it passed through the air gap. The fast quenching froze the fiber morphology in the air gap. By comparing the morphologies in Fig. 2.7, it can be seen that the same dense inner layer I_1 and the same fingerlike layer I_2 can be obtained, but the two middle layers with large macrovoids (I_3 and O_3) seem a little crushed in Fig. 2.7A. A significantly different morphology of HFMs quenched in liquid nitrogen is obtained close to the outer surface because no immersion precipitation takes place from the outer front during the quenching process. Similar phenomenon was also observed by Tsai *et al*. [Tsai2006]. It can be deduced that the groove formation is due to the shrinkage of outer layer resulting from either quenching or solidification, and the fingerlike pores and large macrovoids form in the air gap.

2.2.3 Effect of polymer concentration

The role of polymer concentration in HFM fabrication has been primarily studied by [Pereira2000, Bonyadi2007, Long2008]. Therefore, the different polymer concentrations were used while maintaining other fabrication conditions. The detailed results of polymer concentration effect on HFMs are listed in Table 2.3.

Table 2.3. Effect of the polymer concentration on the geometry of a textured HFM.

Fabrication conditions: • Polymer solution flow rate 1.0 ml/min • Nonsolvent flow rate 2.0 ml/min		Inner diameter (mm)	Outer diameter (mm)	thickness (μm)	Groove number	Groove width (μm)	Groove height (μm)
Polymer solution concentration	Air gap distance (cm)						
7 w/w%	8	0.98±0.013	1.20±0.008	109±7	18±1	180±5	29±5
8 w/w%		0.94±0.038	1.18±0.045	121±5	14±1	217±24	28±5
9 w/w%		1.10±0.076	1.41±0.056	154±24	11±2	315±81	38±10
7 w/w%	15	0.78±0.034	0.98±0.045	103±10	19±1	134±2	23±6
8 w/w%		0.80±0.027	1.03±0.034	113±4	18±1	146±10	25±8
9 w/w%		0.94±0.031	1.21±0.056	137±28	14±1	212±9	30±6

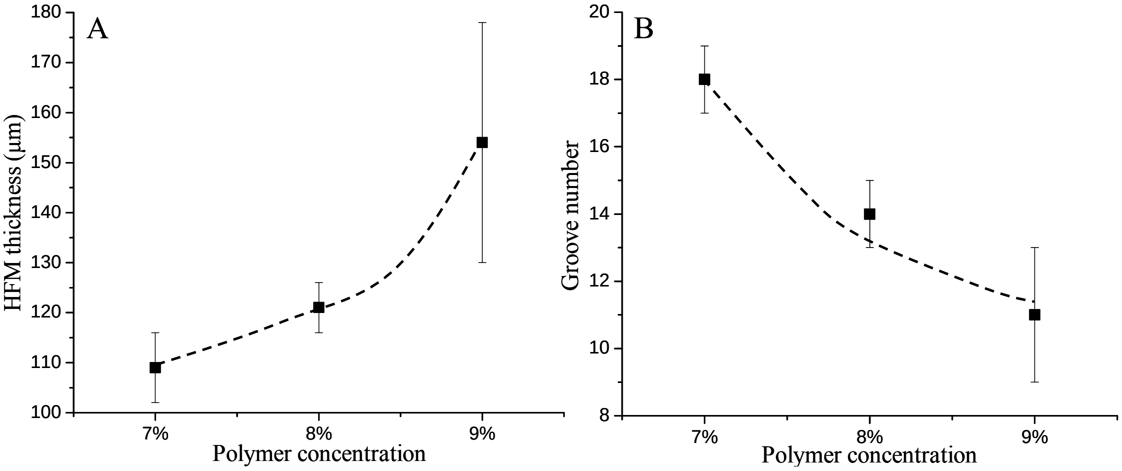

Fig. 2.8. Effect of polymer concentration on (A) HFM thickness, and (B) groove number (Nonsolvent flow rate 2 ml/min, air gap 8 cm, and polymer solution flow rate 1 ml/min).

As seen from Fig. 2.8, HFM thickness increases but the number of grooves decreases with the polymer concentration. A similar trend was also observed in previous studies [Bonyadi2007, Long2008]. The tendency to eliminate the grooves using sufficiently high concentration solutions can also be seen from Fig. 2.9.

Table 2.4. Mechanical properties of PAN HFM (inner flow rate = 2.0 ml/min, outer flow rate = 1.0 ml/min, air gap distance = 8 cm).

Polymer concentration (w/w%)	7	8	9
Polymer solution viscosity (Pa·s)	1.08	2.08	3.55
HFM Young's modulus (MPa)	23	26	32
HFM fracture tensile stress (MPa)	0.81	1.1	1.13

During the spinning process, no take-up device was used in this study, so once the polymer solution was extruded from the spinneret, it fell under its own weight. Due to gravity, surface tension and absence of die swell, HFM inner and outer diameters decrease as well as the HFM wall thickness in the air gap, so the diameters of the fabricated HFMs are smaller than the inner and outer diameters of the spinneret, respectively. As seen from Fig. 2.8A, HFMs become thicker when the polymer solution concentration is higher, so the HFM diameters are closer to the diameters of spinneret, respectively.

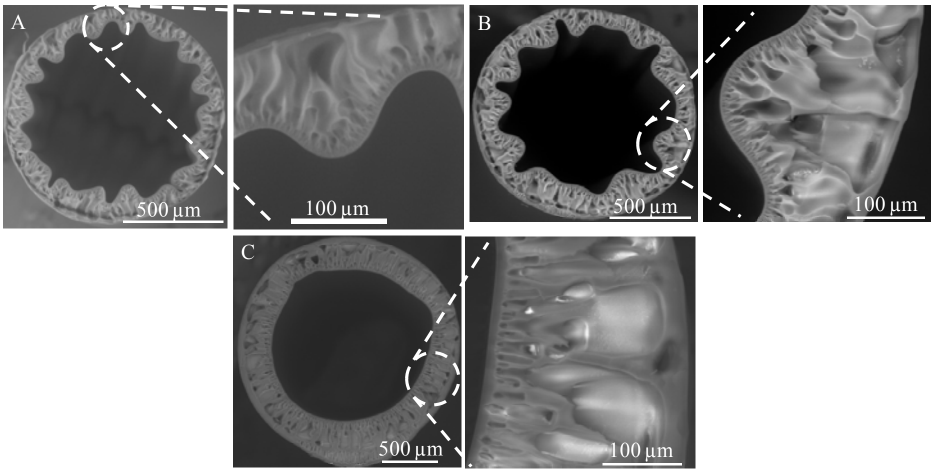

Fig. 2.9. Effect of polymer concentration on HFM morphology: (A) 7 w/w%, (B) 9 w/w %, and (C) 13 w/w% (Polymer solution flow rate 1.0 ml/min, air gap 8 cm, and nonsolvent flow rate 2.0 ml/min).

The effect of polymer concentration on HFM morphology is shown in Fig. 2.9. The membranes exhibit one very thin inner and one thin outer layers, one fingerlike layer on the inner side and one or two large spongelike layers with large macrovoids. Comparing the HFMs made using 7 w/w% (Fig. 2.9A) and 9 w/w% (Fig. 2.9B) concentrations, there is no obvious morphological difference except the HFM thickness, which is larger using the 9 w/w% solution. When the polymer concentration increases to 13 w/w% (Fig. 2.9C), the two inner and outer skin layers look similar to those of Figs. 2.9A and 2.9B except that they are thicker. The other layers have merged and long fingers separated by large macrovoids connect the inner and outer layers. Comparing the three pictures in Fig. 2.9, the membrane porosity is the highest when the lowest concentration used, which agrees with Mulder's conclusion [Mulder1996]: a less porous structure with a larger Young's modulus (Table 2.4) is obtained from a higher polymer concentration.

As grooved HFMs may serve as nerve conduits *in vivo*, it is necessary to know the strength of fabricated HFMS. Nerve conduits need to resist different kinds of external loads and protect the neurons inside. An increase in the polymer solution concentration induces an increase in the viscosity of polymer solution (Table 2.4), an increase in the membrane thickness as seen from Fig. 2.9. The Young's modulus and fracture tensile stress of HFMs increase when the polymer solution concentration increases, which indicates that the strength can be significantly improved by increasing the polymer solution concentration.

2.2.4 Effect of inner nonsolvent flow rate

When the nonsolvent flow rate increases, both HFM inner and outer diameters increase as seen from Table 2.5. Since a larger inner nonsolvent flow rate expands the lumen, the inner and outer diameters can be controlled by varying the nonsolvent flow rate, leading to designed HFM geometries for different biomedical applications. It is noted from Fig. 2.10B that with a sufficiently high nonsolvent flow rate (larger than 3.1 ml/min), grooves can be eliminated. The same phenomenon was also observed by Santoso *et al*. [Santoso2006]. Based on the observations herein, it is found that when the nonsolvent flow rate approaches the groove disappearing limit (larger than 2.7 ml/min), the groove height is significantly reduced until vanishing (Fig. 2.10C). This means that when a larger inner flow rate expands the inner surface, it also generates a circumferential tension which tends to reduce the groove height but maintains an almost constant groove number. With a further increase of the nonsolvent flow rate, the pressure due to the shrinkage of the outer layer is no longer high enough to induce the buckling of inner skin layer. As a result, the inner surface becomes smooth. Fig. 2.10A also shows the variations of inner and outer diameters as the nonsolvent flow rate increases, indicating different types of variation for the diameters of smooth and grooved HFMs.

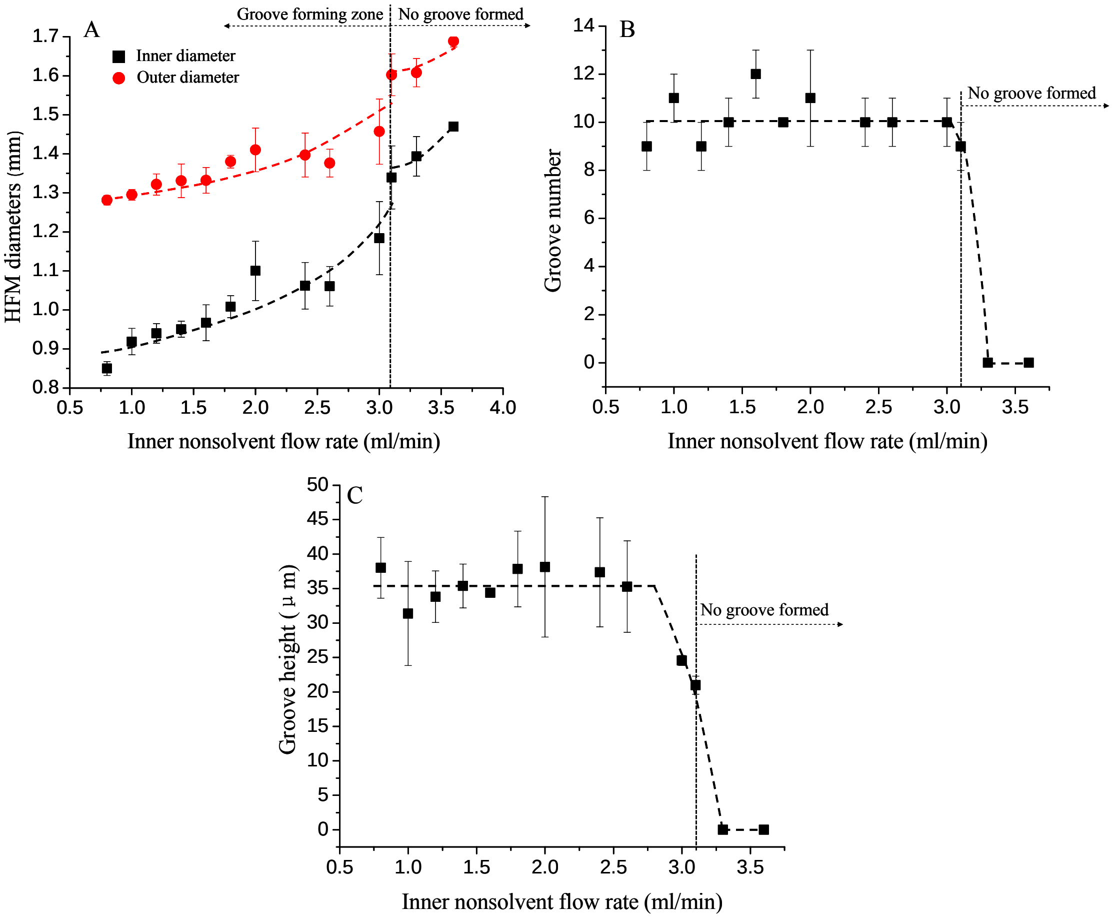

Fig. 2.10. Effect of inner nonsolvent flow rate between 0.8 to 3.6 ml/min on (A) HFM diameters, (B) groove number, and (C) groove height (Polymer solution flow rate 1 ml/min, air gap 8 cm, and polymer concentration 9 w/w%).

The differences between the structures of smooth and grooved HFMs using different nonsolvent flow rates can be observed in Figs. 2.2A and 2.7B. Increasing the nonsolvent flow rate leads to a decrease in the thickness and a more asymmetric membrane. The macrovoids of the inner sublayer are closer to the inner surface and are inward pointed, whereas a layer of ellipsoidal macrovoids appear close to the outer surface.

Table 2.5. Effect of inner nonsolvent flow rate.

Fabrication conditions: • Air-gap: 8 cm • 9.0 w/w% polymer solution concentration		Inner diameter (mm)	Outer diameter (mm)	Thickness (µm)	Groove number	Groove width (µm)	Groove height (µm)
Polymer solution flow rate: 1.0 ml/min	Inner nonsolvent flow rate (ml/min)						
	0.8	0.85±0.017	1.28±0.012	216±3	9±1	287±13	38±4
	1.0	0.92±0.032	1.30±0.017	188±5	11±1	255±11	31±8
	1.2	0.94±0.025	1.32±0.027	191±28	9±1	317±24	34±4
	1.4	0.95±0.021	1.33±0.043	190±24	10±1	310±24	35±3
	1.6	0.97±0.046	1.33±0.033	182±19	12±1	261±16	34±1
	1.8	1.01±0.028	1.38±0.016	186±17	10	317±9	38±5
	2.0	1.10±0.076	1.41±0.056	154±24	11±2	315±81	38±10
	2.4	1.06±0.060	1.40±0.056	167±11	10±1	346±33	38±8
	2.6	1.06±0.051	1.38±0.035	157±15	10±1	326±50	35±7
	3.0	1.18±0.094	1.46±0.084	137±7	10±1	376±68	25±1
	3.1	1.34±0.081	1.60±0.054	131±19	9±1	488±56	21±1
	3.3	1.39±0.051	1.61±0.036	107±8	0	-	0
	3.6	1.47±0.009	1.69±0.014	110±3	0	-	0

2.2.5 Effect of polymer solution flow rate

The polymer solution flow rate mainly influences the HFM thickness. As shown in Table 2.6, the HFM wall thickens when the polymer solution flow rate increases, which indicates an efficient way for controlling the HFM thickness. The groove number decreases when the polymer solution flow rate increases, and the grooves may even disappear when the polymer solution flow rate is high enough (Fig. 2.11B), showing the boundary of the groove forming region. Comparing the groove number tendencies in Tables 2.5 and 2.6 (under different dope and bore flow rates), it can be concluded that the groove number is determined easily by the polymer solution (dope) flow rate. Within the groove forming region, varying the nonsolvent (bore) flow rate does not obviously change the groove number. The decrease of the groove number due to the increased polymer solution flow rate has been also observed by Long *et al.* [Long2008].

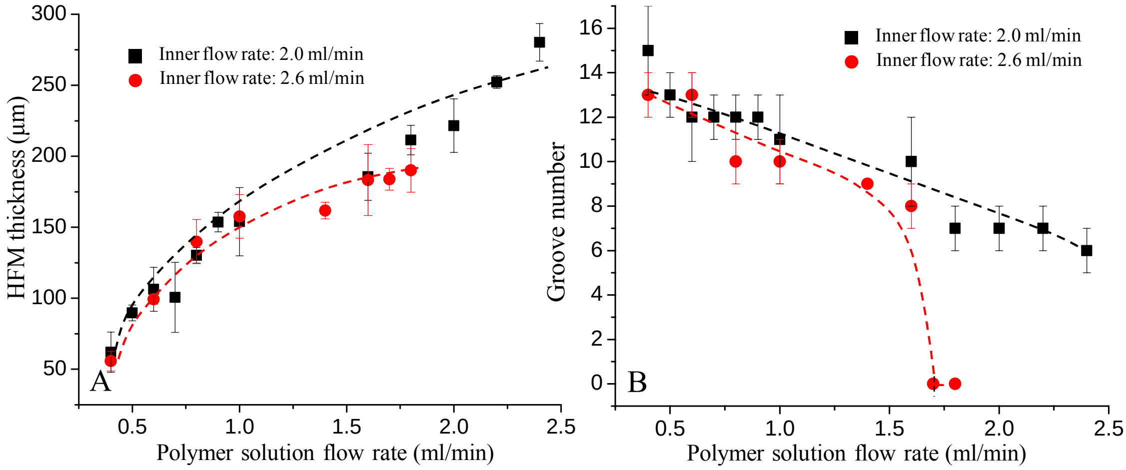

Fig. 2.11. Effect of polymer solution flow rate (A) HFM thickness, (B) groove number (nonsolvent flow rate 2 and 2.6 ml/min, air gap 8 cm, polymer concentration 9 w/w%).

Table 2.6. Effect of polymer solution flow rate.

Fabrication conditions: • Air-gap: 8 cm • 9.0 w/w% polymer solution concentration		Inner diameter (mm)	Outer diameter (mm)	Thickness (μm)	Groove number	Groove width (μm)	Groove height (μm)
Inner nonsolvent flow rate: Case 1: 2.0 ml/min	Polymer solution flow rate (ml/min)						
	0.4	1.17±0.120	1.29±0.092	62±14	15±2	262±63	16±9
	0.5	1.12±0.111	1.30±0.100	90±6	13±1	278±35	19±4
	0.6	1.12±0.068	1.33±0.046	106±15	12±2	279±33	32±6
	0.7	1.03±0.076	1.23±0.093	100±25	12±1	262±28	29±8
	0.8	1.03±0.065	1.29±0.054	130±6	12±1	265±48	40±6
	0.9	0.99±0.013	1.29±0.013	154±7	12±1	259±21	37±7
	1.0	1.10±0.076	1.41±0.056	154±24	11±2	315±81	38±10
	1.6	1.06±0.062	1.43±0.075	186±17	10±2	351±77	45±1
	1.8	1.21±0.034	1.63±0.045	211±10	7±1	522±53	32±4
	2.0	1.25±0.034	1.69±0.065	222±19	7±1	590±52	36±4
	2.2	1.20±0.008	1.71±0.008	252±4	7±1	569±51	31±7
	2.4	1.21±0.048	1.77±0.067	280±13	6±1	606±66	36±1
Inner nonsolvent flow rate Case 2: 2.6 ml/min	Polymer solution flow rate (ml/min)						
	0.4	1.18±0.033	1.29±0.045	56±7	13±1	279±13	13±2
	0.6	1.05±0.070	1.25±0.062	99±3	13±1	256±36	24±4
	0.8	1.13±0.075	1.41±0.030	140±16	10±1	355±24	30±9
	1.0	1.06±0.051	1.38±0.035	158±15	10±1	326±50	35±7
	1.4	1.17±0.063	1.50±0.065	161±6	9	410±22	37±5
	1.6	1.14±0.112	1.50±0.041	183±25	8±1	454±101	39±15
	1.7	1.44±0.023	1.81±0.021	184±7	0	-	0
	1.8	1.43±0.027	1.81±0.024	190±15	0	-	0

Two different HFM morphologies (Fig. 2.3) were obtained using two different polymer solution flow rates (1.4 vs. 0.7 ml/min). There is a pronounced difference between these two structures: the six-layer cross section with the presence of a fingerlike layer just below the outer skin layer when the polymer solution flow rate is high, and a four-layer cross section with a different morphology close to the outer skin layer. During dry-jet wet spinning, precipitation occurs first close to the inner surface then the outer surface when a nascent fiber first passes through the air gap and then enters the coagulation bath. Two coagulation fronts move in opposite directions and meet each other forming the spongelike layer of ellipsoidal macrovoids as seen in Fig. 2.3A. With a lower polymer solution flow rate, the duration between the first and second coagulations is longer, and the inner front moves further into the HFM wall. As a result, the fingerlike pores are longer. All of these lead to an asymmetric membrane as seen in Fig. 2.3B.

2.3 Summary

This chapter presents a method to fabricate textured PAN HFMs, with aligned grooves formed on the inner surface by a dry-jet wet spinning process under certain fabrication conditions. The grooves were found to be formed due to process-induced instability. The effects of the four parameters fixing the fabrication conditions: air gap length, polymer solution concentration, polymer solution and nonsolvent flow rates were systematically studied. A groove forming region is defined for different combinations of fabrication conditions, where HFMs with aligned grooves on the inner surface are obtained. The geometry, morphology and mechanical properties of HFMs have been characterized in terms of the four parameters, and have been analyzed to design textured HFM for specific applications. Specifically, within the groove forming region, the number of grooves increases with the air gap distance between 1 and 20 cm. The number of groove decreases with the polymer solution concentration and flow rate. The groove number was found to not be sensitive to the inner nonsolvent flow rate.

CHAPTER THREE

ONSET INSTABILITY MODEL FOR GROOVED HFMS FABRICATION

The fabrication of HFMs with grooved inner texture is presented in last chapter. The aligned grooves on the inner surface of HFM are generally considered to be formed due to the process-induced instability in the circumferential direction. Bonyadi *et al.* [Bonyadi2007] recently have pioneered two different instability mechanisms for groove formation: hydrodynamic instability and buckling, which are based on two assumptions: 1) the hydrodynamic instability happens during mass transfer and phase separation before solidification, and is the onset of instability during the HFM fabrication; and 2) the buckling is the magnifying solidification step for the development of a non-uniform cross section of hollow fibers.

In this chapter, the hydrodynamic instability will be discussed first. The driving mechanism for hydrodynamic instability is the existence of interfacial tension gradients associated to polymer concentration variations, and is called the Marangoni effect. For the first time, the Marangoni instability is used to explain the formation of axially and internally grooved HFMs. The theoretical predicted results are then compared with the experimental results obtained for PU/DMSO/water [Long2008], the Marangoni instability having enough time to develop. However, it is found that the hydrodynamic instability is not the predominant mechanism of groove formation for PAN/DMSO/water HFMs.

3.1 Role of Marangoni instability in groove formation

The interfacial instability between two immiscible liquid phases has been widely studied. When a third component diffuses between two immiscible liquid phases, the interface may become unstable, and spontaneous convection sets in [Sørensen1977]. A theoretical understanding of the interfacial instability observed during mass transfer across an interface has been developed by Sternling and Scriven [Sternling1959] who reported high fluctuations in the vicinity of the interface (also known as interfacial turbulence) between two incompressible fluid phases which in some cases accompany mass transfer. The essence of their explanation is that the interfacial instability is due to concentration-induced variation of interfacial tension, known as the Marangoni effect, but they assumed no deformation of the interface. Hennenberg and Sørensen *et al.* [Sørensen1977, Hennenberg1977] have carried out a stability analysis on isothermal, deformable interfaces with transfer of surface-active substances. They formulated the balance laws for a moving and deformable interface in local equilibrium with immiscible bulk liquids in which a third component is distributed. Von Gottberg *et al.* [von Gottberg1995] studied interfacial instabilities due to a chemical reaction, which is taking place at the interface. The stability of the system was examined with respect to small perturbations with the normal mode method. Slavtchev *et al.* [Slavtchev2006] studied Marangoni instability in partially miscible liquid-liquid systems in the presence of surface-active solutes. The surface-active solute, soluble in both phases, is transferred across the interface between the two liquids, introducing interfacial tension gradients which drive a solutal Marangoni instability. In all these works, a linear stability analysis was carried out to study the condition of stability and the influence of different parameters such as the diffusivity ratio and the viscosity ratio of the two phases.

Marangoni instability [Davies1963] is known as an interfacial instability driven by interfacial tangential forces due to interfacial tension gradients. Solvent extraction introduces concentration gradients in the solution which lead to these interfacial tension gradients. An interfacial instability can cause the inner surface pattern of HFMs and the number of forced grooves depends on the wavelength of the most dangerous wave. In the present study, it is assumed that the groove formation occurs during the solvent extraction process and is due to the onset of an instability developing at the interface. Consequently, phase inversion and/or solidification-induced shrinkage effects are decoupled from the Marangoni instability. Mass transfer starts with the spontaneous extraction of solvent between the two immiscible phases: polymer solution and nonsolvent. Then the nonsolvent invades the solution. In order to study the onset of instability, only the solvent extraction process is considered.

3.1.1 Modeling assumptions

In general HFM fabrication, two flows, polymer solution and nonsolvent, discharge from the spinneret together through the air gap (Figure 1.9). Once these two flows are brought into contact in the air gap, several steps occur: first a spontaneous extraction of the solvent from the polymer solution, then an invasion of the polymer solution by the nonsolvent leading to phase inversion in the ternary mixture polymer/solvent/nonsolvent and solidification. The interfacial instability is supposed to occur during the first step of the process [Cohen Addad1999]. Different assumptions are considered for this first step and summarized as follows:

1. The time scale of the first step, extraction of the solvent, is smaller than the characteristic diffusion time t_0 associated to the interfacial region estimated as 1 ms (thickness of the zone 1 μm and diffusivity 5×10^{-10} m^2/s) and smaller than the characteristic advective time associated to the vertical flows of the two phases of the order of 0.1 s (volume flow rate 4 ml/min for a 1 mm diameter). The two phases are assumed at rest, and consequently for the onset of instability, the basic solution is the

classical diffusion solution when two incompressible semi-infinite fluid layers are in contact along a deformable interface;

2. During the first step, only the solvent mass transfer is considered. Therefore, polymer solution and nonsolvent can be treated as two immiscible liquid phases while the solvent is transferred across the interface;
3. Thermal and rheological effects are neglected; and
4. The region of interest is located close to the interface. Its thickness of the order of 1 μm is far smaller than the inner radius or/and the thickness of the HFM, so the problem can be studied in a 2D rectangular geometry with two semi-infinite layers on each side of a planar interface. This assumption is validated by the simulation results that the wavenumber of the most dangerous wave is $k \sim 0.3$, and the associated wavelength is far larger than the length scale.

3.1.2 Problem formulation

Consider a 2D system of two semi-infinite layers of a polymer solution, phase 2, in contact with a nonsolvent, phase 1, along an interface. The governing equations of mass, momentum and solvent diffusion are written in both phases as:

$$\nabla \cdot \vec{v}_i^* = 0 \tag{3.1}$$

$$\rho_i \left(\frac{\partial \vec{v}_i^*}{\partial t^*} + \vec{v}_i^* \cdot \nabla \vec{v}_i^* \right) = -\nabla p_i^* + \mu_i \nabla^2 \vec{v}_i^* \tag{3.2}$$

$$\frac{\partial c_i^*}{\partial t^*} + \vec{v}_i^* \cdot \nabla c_i^* = D_i \nabla^2 c^*_i \tag{3.3}$$

where $\vec{v}_i^*$ is the velocity, c_i^* the solvent concentration distribution, p_i^* the pressure, ρ_i the density, μ_i the viscosity, and D_i the solvent diffusivity in phase *i* (*i* = 1 for nonsolvent, and *i* = 2 for polymer solution). It should be pointed out that variables with a superscript "*" are dimensional. The densities, viscosities and diffusivities of each phase are assumed to be constant.

The fluid domain is divided into three regions, as shown in Fig. 3.1, the two bulk regions separated by the third one which is a thin adsorption layer adjacent to the interface, the adsorbed polymer layer. The solvent transfer is due to diffusion in each bulk up to the adsorption layer and due to adsorption-desorption of polymer inside the adsorption layer in phase 2. Polymer adsorption is a reversible process, but polymer desorption is a very slow process [Somasundaran2006], whose characteristic time is far larger than the diffusion time t_0. It is assumed that only adsorption is concerned herein.

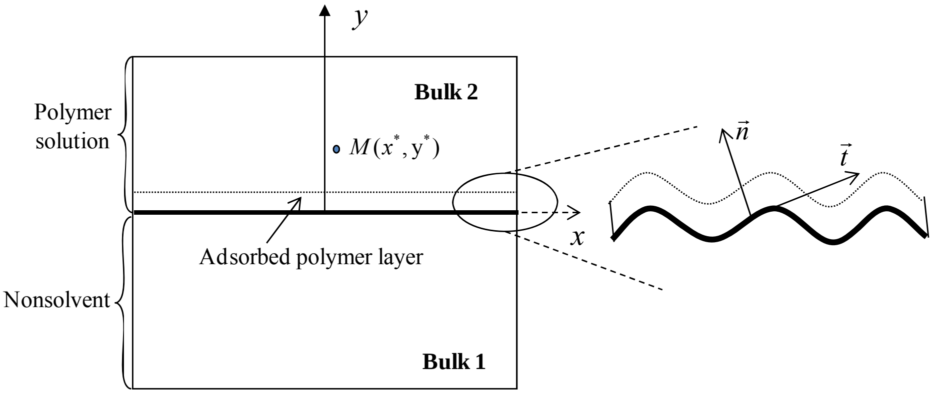

Fig. 3.1. The fluid domain with the unperturbed interface between two phases: nonsolvent and polymer solution (the inset shows the perturbed adsorbed polymer layer).

The Langmuir model is used to describe a polymer adsorption coupled with bulk diffusion [Somasundaran2006]. The interfacial excess polymer concentration Γ^* is expressed in terms of the concentration of polymer $c^*_{p/s}$ in the solution evaluated just above the interface:

$$\Gamma^* = \Gamma_{\max} \frac{K^l c^*_{p/s}}{1 + K^l c^*_{p/s}} \tag{3.4}$$

where $\Gamma_{\max}$ is the maximum interfacial polymer concentration and K^l the Langmuir equilibrium constant measuring the ability to adsorb. The interfacial tension σ^* depends on the polymer concentration and this dependence is expressed by the Langmuir-Szyskowski isotherm:

$$\sigma^* = \sigma^*_{solv} - \frac{RT}{M_w} \Gamma_{\max} \ln\left(1 + K^l c^*_{p/s}\right) \tag{3.5}$$

where σ^*_{solv} is the interfacial tension of pure solvent, T the absolute temperature, R the gas constant, and M_w the molecular weight of the polymer. Eq. (3.5) shows the drop of the interfacial tension due to the presence of a polymer such as PU in a solvent DMSO and the surfactant property of the polymer. However, in case of PAN/DMSO/water system, it was found that the interfacial tension between water (nonsolvent) and the polymer solution just slightly depends on PAN concentration [Weh2004].

3.1.3 The basic solution

During the solvent extraction, the concentration profiles in each phase are obtained from the diffusion equations, the bulk fluid being considered at rest with a planar interface. The diffusion time scale t_0 is assumed far larger than the advective time scale associated with the perturbation. Consequently, the concentration profiles are frozen at time t_0 to study the perturbation as considered by Sterling and Scriven [Sterling1959]. The solvent concentrations $c_i^{*(0)}$ are solutions of the 1D diffusion equations in two semi-infinite domains:

$$\frac{\partial c_i^{*(0)}}{\partial t^*} = D_i \frac{\partial^2 c_i^{*(0)}}{\partial y^{*2}}, \qquad \begin{cases} i = 1, & -\infty < y^* \le 0 \\ i = 2, & 0 \le y^* < \infty \end{cases} \tag{3.6}$$

where y^* is the y coordinate. The concentration profiles $c_i^{*(0)}\left(t^*, y^*\right)$ are deduced from Eq. (3.6) complemented by the following conditions:

A1. Interfacial conditions

a. Concentration continuity:

$$c_1^{*(0)}\left(t^*,0\right)=c_2^{*(0)}\left(t^*,0\right) \tag{3.7}$$

b. Equality of the solvent fluxes, that is, no accumulation of solvent:

$$D_1\frac{\partial c_1^{*(0)}}{\partial y^*}\left(t^*,0\right)=D_2\frac{\partial c_2^{*(0)}}{\partial y^*}\left(t^*,0\right) \tag{3.8}$$

A2. Initial conditions: uniform concentration profiles in each phase:

$$\begin{cases} c_1^{*(0)}\left(0,y^*\right)=c_{1\infty} \\ c_2^{*(0)}\left(0,y^*\right)=c_{2\infty} \end{cases} \tag{3.9}$$

where $c_{1\infty}$ and $c_{2\infty}$ are the initial solvent concentrations in phases 1 and 2, respectively.

The solutions can then be written as:

$$\begin{cases} c_1^{*(0)}\left(t^*,y^*\right)=\dfrac{c_{1\infty}\sqrt{d}+c_{2\infty}}{\sqrt{d}+1}-\dfrac{\left(c_{2\infty}-c_{1\infty}\right)}{\sqrt{d}+1}\operatorname{erf}\left(\dfrac{-y^*}{2\sqrt{D_1t^*}}\right), & -\infty < y^* \le 0 \\ c_2^{*(0)}\left(t^*,y^*\right)=\dfrac{c_{1\infty}\sqrt{d}+c_{2\infty}}{\sqrt{d}+1}+\dfrac{\left(c_{2\infty}-c_{1\infty}\right)\sqrt{d}}{\sqrt{d}+1}\operatorname{erf}\left(\dfrac{y^*}{2\sqrt{D_1t^*}}\right), & 0 \le y^* < \infty \end{cases} \tag{3.10}$$

where $d=\dfrac{D_1}{D_2}$, and $\operatorname{erf}\left(Y\right)=\dfrac{2}{\sqrt{\pi}}\displaystyle\int_0^Y e^{-z^2}dz$. The solvent concentration profiles are shown in Fig. 3.2 for $t_0 = 10^{-3}$ s, as the polymer concentration $c_p^{*(0)}$ is defined as follows:

$$c_p^{*(0)}(y^*)=\rho_2-c_2^{*(0)}(y^*) \tag{3.11}$$

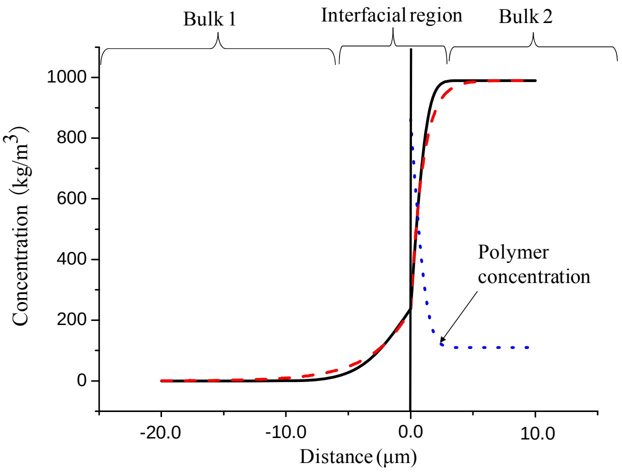

Fig. 3.2. Concentration profiles: $c_i^{*(0)}$ (solid line), $c_i^{*(00)}$ (dashed line), and $c_p^{*(0)}$ (dotted line) of the basic polymer solution in bulk 2 at time $t_0 = 10^{-3}$ s deduced from Eqs. (3.10), (3.13), and (3.11), respectively, with D_1, D_2, $c_{1\infty}$, and $c_{2\infty}$ as shown in Table 3.2.

The concentration profiles are approximated by using an approximation of the error function [Sørensen1977]:

$$1-\mathrm{erf}(Y)=1+\mathrm{erf}(-Y)\approx \exp(-1.444Y) \tag{3.12}$$

The corresponding concentration profiles after approximation, $c_i^{*(00)}$, define the basic solution for the solvent concentration in each phase. The basic solution $c_i^{*(0)}(t^*, y^*)$ given by Eq. (3.10) is first written at time $t^* = t_0$, then Eq. (3.12) is used to obtain the approximation of Eq. (3.10) as follows:

$$\begin{cases} c_1^{*(00)}(y^*) = c_{1\infty} + \Delta c_1^{(0)} \exp(\beta_1 y^*), & -\infty < y^* \le 0 \\ c_2^{*(00)}(y^*) = c_{2\infty} - \Delta c_2^{(0)} \exp(-\beta_2 y^*), & 0 \le y^* < \infty \end{cases} \tag{3.13}$$

where: $\Delta c_1^{(0)} = \dfrac{c_{2\infty} - c_{1\infty}}{\sqrt{d}+1}$, $\Delta c_2^{(0)} = \dfrac{\left(c_{2\infty} - c_{1\infty}\right)\sqrt{d}}{\sqrt{d}+1}$, $\beta_1 = \dfrac{1.444}{2\sqrt{d\,D_2\,t_0}}$,

$\beta_2 = \dfrac{1.444}{2\sqrt{D_2\,t_0}}$, and $\beta_2 = \sqrt{d}\ \beta_1$.

3.1.4 Perturbation equation and normal mode method

Different scales are first introduced to perform the stability analysis. The length scale H is the diffusion length $\sqrt{D_2\,t_0}$ associated to the diffusion process in phase 2 at time t_0. Time, velocities, pressures and solvent concentrations are scaled with $\dfrac{H^2}{D_2}$, $\dfrac{D_2}{H}$, $\rho_i\left(\dfrac{D_2}{H}\right)^2$ and $\Delta c_2^{(0)}$ respectively. The dimensionless governing equations of mass, linear momentum and solvent diffusion read now:

$$\nabla \cdot \vec{v}_i = 0 \tag{3.14}$$

$$\frac{\partial \vec{v}_i}{\partial t} + \vec{v}_i \,.\, \nabla \vec{v}_i = -\frac{\rho_2}{\rho_i}\nabla p_i + \frac{\mu_i}{\rho_i\,D_2}\nabla^2 \vec{v}_i \tag{3.15}$$

$$\frac{\partial c_i}{\partial t} + \vec{v}_i \cdot \nabla c_i = \frac{D_i}{D_2}\nabla^2 c_i \tag{3.16}$$

where in dimensionless form, $\vec{v}_i$ is the velocity, p_i the pressure, and c_i the solvent concentration in phase *i*. Some dimensionless parameters are introduced such as the density ratio $f = \dfrac{\rho_1}{\rho_2}$, the viscosity ratio $m = \dfrac{\mu_1}{\mu_2}$ and the Schmidt number, $\mathrm{Sc} = \dfrac{\mu_2}{\rho_2 D_2}$.

The velocities, pressures and concentrations are then expressed as the sums of the corresponding value for the basic solution and a perturbation:

$$\vec{v}_i = \vec{v}_i^{(0)} + \delta v_i \vec{y}, \quad p_i = p_i^{(0)} + \delta p_i, \quad c_i = c_i^{(00)} + \delta c_i \tag{3.17}$$

where $\vec{v}_i^{(0)} = 0$, and $p_i^{(0)}$ is uniform. The location of the deformed interface y_S is defined as:

$$y_S = \delta h(x,t) \tag{3.18}$$

where δh is the interfacial deformation. Eqs. (3.14)-(3.16) are then linearized and read:

$$\nabla \cdot \delta\vec{v}_i = 0 \tag{3.19}$$

$$\begin{cases} \dfrac{\partial \delta\vec{v}_1}{\partial t} = -\dfrac{1}{f}\nabla\delta p_1 + \dfrac{m\mathrm{Sc}}{f}\nabla^2\delta\vec{v}_1 \\ \dfrac{\partial \delta\vec{v}_2}{\partial t} = -\nabla\delta p_2 + \mathrm{Sc}\nabla^2\delta\vec{v}_2 \end{cases} \tag{3.20}$$

$$\begin{cases} \dfrac{\partial \delta c_1}{\partial t} + \delta\vec{v}_1 \cdot \nabla c_1^{(00)} = d\nabla^2\delta c_1 \\ \dfrac{\partial \delta c_2}{\partial t} + \delta\vec{v}_2 \cdot \nabla c_2^{(00)} = \nabla^2\delta c_2 \end{cases} \tag{3.21}$$

The perturbation is generated at the interface and vanishes far from the interface:

$$\begin{cases} \delta\vec{v}_1, \delta p_1, \delta c_1 \to 0 \quad \text{as } y \to -\infty \\ \delta\vec{v}_2, \delta p_2, \delta c_2 \to 0 \quad \text{as } y \to \infty \end{cases} \tag{3.22}$$

The interfacial conditions at the interface are:

B1. Condition for the bulks

a. Continuity of the normal component of the velocities:

$$\delta \vec{v}_1 . \vec{y}\big|_{y=0} = \delta \vec{v}_2 . \vec{y}\big|_{y=0} \tag{3.23}$$

b. Continuity of the tangential component of the velocities. This equation can be expressed thanks to Eq. (3.19) in terms of the normal components δv_i ($i = 1, 2$) only:

$$\frac{\partial}{\partial y}\left(\delta v_1\right)\Big|_{y=0} = \frac{\partial}{\partial y}\left(\delta v_2\right)\Big|_{y=0} \tag{3.24}$$

c. Continuity of the solvent concentrations

$$\delta c_1 + \left.\frac{\partial c_1^{(00)}}{\partial y}\right|_{y=0} \delta h = \delta c_2 + \left.\frac{\partial c_2^{(00)}}{\partial y}\right|_{y=0} \delta h \tag{3.25}$$

B2. Kinematic condition:

$$\delta v_1\big|_{y=0} = \frac{\partial \delta h}{\partial t} \tag{3.26}$$

The interfacial excess polymer concentration Γ^* and the interfacial tension σ^* are scaled respectively with $\Gamma_{\max}$ and σ_0^*, the interfacial tension at the interface in the basic state. The dimensionless interfacial excess polymer concentration Γ and interfacial tension σ are such that:

$$\Gamma = \frac{\Gamma_0^*}{\Gamma_{\max}} + \delta\Gamma , \quad \sigma = 1 + \delta\sigma \tag{3.27}$$

where Γ_0^* is the value of Γ^* for the basic state. Due to polymer adsorption, three more interfacial equations are needed as follows:

C1. Interfacial mass balance:

$$\frac{\Gamma_{\max}}{\Gamma_0^*}\frac{\partial(\delta\Gamma)}{\partial t} - \left.\frac{\partial(\delta v_2)}{\partial y}\right|_{y=0} - \frac{D_S}{D_2}\frac{\Gamma_{\max}}{\Gamma_0^*}\frac{\partial^2(\delta\Gamma)}{\partial x^2} = \frac{\Delta c_2^{(0)} H}{\Gamma_0^*}\left[\left.\frac{\partial(\delta c_2 - d\,\delta c_1)}{\partial y}\right|_{y=0} + \left.\frac{\partial^2\left(c_2^{(00)} - d\,c_1^{(00)}\right)}{\partial y^2}\right|_{y=0}\delta h\right] \tag{3.28}$$

where D_S is the surface diffusion coefficient;

C2. Interfacial normal linear momentum balance:

$$\left.\frac{\Gamma_0^*}{\rho_2 H}\frac{\partial(\delta v_1)}{\partial t}\right|_{y=0} = (\delta p_1 - \delta p_2)_{y=0} - 2\mathrm{Sc}\left[m\frac{\partial(\delta v_1)}{\partial y} - \frac{\partial(\delta v_2)}{\partial y}\right]_{y=0} + \frac{\mathrm{Sc}}{\mathrm{Cr}}\frac{\partial^2(\delta h)}{\partial x^2} \tag{3.29}$$

where Cr is the crispation number defined as $\frac{\mu_2 D_2}{\sigma_0^* H}$ and the last term of the right side includes the deformation of the interface (δh);

C3. Interfacial tangential linear momentum balance:

$$\left.\frac{\Gamma_0^* D_2}{\mu_2 H}\frac{\partial}{\partial t}\left(\frac{\partial(\delta v_1)}{\partial y}\right)\right|_{y=0} = -\left[\frac{\partial^2(\delta v_2)}{\partial x^2} - m\frac{\partial^2(\delta v_1)}{\partial x^2}\right]_{y=0} - \mathrm{Ma}\frac{\partial^2(\delta\sigma)}{\partial x^2} \tag{3.30}$$

where $\mathrm{Ma} = \dfrac{\left|\left.\dfrac{\partial\sigma^*}{\partial\Gamma^*}\right|_{y=0}\right|\Gamma_{\max}H}{\mu_2 D_2}$ is the Marangoni number. The perturbations $\delta\Gamma$ and $\delta\sigma$ can be expressed as follows based on Eqs (3.4) and (3.5):

$$\delta\Gamma = -K_2\left(\delta c_2\big|_{y=0} + \left.\frac{\partial c_2^{(00)}}{\partial y}\right|_{y=0}\delta h\right) \tag{3.31}$$

$$\delta\sigma = -\alpha_\Gamma\frac{\Gamma_{\max}}{\sigma_0^*}\delta\Gamma \tag{3.32}$$

where $K_2 = \dfrac{K^l\Delta c_2^{(0)}}{\left(1 + K^l\Delta c_2^{(0)}c_{p/s}^{(0)}\right)^2}$ and $\alpha_\Gamma = \dfrac{RT}{M_w}\left(1 + K^l\Delta c_2^{(0)}c_{p/s}^{(0)}\right)$.

The stability analysis is carried out in terms of normal modes. The different unknowns are defined as:

$$\begin{aligned} &\delta v_i = \tilde{v}_i(y)e^{ikx+\omega t}, \quad \delta p_i = \tilde{p}_i(y)e^{ikx+\omega t}, \quad \delta c_i = \tilde{c}_i(y)e^{ikx+\omega t}, \\ &\delta \Gamma = \tilde{\Gamma}e^{ikx+\omega t}, \qquad \delta\sigma = \tilde{\sigma}e^{ikx+\omega t}, \qquad \delta h = \tilde{h}\,e^{ikx+\omega t} \end{aligned} \tag{3.33}$$

where k is the wavenumber, ω the growth rate of the perturbation, and $\tilde{v}_i$, $\tilde{p}_i$, $\tilde{c}_i$, $\tilde{\Gamma}$, $\tilde{\sigma}$, and $\tilde{h}$ the amplitudes of each perturbation.

First, the different fields $\tilde{v}_i$, $\tilde{p}_i$, and $\tilde{c}_i$ are determined as follows and then are introduced into the interfacial balances to obtain the dispersion equation. Combining the continuity and Navier-Stokes equations in each phase, a differential equation for the pressures $\tilde{p}_i$ is deduced:

$$\Delta \tilde{p}_i = 0, \quad i = 1, 2 \tag{3.34}$$

The boundary conditions Eq. (3.22) lead to the solutions:

$$\begin{cases} \tilde{p}_1(y) = \tilde{p}_{10}\,e^{ky}, & -\infty < y \le 0 \\ \tilde{p}_2(y) = \tilde{p}_{20}\,e^{-ky}, & 0 \le y < \infty \end{cases} \tag{3.35}$$

where $\tilde{p}_{10}$ and $\tilde{p}_{20}$ are two constants to be determined. Substituting the two expressions for $\tilde{p}_1$ and $\tilde{p}_2$ given by Eq (3.35) into the Navier-Stokes equations Eq (3.20), the velocities in phases 1 and 2 take the form:

$$\begin{cases} \tilde{v}_1(y) = A_1\,e^{ky} + B_1\,e^{q_1 y}, & -\infty < y \le 0 \\ \tilde{v}_2(y) = A_2\,e^{-ky} + B_2\,e^{-q_2 y}, & 0 \le y < \infty \end{cases} \tag{3.36}$$

where: $q_1 = \sqrt{k^2 + \frac{f\,\omega}{m\,\mathrm{Sc}}}$, $q_2 = \sqrt{k^2 + \frac{\omega}{\mathrm{Sc}}}$, $\tilde{p}_{10} = -\frac{f\,\omega}{k} A_1$, $\tilde{p}_{20} = \frac{\omega}{k} A_2$, and A_1, A_2, B_1, and B_2 are four constants to be determined. The two diffusion equations Eq. (3.21) can now be solved with:

$$c_1^{(00)} = \frac{c_{1\infty}}{\Delta c_2^{(0)}} + \frac{1}{\sqrt{d}} \exp\left(\frac{\beta_2 H}{\sqrt{d}} y \right), \quad c_2^{(00)} = \frac{c_{2\infty}}{\Delta c_2^{(0)}} - \exp\left(- \beta_2 H\, y \right) \tag{3.37}$$

Due to the choice of diffusion time t_0 associated to H, the length H can be such that $\beta_2 H = 1$. The perturbations $\tilde{c}_1$ and $\tilde{c}_2$ are consequently given by:

$$\begin{cases} \tilde{c}_1(y) = l_1 e^{r_1 y} + \dfrac{A_1}{d^2\left[(b+k)^2 - r_1^2\right]} e^{(k+b)y} + \dfrac{B_1}{d^2\left[(b+q_1)^2 - r_1^2\right]} e^{(q_1+b)y}, & -\infty < y \le 0 \\ \tilde{c}_2(y) = l_2 e^{-r_2 y} + \dfrac{A_2}{\left[(1+k)^2 - r_2^2\right]} e^{-(k+1)y} + \dfrac{B_2}{\left[(1+q_2)^2 - r_2^2\right]} e^{-(q_2+1)y}, & 0 \le y < \infty \end{cases} \tag{3.38}$$

where $r_1 = \sqrt{k^2 + \frac{\omega}{d}}$, $r_2 = \sqrt{k^2 + \omega}$, $b = \frac{\beta_1}{\beta_2} = \frac{1}{\sqrt{d}}$, and l_1 and l_2 are two new constants to be determined. The perturbation solution depends on 9 constants, A_1, A_2, B_1, B_2, l_1, l_2, $\tilde{h}$, $\tilde{\Gamma}$ and $\tilde{\sigma}$. The perturbation is the solution of the linear system of equations deduced from Eqs. (3.23)-(3.26), and (3.28)-(3.32). The dispersion equation is obtained by writing that the determinant $\det(M)$ of the linear system defined by its matrix M has to be zero.

$$\det(M) = F(\omega, k) = 0 \tag{3.39}$$

The function F contains several parameters such as the diffusivity, viscosity, and density ratios, the Schmidt number $\mathrm{Sc} = \frac{\mu_2}{\rho_2 D_2}$, the adsorption number $\mathrm{Na} = \frac{\mathit{\Gamma}_{\max}}{\mathit{\Delta} c_2^{(0)} H}$, the interfacial diffusion number $\mathrm{I_D} = \frac{D_S \mathit{\Gamma}_{\max}}{\mu_2 H}$, the crispation number $\mathrm{Cr} = \frac{\mu_2 D_2}{\sigma_0^* H}$, the Marangoni number $\mathrm{Ma} = \frac{\alpha_\mathit{\Gamma} \mathit{\Gamma}_{\max} H}{\mu_2 D_2}$ and the mass fraction of solvent in phase 2. All these dimensionless numbers can be expressed as the ratios of characteristic times as shown in Table 3.1.

Table 3.1. Different characteristic times and dimensionless groups.

Characteristic times			Dimensionless groups	
Momentum diffusion	$t_v = \frac{H^2 \rho_2}{\mu_2}$		Schmidt	$\mathrm{Sc} = \frac{t_D}{t_v}$
Species diffusion	$t_D = \frac{H^2}{D_2}$		Interfacial diffusion	$\mathrm{I_D} = \frac{t_v}{t_{\mathrm{int},D}}$
Adsorption	$t_{ads} = \frac{\mathit{\Gamma}_{\max} H}{\Delta c_2^{(0)} D_2}$		Adsorption	$\mathrm{Na} = \frac{t_{ads}}{t_D}$
Interfacial diffusion	$t_{\mathrm{int},D} = \frac{\rho_2 H^3}{\mathit{\Gamma}_{\max} D_S}$		Crispation	$\mathrm{Cr} = \frac{(t_c)^2}{t_v t_D}$
Capillary	$t_c = \sqrt{\frac{\rho_2 H^3}{\sigma_0^*}}$		Marangoni	$\mathrm{Ma} = \frac{t_v t_D}{(t_{\mathrm{Ma}})^2}$
Marangoni	$t_{\mathrm{Ma}} = \sqrt{\frac{\rho_2 H^3}{\alpha_\mathit{\Gamma} \mathit{\Gamma}_{\max}}}$			

In order to study the onset of instability in the neighborhood of marginal stability corresponding to $\omega = 0$, when the perturbation does not grow or decay with time, the different elements of the matrix M are expanded in powers of ω. Keeping only the first order terms in ω in the determinant, the characteristic equation is now written as:

$$\mathcal{A} - \mathcal{B}\omega = 0 \tag{3.40}$$

where $\mathcal{A}$ and $\mathcal{B}$ are expressed in terms of the dimensionless groups as:

$$\mathcal{A} = \mathrm{Ma}\, k^2 \left\{ \frac{\Gamma_0^*}{\Gamma_{\max}} + \frac{1}{\mathrm{Na}} \left[\frac{1}{d(2k+b)^2} - \frac{1}{(2k+1)^2} \right] \right\} \tag{3.41}$$

$$\begin{aligned} \mathcal{B} = & -\left[k^2 \mathrm{I_D} - k \frac{\Delta c_2^{(0)}}{\rho_2} \frac{(d+1)}{\mathrm{Sc}\, K_2} \right] + \mathrm{Ma} \frac{\mathrm{Cr}(f-1)}{2k^2\, \mathrm{Na}\, \mathrm{Sc}} (b+1-2k) \\ & - \mathrm{Ma} \left\langle \frac{k}{\mathrm{Na}} \left[\frac{1+\dfrac{1}{2\mathrm{Sc}}}{(2\mathrm{k}+1)^3} - \frac{1+\dfrac{fd}{2m\mathrm{Sc}}}{d^2(2\mathrm{k}+b)^3} \right] \right. \\ & \left. + 2(m+1)\mathrm{Cr}\, k \left\{ \frac{\Gamma_0^*}{\Gamma_{\max}} + \frac{1}{\mathrm{Na}} \left[\frac{1}{d(2k+b)^2} - \frac{1}{(2k+1)^2} \right] \right\} \right\rangle \end{aligned} \tag{3.42}$$

3.2 Validation of Onset of hydrodynamic instability

Since the solutal Marangoni instability happens only during the initial mass transport stages, some polymer/solvent/nonsolvent materials may not have enough time to develop. For PAN/DMSO/water system, the interfacial tension is not sensitive to PAN concentration [Weh2004], so the interfacial gradient of PAN solution/water interface ($\delta\sigma$)

is weak when the PAN adsorption variation ($\delta\Gamma$) is small at the beginning of phase inversion, and in Eq. (3.32) α_Γ is very small. Based on the definition of the Marangoni number $\mathrm{Ma} = \frac{\alpha_\Gamma \Gamma_{\max} H}{\mu_2 D_2}$, a smaller α_Γ will reduce the value of Ma. While from the dispersion relation Eqs. (3.40) to (3.42), it can be deduced that the growth rate ω will be smaller, which means the Marangoni instability needs a longer time to develop. Since a rapid solidification is observed in the PAN/DMSO/water HFM fabrication, the polymer solution solidifies before the Marangoni instability can totally develop. Therefore, another model of groove formation during solidification needs to be developed for PAN/DMSO/water HFMs, which will be discussed in Chapter 4.

Since the model presented in this chapter is dimensionless, the model can be applied to different polymer/solvent/nonsolvent systems with different material properties. Since the hydrodynamic instability can develop in PU/DMSO/water HFMs fabrication, the groove formation results for the fabrication of PU/DMSO/water HFMs [Long2008] is used to validate this theory.

3.2.1 Dispersion relation for PU/DMSO/water

In Long *et al.*'s work [Long2008], HFMs were fabricated for a PU (M_w = 40000-70000 Da; Thermedics Polymer, Wilmington, MA, USA)/DMSO (Sigma-Aldrich, Milwaukee, WI, USA) solution as shown in Fig. 1.9. The polymer solution was co-extruded with a nonsolvent (de-ionized water) through a spinneret. Both polymer solution and nonsolvent flows passed through a 10 mm air gap before the nascent HFM enter the bath. The fabrication process was implemented under different conditions by varying the flow rates and the polymer concentration.

For the (PU/DMSO)/water solution, the absolute temperature is T = 298 K, the gas constant R = 8.31 J/(K·mol) and the PU molecular weight M_w is assumed equal to 50 kg/mol. The polymer maximum adsorbed amount $\mathit{\Gamma}_{\max}$ is about 4×10^{-6} mol/m^2 ~ 0.2 g/m^2 [Rios1994], and the Langmuir equilibrium constant is taken as $K^l = 0.02$ m^3/kg [Fleer1993]. The different parameters used to define the system are given in Table 3.2 of the Appendix. The interfacial tension σ_0^* and the ratio $\frac{\mathit{\Gamma}_0^*}{\mathit{\Gamma}_{\max}}$, obtained using Eqs (3.5) and (3.4), are about 2×10^{-2} N/m, and close to 1, respectively. The surface diffusivity D_s [Valkovska2000], is assumed of the same order as the bulk diffusion coefficients 10^{-10} m^2/s and can then be defined as $D_s = \frac{D_1 + D_2}{2}$ [Sørensen1977].

Table 3.2. Parameters in PU/DMSO/water HFM fabrication.

Parameters		
ρ_1	Density of phase 1	1000 kg/m^3
ρ_2	Density of phase 2	1100 kg/m^3
μ_1	Viscosity of phase 1	10^{-3} kg/(m·s)
μ_2	Viscosity of phase 2	5 kg/(m·s)
D_1	Solvent diffusivity in phase 1	5×10^{-9} m^2/s
D_2	Solvent diffusivity in phase 2	5×10^{-10} m^2/s
t_0	Diffusion time	10^{-3} s
β_1	Solvent profile coefficient in phase 1	$10^6/\sqrt{10}$ m^{-1}
β_2	Solvent profile coefficient in phase 2	10^6 m^{-1}
M_w	PU molecular weight	50 kg/mol
$\Gamma_{\max}$	Excess polymer concentration	2×10^{-4} kg/m^2
K^l	Langmuir equilibrium constant	0.02 m^3/kg
$c_{1\infty}$	Initial solvent concentration in phase 1	0
$c_{2\infty}$	Initial solvent concentration in phase 2	990 kg/m^3
$\sigma_{solv}{}^*$	Interfacial tension DMSO/water	0.046 N/m
α_Γ	Interfacial tension gradient	9.03×10^2 m^2/s^2
K_2	Equilibrium constant in phase 2	4.52×10^{-2}
σ_0^*	Interfacial tension for basic state	0.017 N/m

With the data in Table 3.2, the first two terms in $\mathcal{B}$ can be neglected (Eq. 3.42) except in the vicinity of zero, and the growth rate is approximated by:

$$\omega = \frac{k\left\{\frac{\mathit{\Gamma}_0^*}{\mathit{\Gamma}_{\max}} + \frac{1}{\mathrm{Na}}\left[\frac{1}{d\left(2k+b\right)^2} - \frac{1}{\left(2k+1\right)^2}\right]\right\}}{-2\left(m+1\right)\mathrm{Cr}\frac{\mathit{\Gamma}_0^*}{\mathit{\Gamma}_{\max}} + \frac{1}{\mathrm{Na}}\left[-\frac{1}{\left(2\mathrm{k}+1\right)^3} + \frac{1+\frac{fd}{2m\mathrm{Sc}}}{d^2\left(2\mathrm{k}+b\right)^3} - 2\left(m+1\right)\mathrm{Cr}\left[\frac{1}{d\left(2k+b\right)^2} - \frac{1}{\left(2k+1\right)^2}\right]\right]}$$

(3.43)

The growth rate depends on some dimensionless numbers characterizing capillary and soluto-capillary effects such as Cr and Ma. The growth rate dependence in terms of Ma is very weak except close to the origin. A nonzero growth rate ω depends on the existence of an interfacial tension gradient but not on the value of this gradient. If the interfacial tension remains constant and does not depend on the polymer concentration, Ma is zero, resulting in a zero ω too. The numerator in Eq. (3.43) defines the range of instability, and this range depends on Na and $\frac{\mathit{\Gamma}_0^*}{\mathit{\Gamma}_{\max}}$, which is close to one. It should be noted that while the Marangoni instability is considered the dominant factor leading to the onset of instability herein, the contributions of other effects such as capillary effects have also been included in determining the onset of instability as seen in Eq. (3.43).

The dispersion curve of Fig. 3.3 shows that there exist three regions delimited by

$k_{cr,\min}$ and $k_{cr,\max}$, two critical wavenumbers. For k between $k_{cr,\min}$ and $k_{cr,\max}$, the perturbation grows and grooves may form. Consequently, the system is unstable for modes whose wavelengths λ^* are such that:

$$\lambda^*_{cr,\min} = \frac{2\pi}{k_{cr,\max}} H \; < \; \lambda^* \; < \lambda^*_{cr,\max} = \frac{2\pi}{k_{cr,\min}} H \tag{3.44}$$

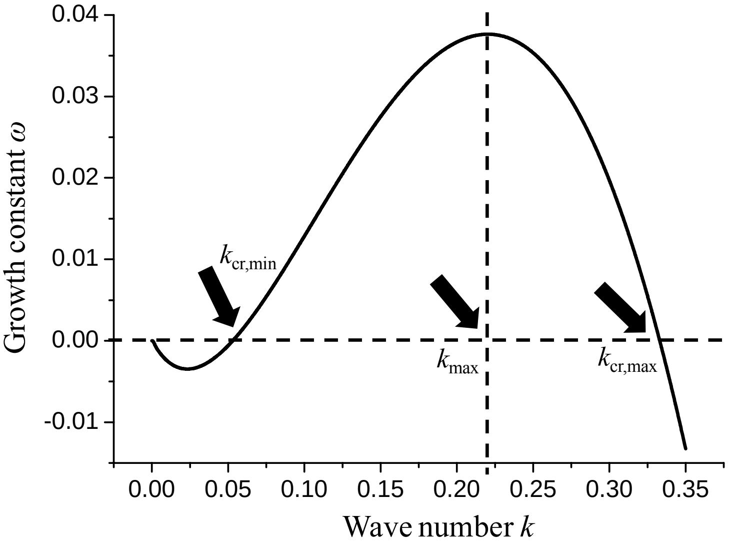

Fig. 3.3. Dispersion curve based on the parameters listed in Table 3.2.

For wavelengths smaller than $\lambda^*_{cr,\min}$ (minimum critical wavelength) or larger than $\lambda^*_{cr,\max}$ (maximum critical wavelength), the system is stable. Considering the groove number N instead of the wavelength of the perturbation, the results shown in Fig. 3.3 define a range for the groove number between $\frac{\pi D_I}{\lambda^*_{cr,\max}}$ and $\frac{\pi D_I}{\lambda^*_{cr,\min}}$, where D_I is the

HFM inner diameter. Sørensen *et al.* [Sørensen1978] also found two strictly positive values, $k_{cr,\min}$ and $k_{cr,\max}$, delimiting the instability region in case of an exponential concentration profile. The only restriction for $k_{cr,\min}$ or $\lambda^*_{cr,\max}$ is that the wavelength has to be smaller than the inner perimeter πD_I.

The most unstable mode is obtained for $k_{\max}$, the wavenumber of the most dangerous wave. The wavelength $\lambda^*_{cr,\max} = \frac{2\pi H}{k_{\max}}$ associated with $k_{\max}$ gives the number of grooves:

$$N = \frac{D_I}{2H} k_{\max} \tag{3.45}$$

For the parameters in Table 3.2, an estimation of $\lambda^*_{\max}$ is 25 μm, which is of the order of the groove width measured in Long *et al.*'s experiment [Long2008]. Therefore, the model can predict the order of magnitude of the groove width and of the groove number. For given fluids, the dispersion curve depends on $\frac{\Gamma^*_0}{\Gamma_{\max}}$, Na, and Cr; or alternatively, $\Gamma_{\max}$, K^I, and $c_{2\infty}$ based on the definitions of Na and Cr and Eqs. (3.31), (3.42), (3.46), (3.47), and (3.48). The influence of these different parameters on the system instability is shown in Figs 3.4, 3.5, and 3.6.

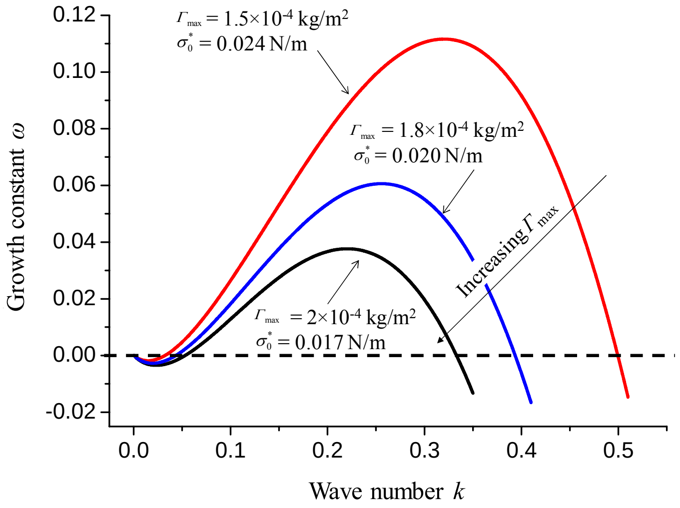

Fig. 3.4. Effect of $\Gamma_{\max}$ on the dispersion curve based on other parameters listed in Table 3.2 (σ_0^* depends on $\Gamma_{\max}$).

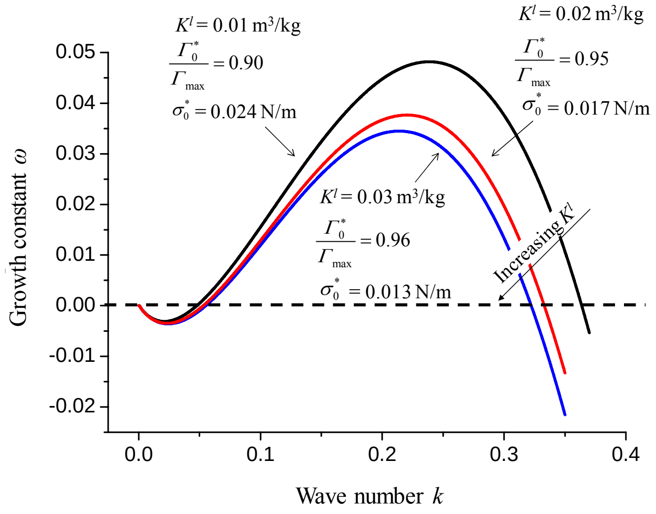

Fig. 3.5. Effect of K^l on the dispersion curve based on other parameters listed in Table 3.2 ($\frac{\Gamma_0^*}{\Gamma_{\max}}$ and σ_0^* depend on K^l).

3.2.2 Model validation

The maximum interfacial polymer concentration $\Gamma_{\max}$ is the maximum polymer amount adsorbed on the interface associated to the affinity of the interface to a certain polymer. Increasing the Langmuir equilibrium constant K^l measuring the ability to adsorb increases the changes in polymer concentration and consequently decreases the time necessary to introduce a surface tension gradient and finally will increase the growth rate ω. For fixed K^l and given polymer concentration scenarios, increasing $\Gamma_{\max}$ keeps the $\frac{\Gamma^*{}_0}{\Gamma_{\max}}$ ratio constant, decreases the interfacial tension, increases the adsorption time, and consequently decreases the growth rate. When $\Gamma_{\max}$ increases, $k_{\max}$ decreases and the number of grooves N decreases. Increasing $\Gamma_{\max}$ from 1.5×10^{-4} to 2×10^{-4} produces a decrease of 25% in the groove number (Fig. 3.4). Increasing K^l also leads to a decrease in the groove number, but this dependence is less sensitive to the Langmuir constant (K^l) than to the maximum excess polymer concentration ($\Gamma_{\max}$).

The problem examined was a 2D problem in a horizontal cross section and the flows of polymer solution and nonsolvent were ignored. The flow rates actually affect K^l. Increasing the polymer solution flow rate increases $\frac{\Gamma_0^*}{\Gamma_{\max}}$ for a given initial polymer concentration and thus increases K^l. The increase of K^l produces a decrease in both $k_{\max}$ and the number of grooves N as seen from Fig. 3.5, and this tendency is the same as in the experimental results [Long2008]. Increasing the inner nonsolvent flow rate decreases $\frac{\varGamma_0^*}{\varGamma_{\max}}$ for a given initial polymer concentration and thus decreases K^l. The decrease of K^l produces an increase in $k_{\max}$ (Fig. 3.5) and the number of grooves N, which is also in agreement with the experimental results [Long2008].

The different dimensionless groups (Na, $\frac{\varGamma_0^*}{\varGamma_{\max}}$, and Cr), appearing in Eq. (3.43), depend on the initial concentration of polymer ($c_{p\infty}$) or solvent ($c_{2\infty}$) in phase 3. It should be noted that in generating Fig. 3.6, Na, $\frac{\varGamma_0^*}{\varGamma_{\max}}$, and Cr are given, respectively, as follows:

$$\mathrm{Na} = \frac{\varGamma_{\max}}{\Delta c_2^{(0)} H} \quad \text{with} \quad \Delta c_2^{(0)} = \frac{c_{2\infty}\sqrt{d}}{\sqrt{d}+1} \tag{3.46}$$

$$\frac{\varGamma_0^*}{\varGamma_{\max}} = \frac{K^l c_{p/s}^{*(00)}}{1 + K^l c_{p/s}^{*(00)}} \quad \text{with} \quad c_{p/s}^{*(00)} = \rho_2 - c_{2/s}^{*(00)} = \rho_2 - \frac{c_{2\infty}}{\sqrt{d}+1} \tag{3.47}$$

where $c_{2/s}^{*(00)}$ is the solvent concentration in phase 2 evaluated just above the interface.

$$\mathrm{Cr} = \frac{\mu_2 D_2}{H \sigma_0^*} \quad \text{with} \quad \sigma_0^* = \sigma_{solv}^* - \frac{RT}{M_w}\varGamma_{\max} \ln\left(1 + K^l c_{p/s}^{*(00)}\right) \tag{3.48}$$

Several dispersion curves are given in Fig. 3.6 to show the effect of the initial polymer concentration. They are obtained from the following expressions of $Num(\omega)$ and $Den(\omega)$ as $\omega = \frac{Num(\omega)}{Den(\omega)}$, where

$$Num(\omega) = k\left\{\frac{K^l\left(\rho_2 - \frac{c_{2\infty}}{\sqrt{d}+1}\right)}{1+K^l\left(\rho_2 - \frac{c_{2\infty}}{\sqrt{d}+1}\right)} + \frac{c_{2\infty} H\sqrt{d}}{\Gamma_{\max}\left(\sqrt{d}+1\right)}\left[\frac{1}{d\left(2k+b\right)^2} - \frac{1}{\left(2k+1\right)^2}\right]\right\}$$

(3.49)

$$\begin{aligned} Den(\omega) = -2(m+1)\frac{\mu_2 D_2}{H\sigma_0^*}&\left\{\frac{K^l\left(\rho_2 - \frac{c_{2\infty}}{\sqrt{d}+1}\right)}{1+K^l\left(\rho_2 - \frac{c_{2\infty}}{\sqrt{d}+1}\right)} + \frac{c_{2\infty} H\sqrt{d}}{\Gamma_{\max}\left(\sqrt{d}+1\right)}\left[\frac{1}{d\left(2k+b\right)^2} - \frac{1}{\left(2k+1\right)^2}\right]\right\} \\ &+\frac{c_{2\infty} H\sqrt{d}}{\Gamma_{\max}\left(\sqrt{d}+1\right)}\left[-\frac{1}{\left(2\mathrm{k}+1\right)^3} + \frac{1+\frac{f\,d}{2m\mathrm{Sc}}}{d^2\left(2\mathrm{k}+b\right)^3}\right] \end{aligned}$$

(3.50)

and $\sigma_0^* = \sigma_{solv}^* - \frac{RT}{M_w}\Gamma_{\max}\ln\left[1+K^l\left(\rho_2 - \frac{c_{2\infty}}{\sqrt{d}+1}\right)\right]$. It can be seen that when the initial polymer concentration increases or the initial solvent concentration decreases, $k_{\max}$ decreases, the wavelength of the most dangerous wave increases and the number of grooves decreases. This prediction agrees well with the experimental results [Long2008] as shown in Fig. 3.6B. As discussed by Bonyadi *et al.* [Bonyadi2007] the stabilizing effect of the polymer concentration can be explained as follows. When the initial polymer concentration increases, the polymer chain orientation on the interface is higher. As a result, less solvent is extracted and the driving mechanism of the instability is reduced leading to a decrease of the groove number.

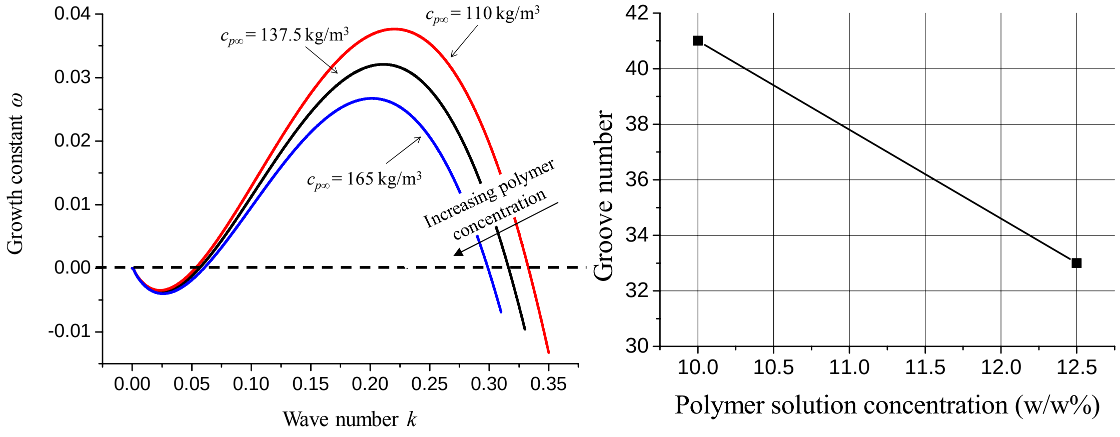

(A) (B)

Fig. 3.6. (A) Effect of initial polymer concentration ($c_{p\infty} = \rho_2 - c_{2\infty}$) on the dispersion curve based on other parameters listed in Table 3.2, and (B) experimental measurements of groove numbers [Long2008].

The comparison of the experimental and theoretical results shows that the evolution of the groove number in terms of the polymer concentration is in good agreement with the available experimental results. As so, the proposed model may give a plausible explanation of the HFM groove formation mechanism due to hydrodynamic instability.

3.3 Summary

The hydrodynamic instability for groove formation during HFM fabrication is studied in this chapter. The Marangoni effect is used to study the onset of hydrodynamic instability before the solidification of polymer solution. It was found that for PAN/DMSO/water HFMs the solutal Marangoni instability does not have enough time to develop before solidification, so the hydrodynamic instability is not valid to explain the groove formation of PAN/DMSO/water HFMs. But by studying the grooved PU/DMSO/water HFM fabrication, the predicted values of the groove number compares well with those experimental results. Therefore, the model developed here gives a reasonable explanation of the groove formation mechanism in PU/DMSO/water HFM fabrication.

CHAPTER FOUR

MULTILAYER BUCKLING MODEL FOR GROOVE FORMATION

Chapter 2 reports the fabrication of PAN/DMSO/water HFMs. In the case of PAN/DMSO/water system, the interfacial tension between water (nonsolvent) and the polymer solution just slightly depends on the PAN concentration [Weh2004]. Thus, due to the rapid solidification, the solutal Marangoni instability does not have time to develop, leading to a circular inner surface during the air gap. Therefore, the inner surface of PAN/DMSO/water HFMs remains circular until it enters the coagulation bath, and grooves form due to buckling when HFMs solidify. The shrinkage during HFM solidification introduces a radially inward stress in HFMs. When this inward stress is large enough, the inner skin layer buckles and forms a grooved texture. In this chapter, a multilayer model for HFM buckling is developed. The predicted results are compared with experimental results reported in Chapter 2 for PAN/DMSO/water HFMs.

4.1 Multilayer model of PAN HFMs

A representative six-layer morphology of both smooth and grooved HFMs is shown in Fig. 2.2B. Generally, the six-layer morphology consists of: (1) an inner and an outer top skin layers (I_1 and O_1 layers), which are formed by a vitrification process because of the sudden solvent outflow from the polymer solution; (2) two sublayers include I_2 and O_2 sublayers; and (3) two inner sublayers in the bulk (I_3 and O_3 sublayers). The sublayers are formed by liquid–liquid demixing [Machado1999, Bonyadi2007]. Both inner and outer skin layers (I_1 and O_1), where only tiny microvoids are formed, are thin but dense. The sublayers adjacent to the inner and outer skin (I_2 and O_2) are relatively thicker than the skin layers, and their structure is more porous. Also, these two sublayers are the transition region between the skin layer and the inner sublayer. The inner sublayers (I_3 and O_3), which are the thickest layers, are in the middle of HFM wall, and they contain macrovoids. Based on the aforementioned six-layer structure model [Bonyadi2007], it is assumed that the inner skin layer (I_1) buckles when the inward pressure exceeds the critical buckling pressure of the inner forming elastic skin layer. This radially inward pressure is mainly due to the shrinkage of the solidifying outer surface upon entering the coagulation bath.

For example, the six-layered structure is considered, so the HFM is modeled as a thin-walled elastic cylindrical shell with six distinct but seamlessly connected layers/sublayers as in Fig. 4.1. The Young's modulus of each layer/sublayer is E_i, the thickness of each layer/sublayer is h_i, where i stands for I_1, I_2, I_3, O_1, O_2 and O_3 as the index of each layer/sublayer. To model this inward pressure-induced buckling phenomenon, the following assumptions are introduced:

a). The material of each layer/sublayer is elastic and isotropic, then the strain-stress relations can be written as follows:

$$\begin{bmatrix} \varepsilon_{rr}^{(i)} \\ \varepsilon_{\theta\theta}^{(i)} \\ \varepsilon_{zz}^{(i)} \\ \gamma_{\theta z}^{(i)} \\ \gamma_{rz}^{(i)} \\ \gamma_{r\theta}^{(i)} \end{bmatrix} = \begin{bmatrix} \frac{1}{E_i} & -\frac{\nu}{E_i} & -\frac{\nu}{E_i} & 0 & 0 & 0 \\ -\frac{\nu}{E_i} & \frac{1}{E_i} & -\frac{\nu}{E_i} & 0 & 0 & 0 \\ -\frac{\nu}{E_i} & -\frac{\nu}{E_i} & \frac{1}{E_i} & 0 & 0 & 0 \\ 0 & 0 & 0 & \frac{2(1+\nu)}{E_i} & 0 & 0 \\ 0 & 0 & 0 & 0 & \frac{2(1+\nu)}{E_i} & 0 \\ 0 & 0 & 0 & 0 & 0 & \frac{2(1+\nu)}{E_i} \end{bmatrix} \begin{bmatrix} \sigma_{rr}^{(i)} \\ \sigma_{\theta\theta}^{(i)} \\ \sigma_{zz}^{(i)} \\ \tau_{\theta z}^{(i)} \\ \tau_{rz}^{(i)} \\ \tau_{r\theta}^{(i)} \end{bmatrix} \tag{4.1}$$

where $\sigma_{rr}^{(i)}$, $\sigma_{\theta\theta}^{(i)}$, $\sigma_{zz}^{(i)}$, $\tau_{\theta z}^{(i)}$, $\tau_{rz}^{(i)}$, and $\tau_{r\theta}^{(i)}$ are the components of the stress tensor, $\varepsilon_{rr}^{(i)}$, $\varepsilon_{\theta\theta}^{(i)}$, $\varepsilon_{zz}^{(i)}$, $\gamma_{\theta z}^{(i)}$, $\gamma_{rz}^{(i)}$, and $\gamma_{r\theta}^{(i)}$ are the components of the strain tensor expressed in the cylindrical coordinate system in Fig. 4.1. Due to the porous morphology of each layer, Young's moduli of the inner and outer skin layers (I_1 and O_1) are the highest, while the I_2 and O_2 sublayers are stiffer than the I_3 and O_3 sublayers due to the existence of macrovoids inside I_3 and O_3. In this work, it is assumed that all layers/sublayers have the same Poisson's ratio (ν) when their porosities are no more than 70% [Arnold1996].

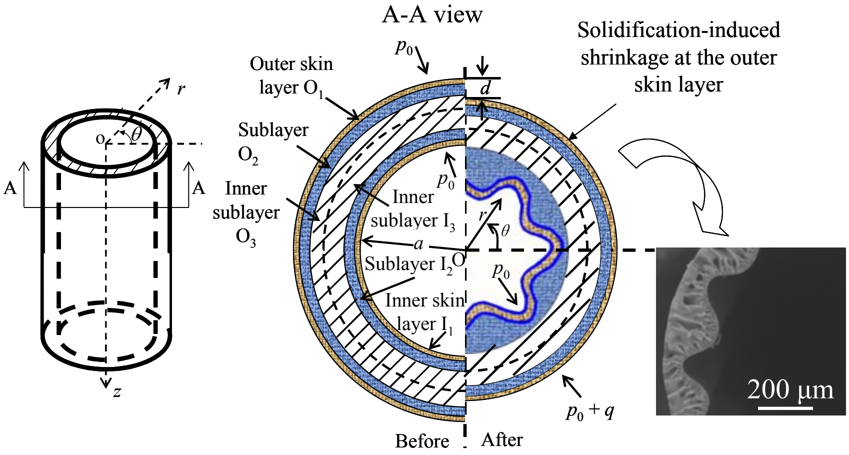

Fig. 4.1. Schematic of the six-layer model before and after the shrinkage-induced inward pressure.

b). The HFM fabrication process introduces an axially uniform, inward radial pressure on the inner skin layer (I_1) of the forming long hollow fiber, so as in a plane deformation case, the pre-buckling stress and displacement fields are axisymmetric, and the buckling modes are 2D for such a multilayer structure [Kardomateas2005]. Both stresses and the displacements do not depend on the axial coordinate z. Due to axisymmetry, the stresses and displacements are only dependent on the radial coordinate r;

c). Due to the macrovoid structure of sublayers I_2, O_2, I_3 and O_3, the shrinkage-induced inward pressure is transmitted to the inner skin layer (I_1) through the sublayers (O_1, I_2, O_2, I_3 and O_3). The buckling of I_1 is much smaller compared to the HFM diameter, so the inner skin layer buckling may not significantly affect the HFM stress distribution and displacement of the other layer/sublayers before and after buckling;

d). There is a pressure p_0 applied on both inner and outer surfaces before HFM shrinkage happens. The outer surface experiences an extra inward pressure q during the HFM shrinkage. Then the HFM is under an internal and an external pressures, p_0 and p_0+q, respectively (Fig. 4.1); and

e). Based on the fabrication process as shown in Fig. 1.9, when the polymer dope solution comes out of the spinneret, it first interacts with the inner nonsolvent fluid, resulting in an elastic inner skin layer. At that time, the outer skin layer is not well formed yet. In this study, it is assumed that this inner skin layer solidification-induced shrinkage may be fully released before the outer skin layer solidifies.

An elasticity theory-based solution for an orthotropic homogeneous cylindrical sandwich shell under an external or internal pressure has been discussed by Kardomateas *et al.* [Kardomateas2005]. The stresses of each layer/sublayer, as in an isotropic homogeneous deformation case, can be simplified as follows [Kardomateas2005, Timoshenko1970]

$$\sigma_{rr}^{(i)}(r) = A_i + B_i r^{-2} \tag{4.2}$$

$$\sigma_{\theta\theta}^{(i)}(r) = A_i - B_i r^{-2} \tag{4.3}$$

$$\sigma_{zz}^{(i)}(r) = 2\nu A_i \tag{4.4}$$

$$\tau_{\theta z}^{(i)} = \tau_{rz}^{(i)} = \tau_{r\theta}^{(i)} = 0 \tag{4.5}$$

and the radial displacement is found to be [Kardomateas2005]:

$$u^{(i)}(r) = A_i \frac{1-\nu-2\nu^2}{E_i} r - B_i \frac{1+\nu}{E_i} r^{-1} \tag{4.6}$$

where A_i and B_i are the coefficients to be determined based on the boundary and interfacial conditions, and i stands for I_1, I_2, I_3, O_1, O_2 and O_3 as the index of each layer/sublayer.

For a given outer surface shrinkage d, the O_1 displacement boundary condition is as follows:

$$u^{(O1)}\Big|_{r=a+h} = -d = A_{O1} \frac{1-\nu-2\nu^2}{E_{O1}}(a+h) - B_{O1} \frac{1+\nu}{E_{O1}}(a+h)^{-1} \tag{4.7}$$

where h is the HFM wall thickness, and a is the inner radius before shrinkage. The pressure on the inner surface is assumed to be the atmospheric pressure (~ 10^5 Pa), then the stress boundary condition along the inner surface is:

$$\sigma_{rr}^{(I1)}\Big|_{r=a} = A_{I1} + B_{I1} a^{-2} = -p_0 \tag{4.8}$$

where p_0 is assumed to be 10^5 Pa, which will not vary too much during the experiments.

For seamlessly connected HFM layers/sublayers, the radial stress $\sigma_{rr}^{(i)}$ is continuous at each interface. The five interfacial conditions are expressed as:

$$A_{I1} + B_{I1}(a + h_{I1})^{-2} = A_{I2} + B_{I2}(a + h_{I1})^{-2} \tag{4.9}$$

$$A_{I2} + B_{I2}(a + h_{I1} + h_{I2})^{-2} = A_{I3} + B_{I3}(a + h_{I1} + h_{I2})^{-2} \tag{4.10}$$

$$A_{I3} + B_{I3}(a + h_{I1} + h_{I2} + h_{I3})^{-2} = A_{O3} + B_{O3}(a + h_{I1} + h_{I2} + h_{I3})^{-2} \tag{4.11}$$

$$A_{O3} + B_{O3}(a + h_{I1} + h_{I2} + h_{I3} + h_{O3})^{-2} = A_{O2} + B_{O2}(a + h_{I1} + h_{I2} + h_{I3} + h_{O3})^{-2} \tag{4.12}$$

$$A_{O2} + B_{O2}(a + h_{I1} + h_{I2} + h_{I3} + h_{O3} + h_{O2})^{-2} = A_{O1} + B_{O1}(a + h_{I1} + h_{I2} + h_{I3} + h_{O3} + h_{O2})^{-2} \tag{4.13}$$

The radial displacement is also continuous, leading to the following five equations

$$A_{I1}\frac{1-\nu-2\nu^2}{E_{I1}}(a + h_{I1}) - B_{I1}\frac{1+\nu}{E_{I1}}(a + h_{I1})^{-1} = A_{I2}\frac{1-\nu-2\nu^2}{E_{I2}}(a + h_{I1}) - B_{I2}\frac{1+\nu}{E_{I2}}(a + h_{I1})^{-1} \tag{4.14}$$

$$\begin{aligned} &A_{I2}\frac{1-\nu-2\nu^2}{E_{I2}}(a + h_{I1} + h_{I2}) - B_{I2}\frac{1+\nu}{E_{I2}}(a + h_{I1} + h_{I2})^{-1} \\ &= A_{I3}\frac{1-\nu-2\nu^2}{E_{I3}}(a + h_{I1} + h_{I2}) - B_{I3}\frac{1+\nu}{E_{I3}}(a + h_{I1} + h_{I2})^{-1} \end{aligned} \tag{4.15}$$

$$\begin{aligned} &A_{I3}\frac{1-\nu-2\nu^2}{E_{I3}}(a + h_{I1} + h_{I2} + h_{I3}) - B_{I3}\frac{1+\nu}{E_{I3}}(a + h_{I1} + h_{I2} + h_{I3})^{-1} \\ &= A_{O3}\frac{1-\nu-2\nu^2}{E_{O3}}(a + h_{I1} + h_{I2} + h_{I3}) - B_{O3}\frac{1+\nu}{E_{O3}}(a + h_{I1} + h_{I2} + h_{I3})^{-1} \end{aligned} \tag{4.16}$$

$$\begin{aligned} &A_{O3}\frac{1-\nu-2\nu^2}{E_{O3}}(a + h_{I1} + h_{I2} + h_{I3} + h_{O3}) - B_{O3}\frac{1+\nu}{E_{O3}}(a + h_{I1} + h_{I2} + h_{I3} + h_{O3})^{-1} \\ &= A_{O2}\frac{1-\nu-2\nu^2}{E_{O2}}(a + h_{I1} + h_{I2} + h_{I3} + h_{O3}) - B_{O2}\frac{1+\nu}{E_{O2}}(a + h_{I1} + h_{I2} + h_{I3} + h_{O3})^{-1} \end{aligned} \tag{4.17}$$

$$A_{O2}\frac{1-\nu-2\nu^2}{E_{O2}}\left(a+h_{I1}+h_{I2}+h_{I3}+h_{O3}+h_{O2}\right)-B_{O2}\frac{1+\nu}{E_{O2}}\left(a+h_{I1}+h_{I2}+h_{I3}+h_{O3}+h_{O2}\right)^{-1}$$
$$=A_{O1}\frac{1-\nu-2\nu^2}{E_{O1}}\left(a+h_{I1}+h_{I2}+h_{I3}+h_{O3}+h_{O2}\right)-B_{O1}\frac{1+\nu}{E_{O1}}\left(a+h_{I1}+h_{I2}+h_{I3}+h_{O3}+h_{O2}\right)^{-1} \quad (4.18)$$

The 12 unknowns (A_i and B_i) should satisfy the twelve boundary conditions defined by Eqs. (4.7)-(4.18). For a given shrinkage d, the radial stress and displacement distributions across the HFM can be predicted using Eqs. (4.2) and (4.6).

4.2 Buckling mode estimation

Based on the proposed six-layer HFM model, the shrinkage-induced inward pressure along the I_1/I_2 interface can be calculated as follows

$$P=-\sigma_{rr}\big|_{r=a+h_{I1}}=-\left[A_{I1}+B_{I1}\left(a+h_{I1}\right)^{-2}\right] \quad (4.19)$$

Under the effect of inward pressure, the inner elastic skin layer may buckle if the resulting pressure is higher than the critical pressure, P_{cr}, which can be determined by applying a classical instability theory [Timoshenko1961] to the inner skin layer considered as a thin-walled elastic cylindrical shell

$$P_{cr}=\frac{E_{I1}{h_{I1}}^3\left(n^2-1\right)}{12a^3\left(1-\nu^2\right)} \quad (4.20)$$

In Eq. (4.20) n is the buckling mode (the number of circumferential waves). Under a sufficient high process-induced pressure difference $P-p_0$, the inner skin layer buckling mode can be obtained based on Eq. (4.20) as follows

$$n=\sqrt{\frac{12a^3\left(1-\nu^2\right)\left(P-p_0\right)}{E_{I1}{h_{I1}}^3}+1} \qquad (4.21)$$

The whole procedure for groove number prediction is shown in Fig. 4.2.

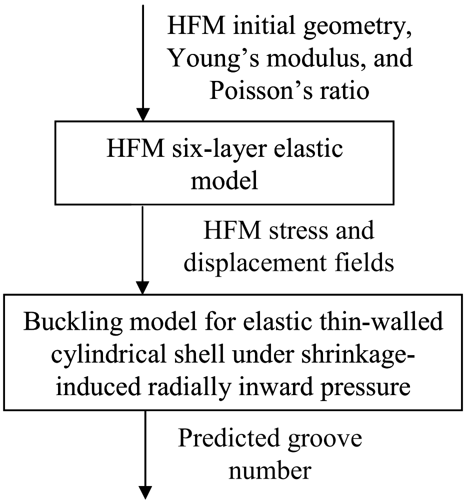

Fig. 4.2. Groove number prediction flowchart.

4.3 Model validation and discussion

4.3.1 Parameters selection and modeling results

The model presented above is used to predict the influence of air gap distance on groove number of PAN/DMSO/water HFMs in Chapter 2. For different air gap lengths, $\nu = 0.3$ [Cabasso1976] is assumed to be constant [Bonyadi2007]. The Young's modulus of each layer is defined as:

$$\frac{E_{I2}}{E_{I1}}={\eta_1}^{-1},\ \frac{E_{I3}}{E_{I1}}={\eta_2}^{-1},\ \frac{E_{O3}}{E_{I1}}={\eta_3}^{-1},\ \frac{E_{O2}}{E_{I1}}={\eta_4}^{-1},\ \text{and}\ \frac{E_{O1}}{E_{I1}}={\eta_5}^{-1} \qquad (4.22)$$

The thickness of each layer/sublayer h_{Mj} ($M = I$, and O, and j = 1, 2, and 3) can be determined from the SEM images, and E_{ave} is measured. Their different values are listed in Table 4.1. The Young's modulus ratio η_i in Eq. (4.22) is approximated from the examination of the microstructures of the corresponding layer and its porosity [Arnold1996]. The relation between the average Young's modulus E_{ave} and the Young's modulus of each layer/sublayer can be written as:

$$E_{ave} = \frac{\sum_{j=1}^{3} E_{Ij} A_{Ij} + \sum_{j=1}^{3} E_{Oj} A_{Oj}}{\sum_{j=1}^{3} \left(A_{Ij} + A_{Oj}\right)},$$

$$A_{Ij} = \pi\left[\left(r + \sum_{k=1}^{j} h_{Ik}\right)^2 - \left(r + \sum_{k=1}^{j-1} h_{Ik}\right)^2\right],$$

$$A_{O3} = \pi\left[\left(r + h_{O3} + \sum_{k=1}^{3} h_{Ik}\right)^2 - \left(r + \sum_{k=1}^{3} h_{Ik}\right)^2\right], \tag{4.23}$$

$$A_{O2} = \pi\left[\left(r + h_{O3} + h_{O2} + \sum_{k=1}^{3} h_{Ik}\right)^2 - \left(r + h_{O3} + \sum_{k=1}^{3} h_{Ik}\right)^2\right], \text{ and}$$

$$A_{O1} = \pi\left[(r + h)^2 - (r + h - h_{O1})^2\right]$$

where A_{Ij} and A_{Oj} are the area of the j inner and outer sublayers, respectively. Based on Eqs. (4.22) and (4.23), the thicknesses, the Young's modulus ratios, and the Young's modulus of each layer, particularly of the inner layer, can be obtained.

Table 4.1. Prediction of groove number under different air gap distances. (Nonsolvent flow rate 2 ml/min, polymer solution flow rate 1 ml/min, and polymer concentration 7 w/w%; for 5 cm air gap: $E_{I1}/E_{I2} = 5$, $E_{I1}/E_{I3} = 125$, $E_{I1}/E_{O3} = 200$, $E_{I1}/E_{O2} = 5$, and $E_{I1}/E_{O1} = 1$; and for 20 cm air gap: $E_{I1}/E_{I2} = 5$, $E_{I1}/E_{O3} = 200$, and $E_{I1}/E_{O1} = 1.25$).

Air gap distance	**5 cm**		**20 cm**	
Inner radius r (mm)	0.548		0.346	
Estimated thickness of each layer h_i (μm)	136	$I_1 = 3.9$	98	$I_1 = 4.7$
		$I_2 = 11.9$		$I_2 = 13.6$
		$I_3 = 41.9$		$O_3 = 70.4$
		$O_3 = 48.0$		$O_1 = 9.3$
		$O_2 = 22.0$		
		$O_1 = 8.3$		
$\frac{r}{h_{I1}}$	141		68	
Measured Shrinkage of outer surface (μm)	8.2		7.8	
Measured Young's modulus E (Pa)	2.0×10^7		3.6×10^7	
Estimated E_{I1} (Pa)	1.4×10^8		2.3×10^8	
Calculated pressure difference P-p_0 (Pa)	847		23726	
Calculated $\frac{P-p_0}{E_{I1}}$	6.3×10-6		1.0×10-4	
Groove number : experimental result	12		22	
Groove number: modeling result	13		21	

To show the effect of air gap, two air gap scenarios are considered: 5 cm (Fig. 2.6B) and 20 cm (Fig. 2.6D). The examination of the HFM morphologies shows that the sublayer I_2 (or O_2) is more porous than the skin layer I_1 (or O_1), and the sublayer I_3 (or O_3) is more porous than the sublayer I_2 (or O_2) (Fig. 2.6), so it is concluded that the ratio η_i

increases from layer 1 to layer 3. With a 5 cm air gap, the morphology is more symmetric, so the stiffness of the inner and outer skin layers is set as $\frac{E_{I1}}{E_{O1}} = 1$. The sublayers I_2 and O_2 are softer than the skin layers I_1, so it is assumed that $\frac{E_{I1}}{E_{I2}} = \frac{E_{I1}}{E_{O2}} = 5$. The sublayers I_3 and O_3 are more porous than the layer I_1, and based on Fig. 2.6B, where the macrovoids in O_3 are larger than those in I_3, so it is assumed $\frac{E_{I1}}{E_{O3}} > \frac{E_{I1}}{E_{I3}} \sim 100$. The values to be adopted are $\frac{E_{I1}}{E_{I3}} = 125$, and $\frac{E_{I1}}{E_{O3}} = 200$. As seen from Fig. 2.6, the morphology varies significantly under the air gap distances of 5 and 20 cm. In the case of 20 cm air gap distance, the six-layer structure reduces to a four-layer structure, and the two outer sublayers O_2 and O_3 merging with the inner layer I_3. It can be observed that both inner and outer skin layers become thicker. It can also be noticed that due to the longer precipitation time of inner surface, the inner skin is stiffer than the outer skin. It is assumed that $\frac{E_{I1}}{E_{O1}} = 1.25$ while the other two ratios are chosen as in the case of a 5 cm air gap distance as specified in Table 4.1. By comparing the HFM outer diameter just before and after entering the coagulation bath, the shrinkage of the outer layer was measured and is about 8 μm for both cases. Table 4.1 lists measurements and predictions using Eq. (4.21).

As observed, the inner radius of HFM r decreases with the air gap distance, so the $\frac{r}{h_{I1}}$ ratio also decreases as expected. With a longer air gap, the middle sublayers become stiffer due to a long precipitation time, thus less stress caused by the shrinkage of outer surface can be absorbed by the middle sublayers, leading to a larger pressure difference P-p_0. The multilayer model developed for six-layer HFMs can be applied for the 5 cm air gap scenario and also can be adapted to four-layer HFMs fabricated using a 20 cm air gap by introducing four layers instead of six. The pressure differences P-p_0 deduced from the multilayer buckling model and the corresponding ratios $\frac{P-p_0}{E_{I1}}$ are listed in Table 4.1. There is a significant increase in $\frac{P-p_0}{E_{I1}}$ with the air gap distance, and the groove number determined from the buckling model (Eq. 4.21) also increases. Table 4.1 shows a good agreement between the results obtained from the model predictions and the experimental observations, supporting the validity of the proposed groove formation mechanism and modeling approach.

4.3.2 Discussion

The results show that for a very short air gap distance (1 cm) the inner surface is smooth, but as the air gap distance increases from 3 to 20 cm the number of grooves increases (Fig. 2.5A). The multilayer buckling model can also predict the increase of the groove number with the air gap distance as shown in Table 4.1. However, Shi *et al.* [Shi2007] and Bonyadi *et al.* [Bonyadi2007] had different observations regarding the effect of air gap and found that HFMs may have irregular inner surfaces in the absence of air gap, and may become smooth as the air gap increases.

Shi *et al.* [Shi2007] considered the high viscoelasticity of PVDF-HFP as one of factors responsible for the irregularities of the inner surface of the membrane. The orientation of the macromolecules induced by shear in the spinneret is frozen during phase inversion, and a partial release of the stress in the transverse direction contributes to the deformation of the inner contour. As the air gap increases, more relaxation and rearrangement of the macromolecules lead to a smoother inner surface. It was concluded that grooves are initiated in the coagulation bath. This interpretation might be suitable for PVDF-HFP HFMs. However in this study, no grooves formed under a very short air gap and the number of grooves increases as the air gap increases. Once the polymer solution and inner nonsolvent solution are brought into contact at the spinneret outlet, a solutal Marangoni instability induced by the solvent extraction from the polymer solution may occur as discussed in Chapter 3. So it could be deduced that the grooves may be initiated in the air gap instead of the coagulation bath. But in case of the PAN/DMSO solution, the interfacial tension between nonsolvent and polymer solution depends weakly on PAN concentration [Weh2004]. Due to the rapid solidification in the air gap, the interfacial instability does not have enough time to develop; as a result, the inner surface remains circular in the air gap until the nascent fiber enters the coagulant bath.

Bonyadi *et al*. [Bonyadi2007] reported that a longer air gap tends to reduce the groove number indicating a different effect of the air gap distance on the shape of the inner surface. But the deformed HFMs reported by Bonyadi *et al.* exhibit large deformations with a small number of lobes, characterizing the deformations of the whole HFM structure instead of the deformations of only a thin sublayer of the HFM structure, observed in this work. Bonyadi *et al.* also explained the inner surface deformation by introducing the buckling of a thin inner skin layer in a six-layer structure without considering the effect of other layers. They pointed out that a longer air gap distance will decrease the inner radius r and increase the Young's modulus of inner skin layer E_{I1}. However, the thickness h_{I1} and the Young's modulus of the inner layer E_{I1} also need to be carefully determined and the pressure difference P-p_0 has to be calculated for each air gap distance. Moreover, it is observed in the experimental study that the air gap distance can also influences the number of layer/sublayer and the morphology, such as the location of macrovoids and the appearance of fingerlike layers. Therefore, the multilayer model in this work can predict the variation of shrinkage-induced pressure P on the I_1/I_2 interface due to the change in the air gap distance. As the air gap distance increases, a slight decrease of $\frac{r}{h_{I1}}$ is observed, and a significant increase of $\frac{P-p_0}{E_{I1}}$ is calculated, modeling the fast solidification, the predominant factor for the groove number determination. As the morphology variations and the pressure changes were not taken into account in Bonyadi *et al.*'s work, their model is not relevant to this study. Since different variations of $\frac{r}{h_{I1}}$ and $\frac{P-p_0}{E_{I1}}$ may be caused by different fluids, spinneret design, flow rates, and concentrations, the different contributions have to be carefully controlled to understand how and why the groove number varies.

4.4 Summary

In Chapter 4, a shrinkage-induced multilayer buckling model is developed for a thin-walled elastic cylindrical shell under a uniform, radially inward pressure. The model is used to predict the buckling modes and to study the influence of air gap distance on groove number of PAN/DMSO/water HFMs. The groove number has been determined by taking into account the changes in the morphology, the thickness and Young's modulus of each layer/sublayer. A reasonable prediction of accuracy of the groove numbers and the tendencies were observed, which can validate this theoretical model in PAN/DMSO/water HFM fabrication.

CHAPTER FIVE

STUDY OF SUBSTRATE GEOMETRY EFFECT ON AXONAL OUTGROWTH

In this chapter, a numerical model of axonal outgrowth on a grooved substrate is developed to study the influence of the substrate geometry. The axon, outgrowing at a very slow speed (of the order of 10^{-8} m/s [Zhang2005]) along a 3D grooved substrate of the nerve conduit, is modeled as a 1D elastic beam. The Cosserat theory is introduced to model the nonplanar deformation and motion of the axon. The 3D deformation of axon, under the effect of friction and external traction force, is solved using the finite element method. The proposed modeling approach is validated by comparing the results with the experimental results in the literature. Finally, the conclusions are drawn.

Numerous experimental investigations have proved the effectiveness of the micropatterned 3D structure in promoting nerve regeneration with tubular nerve conduits made from poly($_{\mathrm{D,L}}$-lactic acid) (PDLLA) [Rutkowski2004], poly($_{\mathrm{D,L}}$-lactic) (PLA) [Hsu2007], and PU [Zhang2005]. The existing axonal outgrowth models are 1D [O'Toole2008] or 2D [Aeschlimann2000]. For the 3D grooved substrate, a 3D model is needed and neither of the aforementioned modeling approaches can work. In order to fully understand the outgrowth of an axon on a 3D grooved substrate, a model describing the motion and deformation of an axon in the 3D space needs to be developed.

5.1 Assumptions and kinematic description

The Cosserat model is a geometrically exact model which concerns the nonplanar dynamics of an extensional and twistable beam [Antman1995] and which is generally used to model the motion of various 1D slender objects such as hair and wire [Chang2007]. The motion of any slender 3D body is characterized by the motion of its line of centroids as well as the rotation of its different cross sections. With the Cosserat model, the study of a beam motion and deformation requires the determination of three vector fields, one for the line of centroids and two for the rotation of the cross sections. The model is implemented to describe the 3D motion and deformation of the axon on a 3D grooved substrate.

5.1.1 Assumptions

There are generally two driving mechanisms explaining how axon elongates. The first one, taking place along the axon, is called “stretch outgrowth” [Franze2010]. As the axon moves on the substrate, the growth cone may experience an adhesion force from the substrate, generating a traction force [Ananthakrishnan2007] stretching the axon. The second one is called “tip outgrowth”. It is due to microtubules polymerization at the distal end of the axon [van Veen1994], called the tip, and as time evolves a new mass is added there [O'Toole2008, Franze2010]. During the outgrowth process, the proximal part of the axon remains firmly attached to the substrate, while the distal part of the axon moves [Chang1998].

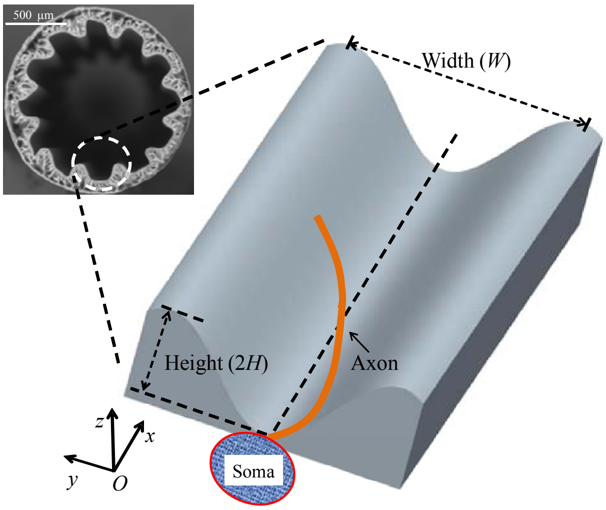

Fig. 5.1. The schematic of an axonal outgrowth on a grooved substrate, substrate geometry being characterized by its width W and height $2H$.

As shown in Fig. 5.1, an axon grows on a substrate with grooves characterized by their longitudinal direction x, their width W and height $2H$. The substrate, as a cylindrical surface whose axis is parallel to the x-direction, is defined as:

$$z = F(y) \tag{5.1}$$

where $F(\cdot)$ is a fully smooth function. In order to simulate the axon outgrowth process, some assumptions are made:

(a) The axon is modeled as a 1D beam. In the previous experimental studies, the groove widths of the textured nerve conduits vary from 10 to 100 μm. The groove width is 10 μm in [Rutkowski2004], while it is 20 μm in [Hsu2007]. These two grooved nerve conduits were fabricated by casting polymer on a grooved master wafer for a better control of the groove width. The grooved nerve conduits formed by process-induced instability have a width around 50 μm [Zhang2005]. All these nerve conduits were demonstrated to enhance the nerve regeneration. The groove width to be considered in this study varies between 10 to 100 μm and the chosen width in the numerical part of this work is on the order of 100 μm. Since the radius of an axon is usually less than 0.5 μm [Aeschlimann2000], the length larger than 10 μm and the ratio of the axonal diameter to the groove width about 0.01, a 1D model for the axon growthing on this grooved geometry is justified;

(b) The axonal motion is considered as quasi-static [Aeschlimann2000], and this assumption will be further discussed later;

(c) The substrate is rigid;

(d) During the outgrowth, the axon remains in the same groove in contact with the substrate. Though, some studies reported that neurons can bridge their neurites over the groove [Johansson2006], this assumption follows the experimental results from [Li2005] that for groove height greater than 11 μm and groove width 100 μm, axons of E11-E14 mouse embryos will remain inside one groove;

(e) The axon itself is modeled as an elastic material [Aeschlimann2000], and there is an inelastic elongation at the tip, which is proportional to the external force exerted at the distal tip [Heidemann1994]. Therefore the behavior of axon can be considered as viscoelastic.

5.1.2 Kinematic description and representation of the rotation

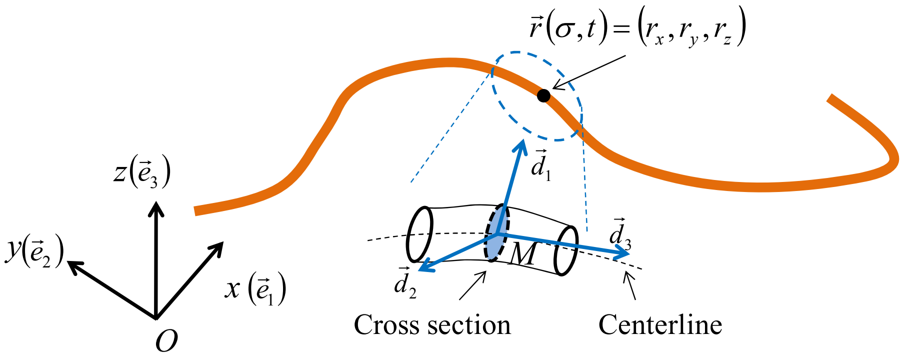

Fig. 5.2. The schematic of Cosserat theory.

The Bernoulli hypothesis is adopted. Any cross section of the axon is considered as rigid, therefore any cross section in a 3D space depends on six parameters: three for translation and three for rotation. The translation specifies the position of the centroid of a cross section with respect to a given frame of reference (O, $\vec{e}_1$, $\vec{e}_2$, $\vec{e}_3$). The configuration of the line of centroids at time *t* is defined by $\vec{r}(\sigma,t)=(r_x,r_y,r_z)$, a function of curvilinear abscissa $\sigma\in[0,1]$ and time *t*. The deformation and rotation of any cross section can be described in terms of the rotation of a moving frame of reference (*M*, $\vec{d}_1$, $\vec{d}_2$, $\vec{d}_3$) called the local frame of reference, $\vec{d}_1$ and $\vec{d}_2$ are in the plane of the cross section as shown in Fig. 5.2 and $\vec{d}_3=\vec{d}_1\times\vec{d}_2$ is assumed to be tangent to the line of centroids.

Based on the vectors introduced above, the deformation can be defined as follows [Antman1995]. The translational velocity

$$\vec{v}_t=\frac{\partial\vec{r}(\sigma,t)}{\partial t}\hat{=}\dot{\vec{r}} \tag{5.2}$$

is associated to the motion of the line of centroids and the translational strain vector

$$\vec{v}_\sigma=\frac{\partial\vec{r}(\sigma,t)}{\partial\sigma}\hat{=}\vec{r}\,' \tag{5.3}$$

associated to its stretching, while associated to the rotation of the cross sections is the temporal derivative of the directors $\vec{d}_p$ (p = 1, 2, 3)

$$\dot{\vec{d}}_p=\frac{\partial\vec{d}_p(\sigma,t)}{\partial t}=\vec{\omega}\times\vec{d}_p \tag{5.4}$$

where $\vec{\omega}$ is the angular velocity vector of the local frame with respect to the reference frame and the “spatial” derivative of the directors $\vec{d}_p$ expressing the change in orientation of the cross section along the line of centroids

$$\vec{d}_p{}' \hat{=} \frac{\partial \vec{d}_p(\sigma,t)}{\partial \sigma} = \vec{u} \times \vec{d}_p \tag{5.5}$$

where $\vec{u}$ is the rotational strain vector. The basis ($\vec{d}_1$, $\vec{d}_2$, $\vec{d}_3$) being orthonormal, it can be deduced that:

$$\sum_{p=1}^{3}\left(\vec{d}_p \times \dot{\vec{d}}_p\right) = \sum_{p=1}^{3}\left[\vec{d}_p \times \left(\vec{\omega} \times \vec{d}_p\right)\right] = \sum_{p=1}^{3}\left[\left(\vec{d}_p \cdot \vec{d}_p\right)\vec{\omega} - \left(\vec{d}_p \cdot \vec{\omega}\right)\vec{d}_p\right] = 3\vec{\omega} - \vec{\omega} = 2\vec{\omega} \tag{5.6}$$

leading to an expression of $\vec{\omega}$ in terms of $\vec{d}_p$ and its time derivative $\dot{\vec{d}}_p$ (p = 1, 2, 3)

$$\vec{\omega} = \frac{1}{2}\sum_{p=1}^{3}\left(\vec{d}_p \times \dot{\vec{d}}_p\right) \tag{5.7}$$

A similar expression can be obtained for the rotational strain vector

$$\vec{u} = \frac{1}{2}\sum_{p=1}^{3}\left(\vec{d}_p \times \vec{d}_p{}'\right) \tag{5.8}$$

The $\vec{d}_p$ components of $\vec{\omega}$ and $\vec{u}$ are denoted by ω_p and u_p (p = 1, 2, 3) respectively.

The orientation of any cross section, at each time t depends on the rotation of the local frame of reference ($\vec{d}_1$, $\vec{d}_2$, $\vec{d}_3$), where $\vec{d}_3$ is normal to the cross section and $\vec{d}_1$ *and* $\vec{d}_2$ lie in its plane. Several approaches exist to represent the rotation, such as Euler angles, the rotational vector and the unit quaternion. The unit quaternions were chosen to avoid singularities and develop straightforward and systematic method to determine the rotation from the angular velocity. Background on quaternions can be found in Zupan *et al.* [Zupan2009]. A quaternion is defined as the sum of a vector and a scalar and can be expressed as:

$$\hat{q} = q_1 \vec{e}_1 + q_2 \vec{e}_2 + q_3 \vec{e}_3 + q_4 = \vec{q} + q_4 \tag{5.9}$$

Operations on quaternions make the set of quaternions an algebra, the multiplication leading to the definition of a norm as:

$$\|\hat{q}\| = \sqrt{|\vec{q}|^2 + q_4^2} \tag{5.10}$$

and consequently to the polar form of any quaternion:

$$\hat{q} = \|\hat{q}\|(\vec{q}_n \sin\theta + \cos\theta), \quad \cos\theta = \frac{\mathrm{q}_4}{\|\hat{q}\|}, \ \vec{q}_n = \frac{\vec{q}}{\|\vec{q}\|} \tag{5.11}$$

where $\vec{q}_n$ is a unit vector. A unit quaternion is such that:

$$q_1^2 + q_2^2 + q_3^2 + q_4^2 = 1 \tag{5.12}$$

and can be expressed as:

$$\hat{q} = \vec{w}\sin(\phi/2) + \cos(\phi/2) \tag{5.13}$$

and describes any rigid rotation where $\vec{w}$ is a unit vector along the axis of rotation, and ϕ is the rotation angle. The quaternion depends on three independent parameters as a rotation in the 3D space.

The rotation between two orthonormal bases ($\vec{e}_1$, $\vec{e}_2$, $\vec{e}_3$) and ($\vec{d}_1$, $\vec{d}_2$, $\vec{d}_3$) can be obtained in terms of the matrix [*R*] [Zupan2009]

$$[R] = \begin{bmatrix} q_1^2 - q_2^2 - q_3^2 + q_4^2 & 2(q_1q_2 - q_3q_4) & 2(q_1q_3 + q_2q_4) \\ 2(q_1q_2 + q_3q_4) & -q_1^2 + q_2^2 - q_3^2 + q_4^2 & 2(q_2q_3 - q_1q_4) \\ 2(q_1q_3 - q_2q_4) & 2(q_2q_3 + q_1q_4) & -q_1^2 - q_2^2 + q_3^2 + q_4^2 \end{bmatrix} \tag{5.14}$$

with the components R_{pq} defined as the components of the $\vec{d}_p$ vectors in the basis ($\vec{e}_1$,

$\vec{e}_2$, $\vec{e}_3$)

$$\vec{d}_p = \sum_{q=1}^{3} R_{qp}\vec{e}_q \tag{5.15}$$

expressed also as

$$\vec{d}_1 = \begin{bmatrix} q_1^2 - q_2^2 - q_3^2 + q_4^2 \\ 2(q_1q_2 + q_3q_4) \\ 2(q_1q_3 - q_2q_4) \end{bmatrix},\ \vec{d}_2 = \begin{bmatrix} 2(q_1q_2 - q_3q_4) \\ -q_1^2 + q_2^2 - q_3^2 + q_4^2 \\ 2(q_2q_3 + q_1q_4) \end{bmatrix},\ \vec{d}_3 = \begin{bmatrix} 2(q_1q_3 + q_2q_4) \\ 2(q_2q_3 - q_1q_4) \\ -q_1^2 - q_2^2 + q_3^2 + q_4^2 \end{bmatrix} \tag{5.16}$$

Thus, the components of $\vec{u}$ and $\vec{\omega}$ (Eqs. 5.7 and 5.8) can be expressed in the local frame as (p = 1, 2, 3)

$$u_p = \vec{u} \cdot \vec{d}_p = 2([B_p][q])^T \cdot [q'] \tag{5.17}$$

$$\omega_p = \vec{\omega} \cdot \vec{d}_p = 2([B_p][q])^T \cdot [\dot{q}] \tag{5.18}$$

where $[q]$ is the 4×1 matrix of components q_k (k = 1 to 4), associated to $\hat{q}$, and $[q']$, $[\dot{q}]$, $[\delta q]$ are the 4×1 matrices associated to the quaternions $\hat{q}'$, $\dot{\hat{q}}$, and $\delta\hat{q}$. The different matrices $[B_p]$ (p = 1, 2, 3), and the derivation of Eqs. (5.17) and (5.18) are given in Appendix B.

5.2 Governing equations and numerical model

5.2.1 Governing equations for axon elastic deformation

As the axonal outgrowth process is assumed quasi-static (Assumption b), the equations of motion to be considered obtained based on the virtual work principle, are the equilibrium equations. The virtual work due to internal forces δW_I is

$$\delta W_I = -\delta U = -(\delta U_s + \delta U_b) \tag{5.19}$$

where U is the strain energy of the axon, U_s its stretching energy, and U_b its bending and torsional energy. Specifically,

$$U_s = \frac{1}{2}\int_0^1 K_s\left(\|\vec{r}'\| - 1\right)^2 d\sigma \tag{5.20}$$

$$U_b = \frac{1}{2}\int_0^1 \sum_{p=1}^{3}\left(K_p u_p{}^2\right) d\sigma \tag{5.21}$$

where

$$K_s = E\pi R^2,\ \ K_1 = K_2 = \frac{E\pi R^4}{4},\ \ K_3 = \frac{G\pi R^4}{2} \tag{5.22}$$

E is the Young's modulus of the axon, R its radius, G its shear modulus. Here, the axon cross section is assumed circular, and the axon is considered elastic (Assumption e).

During the stretch outgrowth, the external forces experienced by the axon include the interaction force between the axon and the substrate and the external outgrowth force exerted at the tip of axon $\vec{f}_N$, which will be discussed later. The interaction between the axon and the substrate is mainly due to friction [Aeschlimann2000, O'Toole2008]. This friction force per unit length $\vec{F}_f$ is assumed to be proportional to the axon velocity [O'Toole2008]:

$$\vec{F}_f = -\mu_1 \dot{\vec{r}} \tag{5.23}$$

where μ_1 is the first constant of friction. The friction moment per unit length $\vec{M}_f$ is also assumed to be proportional to the angular velocity of the axonal cross section as:

$$\vec{M}_f = -\mu_2 \vec{\omega} \tag{5.24}$$

where μ_2 is the second constant of friction. Therefore, the virtual work of all the external forces is

$$\delta W_E = \int_0^1 \left(\vec{F}_f \cdot \delta\vec{r} + \vec{M}_f \cdot \delta\vec{\varphi} \right) d\sigma + \vec{f}_N \cdot \delta\vec{r}_T \tag{5.25}$$

where $\delta\vec{r}$, $\delta\vec{\varphi}$ are the virtual displacement and virtual rotation at any point M on the line of centroids, and $\delta\vec{r}_T$ is the virtual displacement of the axon tip.

The virtual displacements are chosen compatible with the constraints. First, $\hat{q}$ is a unit quaternion, so q_k ($k = 1$ to 4) satisfy Eq. (5.12)

Second, due to the Bernoulli hypothesis, the unit vector $\vec{d}_3$ normal to the cross section is tangent to the axon line of centroids, so

$$\vec{d}_3 = \frac{\vec{r}\,'}{\|\vec{r}\,'\|} \tag{5.26}$$

By applying the virtual work principle, the translational velocity and the angular velocity are obtained for any given time t, and this velocity information is used to update the axon configuration.

5.2.2 Numerical simulation

The axon is modeled as a 1D beam moving on the substrate. In order to numerically solve the problem and obtain the axon motion at any time, a finite element approach is used. The line of centroids is divided into elements, and the nodes are shown in Fig. 5.3. The position of the *i*th (i = 1 to N) node along the centerline is defined by the vector $\vec{r}_i = \left(r_{xi}, r_{yi}, r_{zi}\right)$, and the rotation of the *j*th (j = 1 to N-1) segment is defined by the quaternion $\hat{q}_j = \left\{q_{1j}, q_{2j}, q_{3j}, q_{4j}\right\}$ at the midpoint of this segment. Consequently, the axon configuration is described at time t by $\vec{r}_i$ (i = 1 to N) and $\hat{q}_j$ (j = 1 to N-1). Since the axon is always in contact with the substrate in this study (Assumption d), the z component of $\vec{r}_i$ is such that $r_{zi} = F\left(r_{yi}\right)$ (Eq. 1), the *i*th node is thus defined by two independent components r_{xi} and r_{yi} as $\left(r_{xi}, r_{yi}, F\left(r_{yi}\right)\right)$.

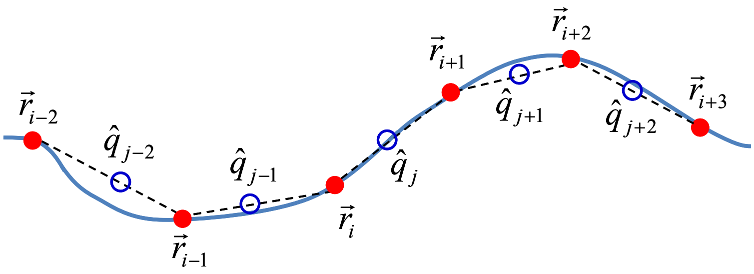

Fig. 5.3. Discretization of axon centerline.

The discrete spatial derivatives are approximated as

$$\vec{r}_i' \approx \frac{\vec{r}_{i+1}-\vec{r}_i}{l_i}\text{, and }\ \hat{q}_j' \approx \frac{\hat{q}_{j+1}-\hat{q}_j}{l_j^q} \tag{5.27}$$

with the lengths l_i and l_j^q defined as:

$$l_i \approx \left\|\vec{r}_{i+1}^{\,t=0}-\vec{r}_i^{\,t=0}\right\| \ \text{ and }\ l_j^q \approx \frac{1}{2}\left(l_{j+1}+l_j\right) \tag{5.28}$$

which are obtained based on the initial configuration (t = 0). For each segment, the constant shape functions are used

$$\overline{\vec{r}_i(\sigma)}=\frac{\vec{r}_{i+1}+\vec{r}_i}{2}\ \text{ and }\ \overline{\hat{q}_j(\sigma)}=\frac{\hat{q}_{j+1}+\hat{q}_j}{2} \tag{5.29}$$

Therefore, the stretching energy of the *j*th segment is expressed as

$$U_{sj}=\frac{1}{2}\int_0^{l_j} K_s\left(\left\|\vec{r}_j'\right\|-1\right)^2 d\sigma=\frac{K_s l_j}{2}\left(\frac{1}{l_j}\left\|\vec{r}_{j+1}-\vec{r}_j\right\|-1\right)^2 \tag{5.30}$$

Substituting Eq. (5.17) into Eq. (5.21), the bending and torsional energy of the *j*th segment becomes

$$\begin{aligned} U_{bj} &= \frac{1}{2}\int_0^{l_j^q}\sum_{p=1}^{3}\left(K_p u_{pj}^{\;2}\right)d\sigma=\frac{1}{2}\int_0^{l_j^q}\sum_{p=1}^{3}K_p\left\{2\left(\left[B_p\right]\left[q_j\right]\right)^T\cdot\left[q_j'\right]\right\}^2 d\sigma \\ &= \frac{l_j^q}{2}\sum_{p=1}^{3}K_p\left\{\left[\left[B_p\right]\left(\left[q_{j+1}\right]+\left[q_j\right]\right)\right]^T\cdot\frac{\left[q_{j+1}\right]-\left[q_j\right]}{l_j^q}\right\}^2 \end{aligned} \tag{5.31}$$

By substituting Eqs. (5.30) and (5.31) into Eq. (5.19), the virtual work of internal forces is now

$$\delta W_I = -\frac{\partial U_{s1}}{\partial r_{x1}}\delta r_{x1} - \frac{\partial U_{s1}}{\partial r_{y1}}\delta r_{y1} - \left[\sum_{i=2}^{N-1}\left(\frac{\partial U_{s(i-1)}}{\partial r_{xi}} + \frac{\partial U_{si}}{\partial r_{xi}}\right)\delta r_{xi} + \left(\frac{\partial U_{s(i-1)}}{\partial r_{yi}} + \frac{\partial U_{si}}{\partial r_{yi}}\right)\delta r_{yi}\right] - \frac{\partial U_{s(N-1)}}{\partial r_{xN}}\delta r_{xN}$$
$$- \frac{\partial U_{s(N-1)}}{\partial r_{yN}}\delta r_{yN} - \left(\sum_{k=1}^{4}\frac{\partial U_{b1}}{\partial q_{k1}}\delta q_{k1}\right) - \left[\sum_{j=2}^{N-2}\sum_{k=1}^{4}\left(\frac{\partial U_{b(j-1)}}{\partial q_{kj}} + \frac{\partial U_{bj}}{\partial q_{kj}}\right)\delta q_{kj}\right] - \left(\sum_{k=1}^{4}\frac{\partial U_{b(N-2)}}{\partial q_{k(N-1)}}\delta q_{k(N-1)}\right)$$

(5.32)

The expressions of the different partial derivatives in Eq. (5.32) are given in Appendix B.

During simulation, the friction force is distributed over the nodes [Aeschlimann2000]. Thus, the friction force $\vec{f}_i$ on the *i*th node is expressed as:

$\vec{f}_i = -\eta_1 \dot{\vec{r}}_i$, ($i$ = 1 to N) (5.33)

where $\dot{\vec{r}}_i$ is the velocity of *i*th node, and η_1 is the first constant of friction used in simulation and the friction moment on the mid cross section of the *j*th segment $\vec{m}_j$ is

$\vec{m}_j = -\eta_2 \vec{\omega}_j$, ($j$ = 1 to N-1) (5.34)

where $\vec{\omega}_j$ is the angular velocity of *j*th segment, and η_2 is the second constant of friction used in simulation. The choice of η_1 and η_2 is discussed below. Therefore, the virtual work of external forces (in Eq. 5.25) can be expressed as:

$$\delta W_E = \left(\sum_{i=1}^{N}\vec{f}_i \cdot \delta\vec{r}_i\right) + \left(\sum_{j=1}^{N-1}\vec{m}_j \cdot \delta\vec{\varphi}_j\right) + \vec{f}_N \cdot \delta\vec{r}_N \qquad (5.35)$$

where $\delta\vec{r}_i$ is the virtual displacement of the *i*th node, $\delta\vec{r}_N = \delta\vec{r}_T$ and $\delta\vec{\varphi}_j = \sum_{p=1}^{3}\left\{2\left(\left[B_p\right]\left[q_j\right]\right)^T \cdot \left[\delta q_j\right]\right\}\vec{d}_{pj}$ is the virtual rotation of the *j*th segment. Thus, Eq. (5.35) can be rewritten as

$$\delta W_E = \left[\sum_{i=1}^{N} \left(f_{xi} \delta r_{xi} + f_{yi} \delta r_{yi} \right) \right] + \left(\sum_{j=1}^{N-1} \sum_{k=1}^{4} M_{kj} \delta q_{kj} \right) + \vec{f}_N \cdot \delta \vec{r}_N \tag{5.36}$$

All the generalized forces introduced in Eq. (5.36) are listed in Appendix B.

The first constraint, Eq. (5.12), is expressed for each segment as:

$$\left\| \hat{q}_j \right\| = {q_{1j}}^2 + {q_{2j}}^2 + {q_{3j}}^2 + {q_{4j}}^2 = 1 \tag{5.37}$$

This constraint can be satisfied by normalizing $\hat{q}_j$ at each time step as in [Spillman2007]. Based on Eqs. (5.16) and (5.27), the second constraint, Eq. (5.26) can be expressed on the jth segment in the component form as:

$$C_{1j} = \frac{r_{x(j+1)} - r_{xj}}{\left\| \vec{r}_{(j+1)} - \vec{r}_j \right\|} - 2\left(q_{1j} q_{3j} + q_{2j} q_{4j} \right) = 0 \tag{5.38}$$

$$C_{2j} = \frac{r_{y(j+1)} - r_{yj}}{\left\| \vec{r}_{(j+1)} - \vec{r}_j \right\|} - 2\left(q_{2j} q_{3j} - q_{1j} q_{4j} \right) = 0 \tag{5.39}$$

$$C_{3j} = \frac{r_{z(j+1)} - r_{zj}}{\left\| \vec{r}_{(j+1)} - \vec{r}_j \right\|} - \left(-{q_{1j}}^2 - {q_{2j}}^2 + {q_{3j}}^2 + {q_{4j}}^2 \right) = 0 \tag{5.40}$$

Because of the constraints (Eqs. 5.36-5.38), the virtual work principle reads now

$$\delta W_I + \delta W_E + \sum_{j=1}^{N-1} \left(\lambda_{1j} \delta C_{1j} + \lambda_{2j} \delta C_{2j} + \lambda_{3j} \delta C_{3j} \right) = 0 \tag{5.41}$$

for any virtual displacement (δr_{xi}, δr_{yi}) and (δq_{1j}, δq_{2j}, δq_{3j}, δq_{4j}), λ_{1j}, λ_{2j}, and λ_{3j} being the Lagrange multipliers, and

$$\begin{aligned} \sum_{j=1}^{N-1} \lambda_{mj} \delta C_{mj} = {} & \lambda_{m1} \left(\frac{\partial C_{m1}}{\partial r_{x1}} \delta r_{x1} + \frac{\partial C_{m1}}{\partial r_{y1}} \delta r_{y1} \right) + \left[\sum_{j=2}^{N-1} \left(\lambda_{m(j-1)} \frac{\partial C_{m(j-1)}}{\partial r_{xj}} + \lambda_{mj} \frac{\partial C_{mj}}{\partial r_{xj}} \right) \delta r_{xj} + \left(\lambda_{m(j-1)} \frac{\partial C_{m(j-1)}}{\partial r_{yj}} + \lambda_{mi} \frac{\partial C_{mj}}{\partial r_{yj}} \right) \delta r_{yj} \right] \\ & + \lambda_{m(N-1)} \left(\frac{\partial C_{m(N-1)}}{\partial r_{xN}} \delta r_{xN} + \frac{\partial C_{m(N-1)}}{\partial r_{yN}} \delta r_{yN} \right) + \sum_{j=1}^{N-1} \left(\lambda_{mj} \sum_{k=1}^{4} \frac{\partial C_{mj}}{\partial q_{kj}} \delta q_{kj} \right), \qquad m = 1, 2, 3 \end{aligned} \tag{5.42}$$

Then the system of equations governing the motion is obtained from Eq. (5.41) with δW_I and δW_E given by Eqs. (5.32) and (5.36) and the constraints defined by Eqs. (5.38)-(5.40). Based on the current axonal configuration at time t, the governing equations give the velocities ($\dot{r}_{xi}$, $\dot{r}_{yi}$, $\dot{q}_{1j}$, $\dot{q}_{2j}$, $\dot{q}_{3j}$, and $\dot{q}_{4j}$), and the Lagrange multipliers (λ_{1j}, λ_{2j}, and λ_{3j}). Since the constraints (C_{1j}, C_{2j}, and C_{3j}) are satisfied at any time t, in order to determine the velocities at time t, Eqs. (5.38)-(5.40) are replaced by their derivatives with respect to t,

$$D_{mj} = \frac{\partial C_{mj}}{\partial r_{xj}}\dot{r}_{xj} + \frac{\partial C_{mj}}{\partial r_{yj}}\dot{r}_{yj} + \left(\sum_{k=1}^{4}\frac{\partial C_{mj}}{\partial q_{kj}}\dot{q}_{kj}\right) + \frac{\partial C_{mj}}{\partial r_{x(j+1)}}\dot{r}_{x(j+1)} + \frac{\partial C_{mj}}{\partial r_{y(j+1)}}\dot{r}_{y(j+1)} = 0,\ m = 1, 2, 3 \quad (5.43)$$

The new system of equations deduced from Eqs. (5.41) and (5.43) is numerically solved for the velocities. Once the velocities $\dot{r}_{xi}$ and $\dot{r}_{yi}$ and the temporal derivatives of quaternion ($\dot{q}_{1j}$, $\dot{q}_{2j}$, $\dot{q}_{3j}$, and $\dot{q}_{4j}$) are obtained, the axonal configuration at time t is updated as:

$$\vec{r}_i^{(t+\Delta t)} = \vec{r}_i^{\,t} + \dot{\vec{r}}_i\Delta t \quad \text{and} \quad \hat{q}_j^{(t+\Delta t)} = \hat{q}_j^{\,t} + \dot{\hat{q}}_j\Delta t \qquad (5.44)$$

5.2.3 External force at the axonal outgrowth tip

Previous results established that the contractile filopodia and lamellipodia [Trinkaus1985] and the cytoplasmic filling of the growth cone from the rear part of the axon [Franze2010] may result in a tension force, which causes stretch outgrowth at the axonal outgrowth tip. In addition, the traction force is generated by microtubules and actin filaments within the cytoskeleton structures to push and pull the neurite forward [Mahoney2005]. As so, the collective effect exerted by the growth cone on the axon is modeled as an external force $\vec{f}_N$, which is applied at the tip of the axon. On a planar substrate as shown in Fig. 5.4A, the external force $\vec{f}_N$ is always parallel to the surface, and its magnitude is assumed constant as $\left\|\vec{f}_N\right\| = 10^{-8}$ N. This value has been chosen of the same order of magnitude as the traction force introduced by Aeschlimann [Aeschlimann2000]. Considering the complex morphology and dynamic behavior of the growth cone, the traction force, exerted at the tip of the axon, is generally modeled as a random force on the planar surface [Forciniti2009]:

$$f_{Nx} = \left\|\vec{f}_N\right\| \sin\theta(t) \text{ and } f_{Ny} = \left\|\vec{f}_N\right\| \cos\theta(t) \tag{5.45}$$

where f_{Nx} and f_{Ny} are the components of $\vec{f}_N$ in the x and y directions, respectively. $\theta(t) \in [0, \pi]$ is a random, variant angle, describing the axon outgrowth orientation:

$$\begin{cases} \theta[0 \le t \le \Delta T] = \dfrac{\pi}{2}, \\ \theta[b\Delta T \le t \le (b+1)\Delta T] = \theta_b = \theta_{(b-1)} + \dfrac{\pi Ra}{10}, b = 1, 2, 3, \cdots\cdots \end{cases} \tag{5.46}$$

where $\Delta T = 10$ s is the time duration associated with the angle variation, θ_b is an angular variable, and $Ra \in [-0.5, 0.5]$ is a random number. In order to keep θ_b within the range of [0, π], the following condition is imposed: if $\theta_{(b-1)} + \frac{\pi Ra}{10} < 0$ or $\theta_{(b-1)} + \frac{\pi Ra}{10} > \pi$, then $\theta_b = \theta_{(b-1)} - \frac{\pi Ra}{10}$.

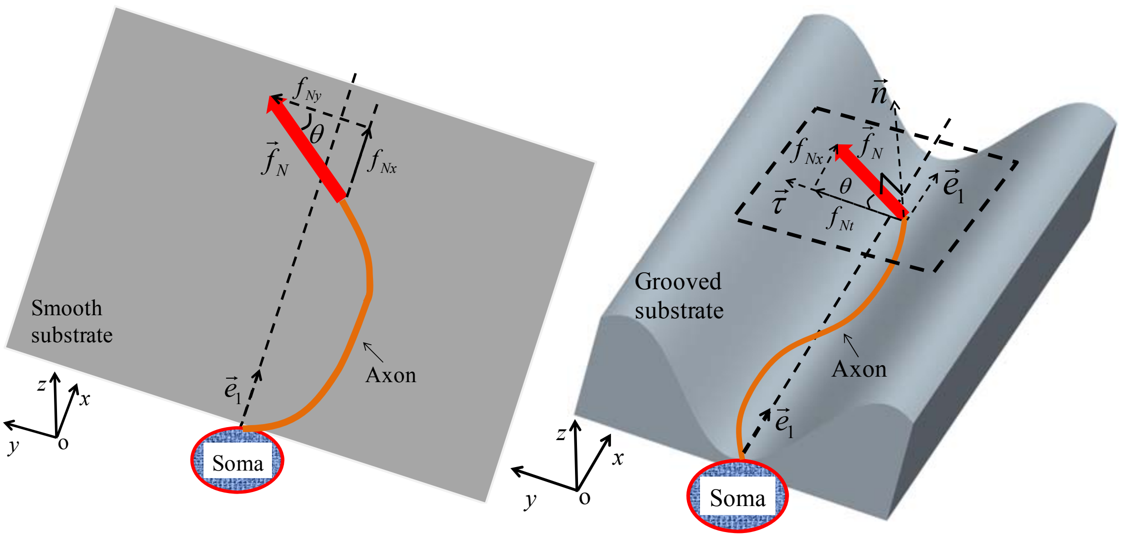

(A) (B)

Fig. 5.4. The force $\vec{f}_N$ for a planar surface (A) or for a grooved surface (B).

On the grooved substrate, since the axon always attaches to the substrate as assumed in this study, the normal component of the external force at the tip is balanced by the reaction force from the substrate. As so, the acting force $\vec{f}_N$ as show in Fig. 5.4B is tangential and defined as:

$$\vec{f}_N = f_{Nx}\vec{e}_1 + f_{N\tau}\vec{\tau} \tag{5.47}$$

where $\vec{e}_1$ is the longitudinal direction of the groove, and $\vec{\tau}$ is the direction in the tangent plane at the tip (*N*th node), normal to $\vec{e}_1$:

$$\vec{\tau} = (0, \tau_2, \tau_3) = \left(0, \frac{1}{\sqrt{1+\left(\frac{dr_z}{dr_y}\right)_N^2}}, \frac{\left(\frac{dr_z}{dr_y}\right)_N}{\sqrt{1+\left(\frac{dr_z}{dr_y}\right)_N^2}} \right) \tag{5.48}$$

where $\left(\frac{dr_z}{dr_y}\right)_N$ is calculated at the *N*th node, and the unit vectors here ($\vec{e}_1$, $\vec{e}_2$, $\vec{e}_3$ and $\vec{\tau}$) are based on the *N*th node. Similar as in the planar substrate case, the random force profile on the grooved substrate can be expressed in the *x* and τ directions as:

$$f_{Nx} = \left\|\vec{f}_N\right\|\sin\theta \text{ and } f_{N\tau} = \left\|\vec{f}_N\right\|\cos\theta \tag{5.49}$$

Further, $\vec{f}_N$ can be expressed as:

$$\vec{f}_N = f_{Nx}\vec{e}_1 + f_{N\tau}\vec{\tau} = f_{Nx}\vec{e}_1 + f_{Ny}\vec{e}_2 + f_{Nz}\vec{e}_3 \tag{5.50}$$

Then the virtual work due to $\vec{f}_N$ is written as:

$$\delta W_N = f_{Nx}\delta r_{xN} + f_{Ny}\delta r_{yN} + f_{Nz}\delta r_{zN} = f_{Nx}\delta r_{xN} + \left[f_{Ny} + f_{Nz}\left(\frac{dr_z}{dr_y}\right)_N \right]\delta r_{yN} \tag{5.51}$$

which is part of Eq. (5.36).

5.2.4 Axon tip outgrowth and crystallization

Different models have been developed to capture the tip outgrowth, considering the effects of the tubulin concentration at the tip [van Veen1994], the neurite length [van Veen1994], or the tension force in the axon [Heidemann1994]. The tip outgrowth rate has been assumed to be an inverse function of elastic tension [Graham2006], since the assembly rate decreases with elastic tension for a certain type of neurons microtubule. Some tip outgrowth models [Zheng1991, Heidemann1994, O'Toole2008] introduce the tip outgrowth rate as proportional to the external force at the tip. Since the relationship between the tip outgrowth rate and the external force depends on the type of neuron, different parameters characterizing the axon response to the external force, if needed, should be experimentally determined. The tip outgrowth model developed by Heidemann *et al*. [Heidemann1994] is applied here for its good physical description of the inelastic elongation. In this model, the tip outgrowth rate $\frac{dl_t}{dt}$ is expressed as follows:

$$\frac{dl_t}{dt} = k_t\left(\left\|\vec{f}_N\right\| - F_0\right) \tag{5.52}$$

where l_t is the elongation due to the tip outgrowth, k_t is the tip outgrowth rate coefficient, and F_0 is the minimal tension required to trigger tip outgrowth. As so, the tip outgrowth rate is proportional to the magnitude of the excess external force at the tip with respect to the threshold F_0. For PC12 neurites, it was found that k_t is about 5 to 50 m/(s·N) and $F_0 = 10^{-9}$ N [Zheng1991]. When the tip outgrowth is the predominant effect in axonal elongation, the ratio of the tip outgrowth rate to the external force, based on O'Toole *et al*.'s model, is about 3 m/(s·N) [O'Toole2008]. Herein, k_t is set on the order of 1 m/(s·N) accordingly, and $\left\|\vec{f}_N\right\|$ is assumed constant and on the order of 10^{-8} N

[Aeschlimann2000], thus $\frac{dl_t}{dt}$ is set as 10^{-8} m/s.

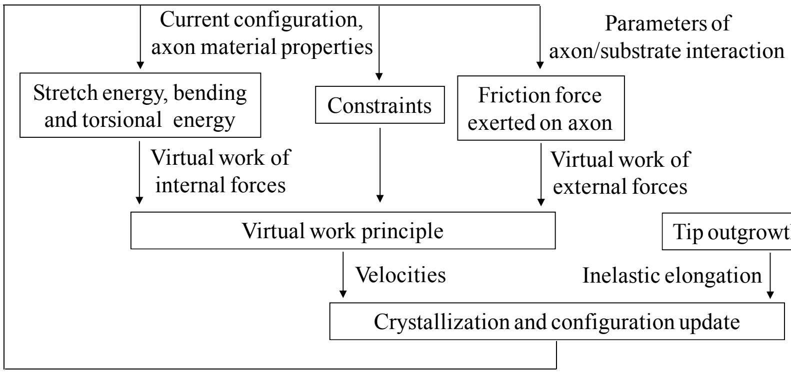

Fig. 5.5. Flowchart of axonal outgrowth modeling.

Since only the distal part of the axon moves during the outgrowth [Chang1998], the proximal part of the axon is artificially crystallized in this study as in [Aeschlimann2000], and for simplicity the crystallization rate $\frac{dl_{cr}}{dt}$ is set as $\frac{dl_{cr}}{dt} = \frac{dl_t}{dt}$, where l_{cr} is the crystallized length during the axon outgrowth process. The axonal outgrowth modeling procedure is described in Fig. 5.5.

5.3 Axonal outgrowth simulation and validation

5.3.1 Simulation parameters

In this simulation, the initial axonal length is set as 5 μm and divided into 50 segments, resulting in 0.1 μm long segments. To simulate the axonal outgrowth progress as depicted in Fig. 5.5, some parameters need to be determined either experimentally or theoretically. As treated as an elastic beam, the axon Young's modulus E depends on the type of neuron cell. By assuming the cross sectional area A of axon being of the order of 10^{-12} m^2, the Young's modulus E of typical neuritis such as the PC12 neurite is of the order of 10^5 Pa [Dennerll1988, Aeschlimann2000]. However, this is no available information regarding the axon shear modulus G. Since G can be estimated using $G = \frac{E}{2(1+\nu)}$, where ν is the Poisson's ratio. Herein G is assumed to have the same order of magnitude of E. The axon radius R is about 0.3 μm [Aeschlimann2000], thus $K_s = E\pi R^2$ is set as 3×10^{-8} N, $K_1 = K_2 = \frac{E\pi R^4}{4}$ as 6×10^{-22} N·m^2, and $K_3 = \frac{G\pi R^4}{2}$ as 10^{-21} N·m^2.

The first constant of friction μ_1 was estimated based on Dennerll *et al.*'s work [Dennerll1988] by Aeschlimann, and μ_1 for one neurite is chosen as 0.1 N·s/m [Aeschlimann2000]. Since the outgrowth process is simulated with the finite element method, the friction force is distributed on the nodes among the segments. As so, the first constant of friction in simulation η_1 is estimated as $\eta_1 \sim \frac{0.1}{N-1}$ N·s/m, where N-1 is 50 in this study, resulting in η_1 on the order of 10^{-3}~10^{-2} N·s/m, which is comparable to the measurement results by O'Toole *et al.* [O'Toole2008]. In this study, η_1 is arbitrarily chosen as 10^{-2} N·s/m. There is no available information about the second constant of friction η_2 thus far, and $\eta_2 = 10^{-12}$ N·s·m is assumed for each segment. Table 5.1 lists the parameters characterizing the axon and the axon/substrate interactions.

Table 5.1. Axon parameters in the simulations.

Symbol	Meaning	Estimated value	References
R	Radius	3×10^{-7} m	[Aeschlimann2000]
ρ	Density	10^3 kg/m^3	[Aeschlimann2000]
E	Young's modulus	10^5 N/m^2	[Dennerll1988]
G	Shear modulus	10^5 N/m^2	
$\lVert\vec{f}_N\rVert$	Magnitude of force exerted on the tip of axon	10^{-8} N	[Aeschlimann2000]
μ_1	First constant of friction	10^4 Pa·s	[O'Toole2008]
μ_2	Second constant of friction	10^{-5} N·s	
η_1	First constant of friction in simulation	10^{-3}~10^{-2} N·s/m	[Aeschlimann2000]
η_2	Second constant of friction simulation	10^{-12} N·s·m	
dl_t/dt	Inelastic elongation rate	10^{-8} m/s	[Aeschlimann2000]
dl_c/dt	Crystallization rate	10^{-8} m/s	[Aeschlimann2000]

5.3.2 Simulation results and validation

Grooves have been fabricated on the inner surface of polymeric hollow fiber membrane-based nerve conduits [Zhang2005]. Their shape, shown in Fig. 5.1, can be described as:

$$z = F(y) = H\left[1 - \cos\left(\frac{2\pi y}{W}\right)\right] \tag{5.53}$$

with two important characteristics: width W and height $2H$. Both parameters are varied in this study to appreciate the influence of geometry on the axonal outgrowth. According to previous studies [Rutkowski2004, Hsu2007], the groove width is chosen on the order of

100 μm, while the groove height is on the order of 10 μm.

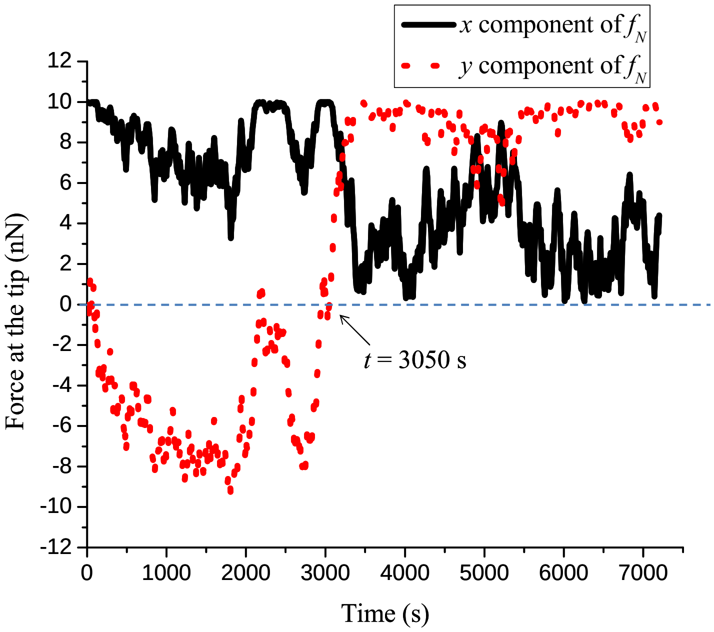

Fig. 5.6. Randomly generated $\vec{f}_N$ profile.

The effect of the groove geometry (W and H) on axonal outgrowth under a given external force $\vec{f}_N = (f_{Nx}, f_{Ny}, 0)$ as shown in Fig. 5.6, during a two-hour period, is illustrated in Fig. 5.7. The axonal outgrowth is a process which has both deterministic and stochastic factors [Maskery2005], so the external force is randomly generated. It can be seen when W increases from 50 μm to 200 μm that the average axonal length along the x direction decreases. There is a 20% decrease of the average directional outgrowth between the grooved one with a 50 μm width and a 20 μm height and a planar substrate ($H = 0$). A similar trend can be observed when the groove height H increases. For a 100 μm width substrate, the average outgrowth length in the x direction increases from 70.9 to 90.4 μm when $2H$ increases from 0 to 60 μm. Under the width and height range investigated, a narrow and deep groove may better promote directional outgrowth as predicted. It is concluded that the axonal alignment can be improved by increasing the ratio $\frac{H}{W}$ of the substrate geometry and a carefully designed substrate texture improves directional outgrowth.

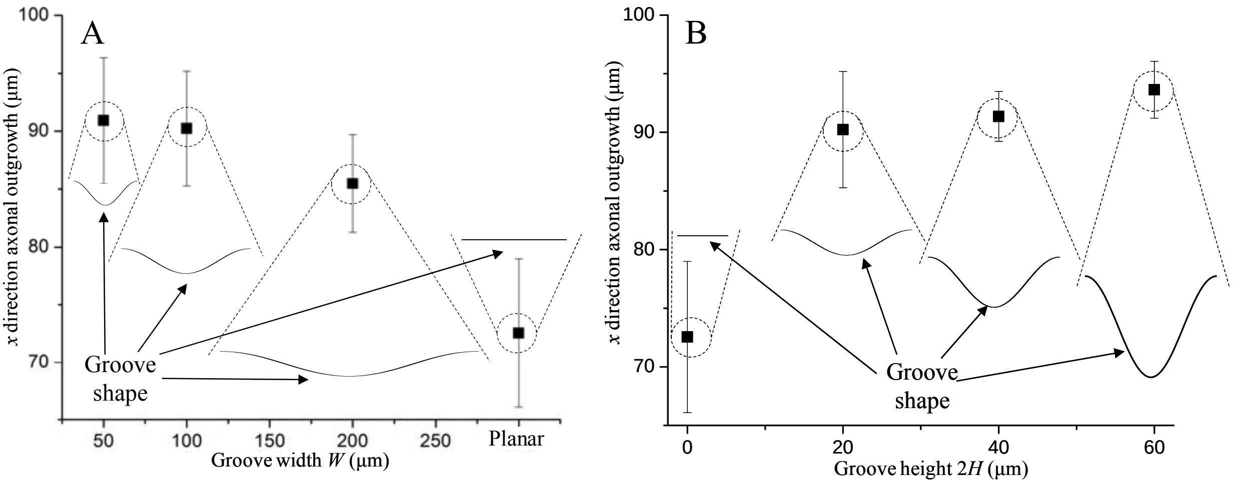

Fig. 5.7. Effect of groove geometry on the mean value of outgrowing axons under a given external force: (A) width effect when $H = 10$ μm and (B) height effect when $W = 100$ μm.

The simulation results also have been compared with the experimental observations in the outgrowth of dorsal root ganglion (DRG). In DRG regeneration, it was found that both the alignment and outgrowth rate of regenerating axons increased significantly on grooved nerve conduits compared with those on smooth nerve conduits [Zhang2005]. As shown in Fig. 5.8, the simulated outgrowth rate (0.94×10^{-8} m/s,) is very comparable to that of the experimental study (0.93×10^{-8} m/s). For the grooved nerve conduits (50 μm width and 40 μm height), the simulated outgrowth rate is lower than the measured one: 1.3×10^{-8} m/s versus 1.6×10^{-8} m/s, and still satisfactorily captures the outgrowth process. The good agreements in Fig. 5.8 show that the proposed modeling approach is capable of capturing the axonal outgrowth process on some grooved substrates.

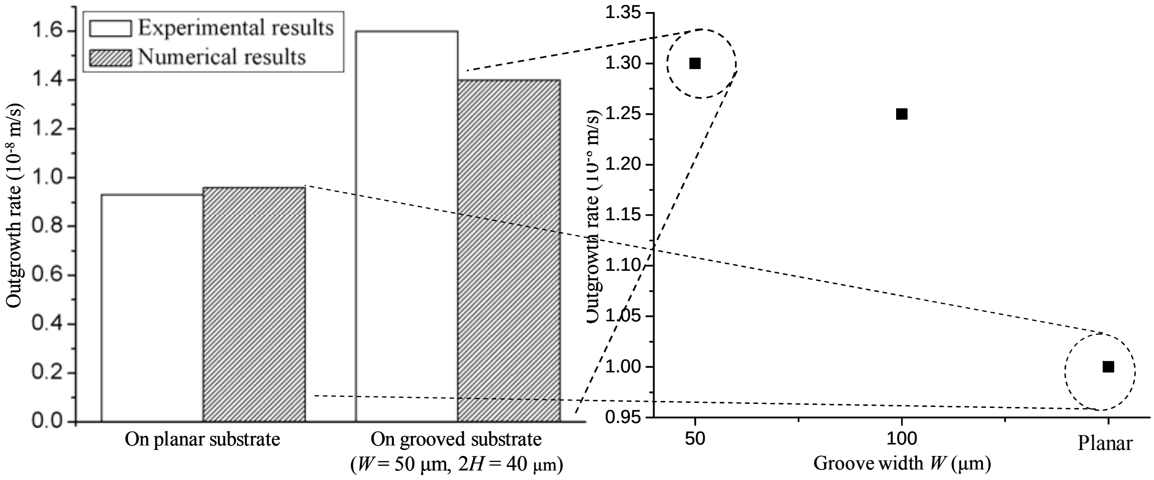

Fig. 5.8. Comparison of experimental [Zhang2005] and numerical results of axonal/neurite outgrowth over different substrates.

5.4 Discussion

In this study, the textured substrate surface is represented by the sinusoidal groove, which is of the order of 100 μm in width and 10 μm in height. This groove size is larger than the diameter of axon (1 μm), justifying the 1D beam model treatment for the axon. The axon geometry is such that the diameter is much smaller than the groove size, but the length has the same order of magnitude as the groove width. As seen in this study, even if the diameter of the axon is very small compared with the groove size, the effect of the substrate geometry cannot be ignored. However, in some previous experimental studies, where the groove width varied from 100 nm [Johansson2006] to 350 μm [Li2005] and the groove height varied from 300 nm [Johansson2006] to 150 μm [Houchin-Ray2007], the associated influence of the groove geometry was not clearly understood. Some contradictory observations regarding the substrate effect have been reported. For example, the axon of mouse sensory ganglia can well sense a tiny grooved pattern (200 nm) and grow parallel to the groove [Johansson2006], while neonatal rat DRGs may bridge their neurites perpendicularly to a 100 μm groove [Goldner2006] by ignoring the guidance effect of grooves. Certainly, the effect of the substrate geometry on the outgrowth performance depends on the neuronal cell type, the neurite/substrate interactions, and even the substrate compliance [Li2005]. A more general model should be further studied to describe the effect of contact-induced guidance with the help of systematic experimental investigations and biophysical understanding of the axon outgrowth mechanism.

The model is based on the assumption that the axonal outgrowth is a quasi-static process (Assumption b), thus at each time t the governing equations are the equilibrium equations. In order to validate the assumption, a simple problem involving only the stretching of a beam is considered. The classical equation of the beam motion for the 1D displacement D in the x-direction reads:

$$\rho A \frac{\partial^2 D}{\partial t^2} = EA \frac{\partial^2 D}{\partial x^2} - \mu_1 \frac{\partial D}{\partial t} \tag{5.54}$$

There are three terms in Eq. (5.54), the inertia term $\rho A \frac{\partial^2 D}{\partial t^2}$, the elastic term $EA \frac{\partial^2 D}{\partial x^2}$, and the friction term $\mu_1 \frac{\partial D}{\partial t}$. For a characteristic time T and a characteristic length L, the orders of magnitude to be compared are respectively:

$$\frac{\rho A}{T^2},\ \frac{EA}{L^2},\ \text{and}\ \frac{\mu_1}{T} \tag{5.55}$$

or can be rewritten as:

$$\frac{\rho L^2}{ET^2},\ 1,\ \text{and}\ \frac{\mu_1 L^2}{EAT} \tag{5.56}$$

Based on the values of the parameters defined in Table 5.1 and L chosen of the order of 10 μm, it can be deduced from Eq. (5.56) that the three terms are now:

$$\frac{10^{-12}}{T^2},\ 1,\ \text{and}\ \frac{10}{T} \tag{5.57}$$

The time scale associated to the evolutions of the external force $\vec{f}_N$ is 10 s. So for a characteristic time T = 10 s, the first ratio in Eq. (5.57) is far smaller than 1, and the contribution of inertia term can be neglected with respect to the elastic term. Additionally, the velocity of axon is about 10^{-8} m/s, and the elastic term and the friction term thus have the same order of magnitude.

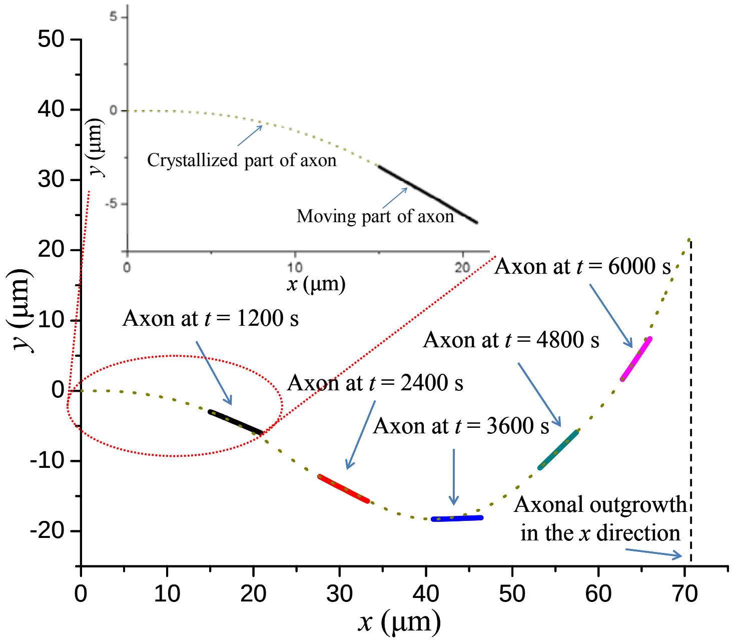

Fig. 5.9. Axonal configurations at different times when outgrowing on the planar surface.

A representative axonal outgrowth progression on a planar substrate is illustrated in Fig. 5.9. This is simulated under an external force $\vec{f}_N = \left(f_{Nx}, f_{Ny}, 0\right)$ (Fig. 5.6) during a two-hour period. Since f_{Nx} and the axonal initial configuration are both along the x direction, the positive f_{Nx} ensures that the axon is always pulled forward by the external force and does not move backward. At the same time, f_{Ny} varies between -10^{-8} to 10^{-8} N, the axon may turn right and then left upon the f_{Ny} direction. This is consistent with the experimental observations, showing that the intrinsic stiffness of the neurite inhibits the perpendicular migration of the axon [Forciniti2009]. In this example, the total axonal length is 99.2 μm after 2 hours outgrowth, while the axonal outgrowth in the *x* direction is only 70.9 μm, leading to an axonal outgrowth efficiency as $\frac{\text{Axonal length in } x \text{ the direction}}{\text{Total axonal length}} = \frac{70.9}{99.2} = 71.6\%$, which is much lower than those of grooved substrates, for example, 98.9% on a 50 μm width and 40 μm height groove.

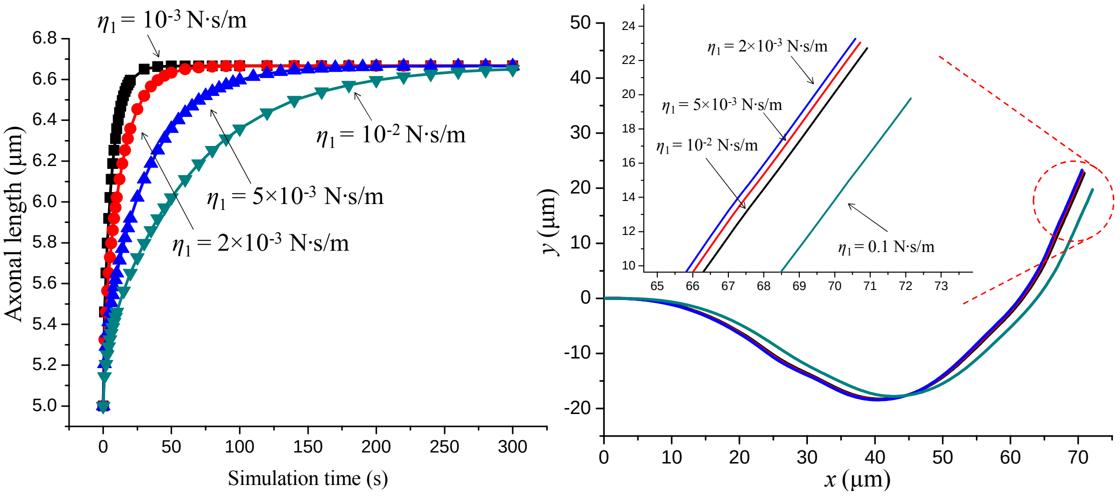

(A) (B)

Fig. 5.10. Effect of the first constant of friction η_1 on axonal elongation. (A) Stretch outgrowth; (B) stretch outgrowth and tip outgrowth.

The interaction between axon and substrate is characterized by the constants of friction η_1 and η_2, which need to be carefully discussed. In [Aeschlimann2000], for the PC12 neurite, a value of η_1 was estimated between 10^{-3}~10^{-2} N·s/m. Due to the adhesion and surface roughness, the constants of friction for the axon on the polymeric-based nerve conduit may be even larger. Thus, the effect of the first constant of friction is discussed and shown in Fig. 5.10. The purely elastic axonal elongation (without tip outgrowth) with different first constants of friction η_1 can be seen in Fig. 5.10A, for an initial axon configuration along the x direction with a 5 μm length, and subject to the constant external force $\vec{f}_N = 10^{-8}\vec{e}_1$ N. When the first constant of friction η_1 increases, the axon reaches the same steady state more slowly. However, as shown in Fig. 5.10B, for a 10^{-8} m/s tip outgrowth with the force profile obtained in Fig. 5.6, the effect of the friction is not obvious, meaning the tip outgrowth is the predominant mechanism of axonal outgrowth. While Fig. 5.11 shows the second constant of friction η_2 associated to moment with the contribution as the force $\vec{f}_N$ specified in Fig. 5.6. It is found that when η_2 increases, the axonal length decreases but the outgrowth in the x-direction increases, which means that the axonal outgrowth efficiency is improved by a higher η_2. A higher η_2 may keep the initial outgrowth direction, and prevent the axon from extending perpendicularly, leading to a better alignment.

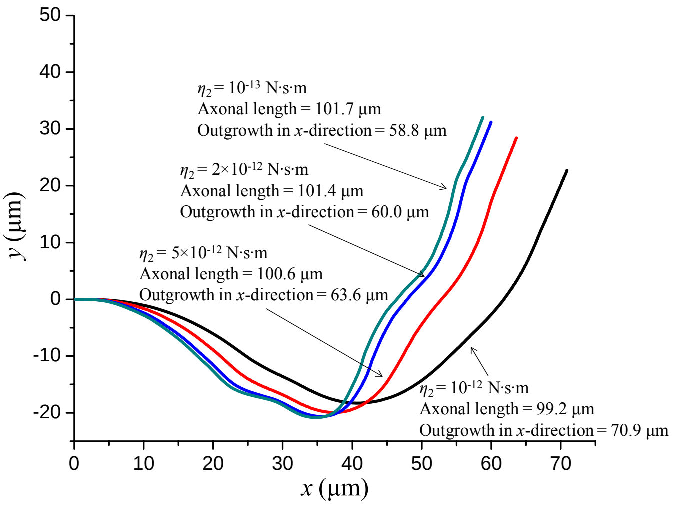

Fig. 5.11. Effect of the second constant of friction η_2 on axonal elongation.

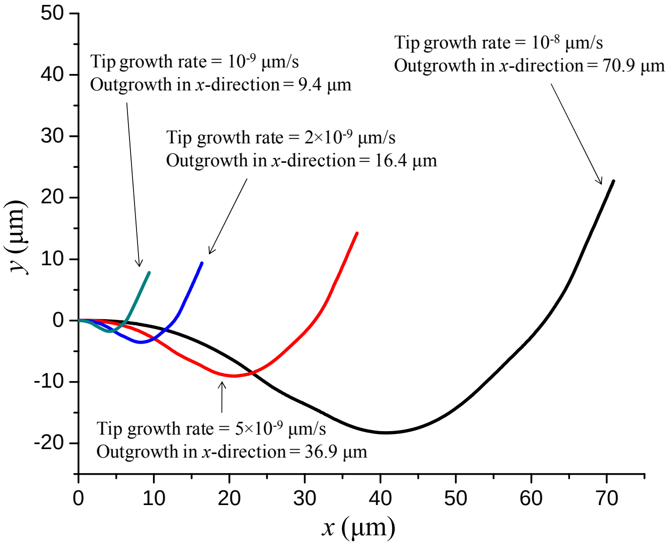

Fig. 5.12. Effect of the tip outgrowth rate on axonal elongation.

Under the same external force profile in Fig. 5.6, the axon configurations look very similar; however, the axonal length in the *x*-direction increases significantly with the tip outgrowth rate. As seen from Fig. 5.12, the predominant factor influencing the axonal elongation is the tip outgrowth. This indicates that the chemical and/or biological guidance cues may significantly promote the outgrowth rate while the axon alignment depends mainly on the elastic and the friction contributions, the axonal material properties and the topological guidance cue.

In the current model, the grooves are applied as the substrate surface, and their cross sections are represented with a sine curve with a 100 μm width and a 10 μm height. This groove size is much larger than the diameter of axon 1 μm, justifying the 1D beam model for the axon. The axon geometry is such that the diameter is much smaller than the groove size, but the length has the same order of magnitude as the groove width. Even if the diameter of the axon is very small compared to the groove size, the effect of the geometry of the substrate cannot be neglected. However, in previous experimental studies, where the groove width varied from 100 nm [Johansson2006] to 350 μm [Li2005], and groove height varied from 300 nm [Johansson2006] to 150 μm [Houchin-Ray2007], the influence of the groove size was not clearly determined. For example, the axon of mouse sensory ganglia can sense a tiny grooved pattern (200 nm) and grow parallel to the groove [Johansson2006], while neonatal rat DRGs can bridge their neurites perpendicularly to a 100 μm groove [Goldner2006], which means the guidance effect of substrates with large width or large height can be ignored. The contradictory effects are not only due to the neurite. The effect of the substrate geometry is associated with the neuronal cell type, the neurite/substrate interactions, and even the substrate compliance [Li2005]. Therefore, the model in this work takes into account the geometry of the substrate, one type of friction, and a rigid substrate. A general model to describe the effect of a contact-induced guidance is needed, requiring more experimental data and better description of the physical mechanisms involved.

5.5 Summary

In this chapter, a numerical model is presented to study the axonal outgrowth in a textured nerve conduit. This is the first numerical model, where the effect of the substrate geometry and the interaction between axon and textured substrate are taken into account. Based on this model, it was found that the substrate geometry will affect the axonal outgrowth length and its alignment. When groove width decreases from 200 to 50 μm or groove height increases from 0 to 60 μm, the axonal elongation in the longitudinal direction of groove may increase. Directional outgrowth can thus be significantly improved with a narrow and deep grooved texture. For a given groove texture, the axonal length was found mainly determined by the tip outgrowth while the axon alignment will be mainly affected by the axon elastic properties and the friction due to the substrate. The simulation results were in good agreement with previous experimental observations.

CHAPTER SIX

CONCLUSIONS

In this chapter, the different tasks carried out and the different results obtained in this work are summarized. The contributions to the fabrication of textured nerve conduits and their application to nerve regeneration are listed. Further researches related to this study are presented at the end.

6.1 Conclusions

The goal of this study is to fabricate textured HFMs with aligned grooves on the inner surface and to understand the effect of the grooved texture on nerve regeneration and repair. This study includes an experimental part investigating the grooved HFM fabrication, a theoretical part explaining the groove formation, and a numerical part studying the axonal outgrowth on the grooved substrate. The conclusions can be summarized as follows:

1. The PAN/DMSO/water HFMs were fabricated using immersion-precipitation induced phase inversion methods. A spinneret with smooth and annular die was used for the dry-jet wet spinning process. Besides HFMs with smooth inner surface, HFMs with deformed inner surface also can be obtained. In order to be applied as an efficient nerve conduit, the HFM with grooved inner texture was designed and controlled. It

was found that the HFM geometry, morphology and strength are sensitive to the experimental operating conditions, such as polymer solution flow rate and concentration, nonsolvent flow rate, and air gap distance. So the effect of these fabrication conditions was carefully studied. It is observed that under a defined polymer concentration, at different air gap distances, the regular aligned grooves on the inner surface of HFMs can be obtained for a certain combination of polymer solution and nonsolvent flow rates, which is called the groove forming region for HFM fabrication. Then, fabricated HFMs were also carefully characterized in terms of geometry of the cross section, morphology, and strength. The influence of different fabrication conditions on the HFM characteristics was carefully investigated in order to obtain the designed HFMs for further application as nerve conduits. As the most concern in this work, the number of groove in the HFM inner surface was found to increase with the air gap distance, and decrease with the polymer solution concentration and flow rate. But it was found that the number of groove is not sensitive to the inner nonsolvent flow rate.

2. The process-induced instability was presented as the groove formation mechanism, and two possible mechanisms were studied: an hydrodynamic instability and a buckling. The hydrodynamic instability happens before polymer solution solidification, so it is the onset of instability during the HFM fabrication, while the buckling is the

magnifying solidification step for the development of instability, leading to the final geometry of HFMs. Theoretical models were developed for both hydrodynamic instability and buckling. It was found that the hydrodynamic instability does not have enough time to develop for PAN/DMSO/water HFMs, so the predominant factor for the groove formation in PAN/DMSO/water HFMs is buckling. While, by studying the solutal Marangoni effect in PU/DMSO/water HFMs using the hydrodynamic instability model, the predicted groove number tendency of PU/DMSO/water HFMs in terms of the initial polymer solution concentration was in good agreement with the available experimental results. Then, the buckling due to the shrinkage of HFM outer surface during solidification, for example in case of PAN/DMSO/water HFMs, was studied. A multilayer buckling model was developed to explain the groove formation. In this model, the morphology of HFMs was divided into several sublayers. The shrinkage of the outer surface during the polymer solidification leads to a radially inward pressure, and then the inner skin layer of HFMs buckles to form the aligned grooved texture due to the inward pressure. A reasonable prediction of the tendency of groove number variation under different fabrication conditions was observed for PAN/DMSO/water HFMs.

3. The axonal outgrowth on a textured substrate was numerically modeled. The influence of the substrate geometry was studied, introducing the effect of the substrate geometry

and the interaction between axon and textured substrate. The axon was modeled as a viscoelastic beam, and its motion and deformation were described as it remains in contact with a 3D substrate, which is the inner surface of grooved nerve conduits. In this work, the stretching, bending and rotation of the axon were considered. The interaction between axon and substrate is due to friction. Both elastic elongation and tip outgrowth mechanisms were included in this model. Based on this model, it was found that the substrate geometry will affect the axonal outgrowth length and its alignment. When groove width decreases from 200 to 50 μm or groove height increases from 0 to 60 μm, the axonal elongation in the longitudinal direction of groove increases. Directional outgrowth can thus be significantly improved with a narrow and deep grooved texture. It is also found that for a given grooved substrate, the axonal length was found mainly determined by the tip outgrowth while the axon alignment will be mainly affected by the axon elastic properties and the friction due to the substrate. The simulation results were in good agreement with previous experimental observations.

6.2 Research contributions

The results in this work, which can contribute to the future research on nerve conduit fabrication and nerve regeneration, are listed as follows:

1. By investigating effects of four operating conditions: polymer concentration, polymer solution flow rate, nonsolvent flow rate, and air gap distance, a groove forming region is for the first time experimentally defined for a certain polymer concentration, where stable and regular grooved HFMs can be obtained. Another interesting observation is that by fixing polymer concentration, polymer solution flow rate, and nonsolvent flow rate, the groove number increases with air gap distance within 1 to 20 cm, which is different from previous studies [Bonyadi2007, Shi2007]. These different effects of air gap distance on groove number in grooved HFM fabrication may be defined not only on material properties, but also on the fabrication setup, for example spinneret and pumps.
2. In previous studies, it is generally recognized that grooves are introduced by process-induced instability, and it is proposed that both hydrodynamic instability and buckling play roles. But, there is not any rigorous mathematical model can be used to predict the groove formation process. In this work, it is the first time to mathematically model the groove formation process, where both hydrodynamic instability and buckling are studied. In the study of the hydrodynamic instability, the solutal Marangoni effect due to polymer adsorption at the interface is introduced as the driving mechanism, which has never been studied in the field of HFM fabrication. A dimensionless model is developed for the Marangoni effect-induced hydrodynamic

instability, where the dispersion relation results from a scale analysis associated to a linear stability analysis. Thus this model can be applied for different material combinations. The buckling of HFMs induced by the shrinkage during solidification is studied with a multilayer model. Since the morphology of HFM is significantly influenced by fabrication conditions and the number of sublayer in the HFM morphology varies, this multilayer buckling model can be adapted to take into account different layered morphologies.

3. In this study, the model of axonal outgrowth on the grooved substrate is the first numerical model, which can consider the effect of substrate geometry. Assumed as a quasi-static outgrowth process, the axon configuration is updated by solving the governing equations at any time *t*. By introducing the Cosserat theory, the axon is modeled as a 1D beam with 3D motion and 3D deformation, allowing stretching, bending, and torsion of the axon. In most of other simulations, only the stretching and bending are described for the axon deformation on a planar substrate. But in this model, the rotation of the axon cross section is also taken into account. This study shows that by carefully choosing the size (width and height), the groove on the inner surface of nerve conduits can be a promising topographical guidance cue to improve the axonal outgrowth.

6.3 Future work

This work covers experimental, theoretical, and numerical studies on the fabrication of a polymeric nerve conduit with topographical guidance cues on its inner surface, and explains the formation of grooved inner surface and the role of this grooved texture on the axonal outgrowth. However, more related researches need to be carried out, such as:

1. HFMs with grooved inner texture are fabricated with a smooth and annular die by controlling the fabrication conditions. By applying the theory of instability, the groove number and geometry can be controlled in a certain range by adjusting the operating conditions. However, due to the nature of process-induced instability, it is difficult to accurately determine the groove number and geometry using just a smooth and annular die. So in order to control the groove size more precisely, one reliable method is to modify the inner tube in the spinneret from a cylindrical shape to a designed shape, imposing the grooved shape to HFMs. Some researchers have designed smart spinnerets with a grooved die (Fig. 6.1) to fabricate grooved HFMs for gas separation [Nijdam2005, Culfaz2010]. Therefore, a grooved inner tube also can be used in our spinneret to fabricate grooved HFMs. So in this approach, the grooved texture in HFM inner surface is no longer formed due to buckling, which has to be eliminated. Although, with a grooved die, the groove number of fabricated HFMs is determined, it

was found that the inner/outer diameters of HFMs and the groove size are reduced during the fabrication [Nijdam2005]. Therefore, the control of HFM geometry and the effect of fabrication conditions on the final geometry when a grooved die is used, need to be addressed.

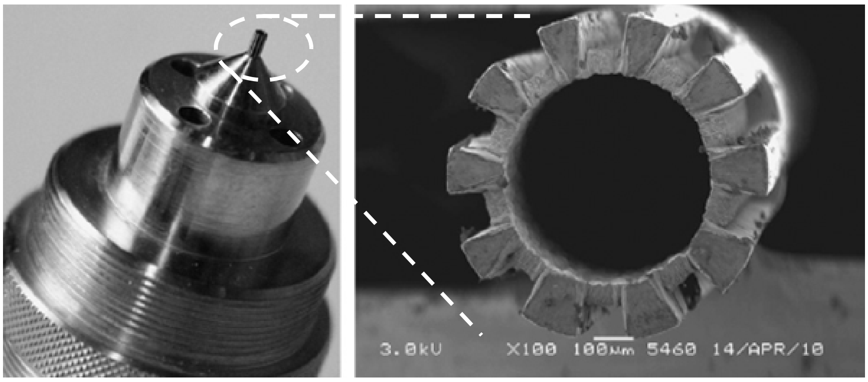

Fig. 6.1. The spinneret with grooved die [Culfaz2010].

2. Two instability mechanisms are studied in this work, where the hydrodynamic instability is the onset of instability, and the buckling can lead to the final grooved geometry. But in some cases, the interfacial gradient of polymer solution/nonsolvent interface during the mass transfer is such that a solutal Marangoni instability can develop within a very short time period. Once the hydrodynamic instability has enough time to develop, and can lead to an obvious non-uniform HFM cross section before the solidification of polymer solution, the hydrodynamic instability will be the

predominant instability mechanism during the fabrication process, such as PU/DMSO/water fluids. In this case, nascent fibers with a deformed inner surface are formed before entering the coagulation bath, so the hydrodynamic and the elastic problems are coupled. Therefore, it is very necessary to develop a model, which can be applied to different combinations of fluids.

3. In the simulation of axonal outgrowth on the grooved substrate with groove width of order of 100 μm, the ratio of the axon diameter to the groove width is about 0.01, thus the axon can be modeled as a 1D beam, and it is assumed that the axon remains in the same groove during outgrowth. But in the current research of nerve regeneration on patterned substrates, the groove width of substrate can be as small as 1 μm, even 100 nm [Gomez2007]. On other studies, substrates with certain surface roughness (about 1 μm) are also used as nerve conduit. In these cases, the axon diameter is of the order of the groove width or the surface roughness, so a general 3D model has to be developed for the axon. Furthermore, in this study the interaction between axon and substrate is considered as a friction, but other interactions may exist depending on the neuron type and the material properties of the substrate, such as the formability of biological bonds. Meanwhile, the substrate stiffness is also found to have significant influence on the axon morphology and reaction [Balgude2001]. Therefore, a more comprehensive model needs to be developed to describe the axonal outgrowth. Moreover, due to the

time scale of the force evolution exerted at the tip $\vec{f}_N$ is on the order of 1 ~ 10 s, the model introduces an elastic stretching and an inelastic tip outgrowth. In order to compare to a 24 hours axonal outgrowth, a viscoelastic constitutive law needs to be chosen for the axon, and a totally viscoelastic model has to be developed for the axon, the limit case, for 7 days, being the totally viscous model as developed by O'Toole *et al*. [O'Toole2008].

APPENDICES

Appendix A

Three-layer buckling model for PU/DMSO/Water HFMs

The driving mechanism of the buckling of HMFs may vary based on the material property and fabrication setup. Because of different operating conditions and morphologies between PAN and PU HFMs, an alternative buckling model is developed in this appendix. It is a model which can explain the groove formation on the inner surface of PU/DMSO/water HFMs.

A.1 Three-layer buckling model

As shown in Fig. A.1, the fabrication of PU/DMSO/water HFMs by phase inversion method leads to the formation of three distinct layers, two dense inner and outer skin layers and one porous intermediate layer [Long2008]. When the polymer dope solution comes out of the spinneret as seen in Fig. 1.9, it first interacts with the inner nonsolvent bore fluid, resulting in the mass transport and phase separation-induced elastic inner skin layer. The outer skin layer is not well formed until the nascent fiber enters the external nonsolvent-based coagulation bath after traveling through an air gap. Once the nascent fiber enters the coagulation bath, the phase separation and solidification processes occur at the fiber outer surface while the inner surface might have already well developed into a thin-walled elastic cylindrical layer. The HFM intermediate layer usually is the last part to completely solidify and may shrink lastly due to mass transfer through both the inner and outer surfaces. As a similar effect due to pre-strain, the shrinkage results in a circumferential stress on the inner and outer elastic layers. This stress may be mainly relieved through the buckling of the inner layer, which solidifies first, instead of the outer layer. This solidification-induced deformation scenario is similar to the buckling of a stiff thin elastic film on a compliant soft elastic plane substrate [Huang2005], which has been intensively studied recently [Groenewold2001, Song2008]. As so, the groove formation of HFM is modeled here as the intermediate layer shrinkage-induced buckling of the inner layer. The inner layer buckles with a particular wave length to minimize the total elastic energy of the system.

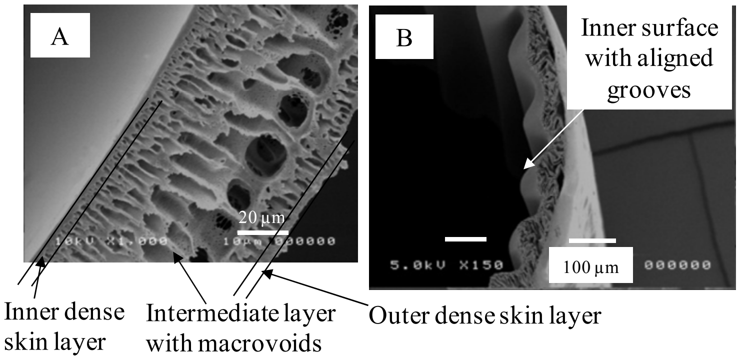

Fig. A.1. PU/DMSO/water HFM with A) smooth, or B) axially grooved inner surface.

PU HFMs here are modeled as a thin-walled elastic cylindrical shell with three distinct but seamless connected layers as in Fig. A.2. For each layer E_i is the Young's modulus, h_i is the thickness, and v_i is the Poisson's ratio, where $i = 1$ stands for the inner layer, $i = 2$ the intermediate layer, and $i = 3$ the outer layer. Both the inner and outer layers bond to the intermediate layer seamlessly as a whole fiber during fabrication. To study this shrinkage-induced buckling phenomenon, the following assumptions are introduced:

a) Due to the porous microstructure of the intermediate layer and the dense-skin structure of the inner layer, the inner layer is much stiffer than the intermediate layer, i.e. $E_1 >> E_2$. As shown in Fig. A.1, the thickness of the inner layer is usually much smaller than that of the intermediate layer, i.e. $h_1 << h_2$, so the intermediate layer is modeled as a semi-infinite solid substrate;

b) As the inner layer is a circular thin layer, the tangential strain of the inner layer $\varepsilon_{\theta\theta}$ is considered uniform;

c) As $E_3 >> E_2$, the thin outer layer is considered as a rigid boundary for the thick intermediate layer;

d) Due to the thin-walled cylindrical shell geometry of HFM, this buckling process is modeled as plane-strain [Kardomateas2005]; and

e) The HFM total energy consists of: the membrane energy (U_{m}), which is the strain energy due to stretching of the inner layer; the bending energy (U_{b}), which is the strain energy due to bending of the inner layer; and the substrate energy (U_s), which is the strain energy of the intermediate layer.

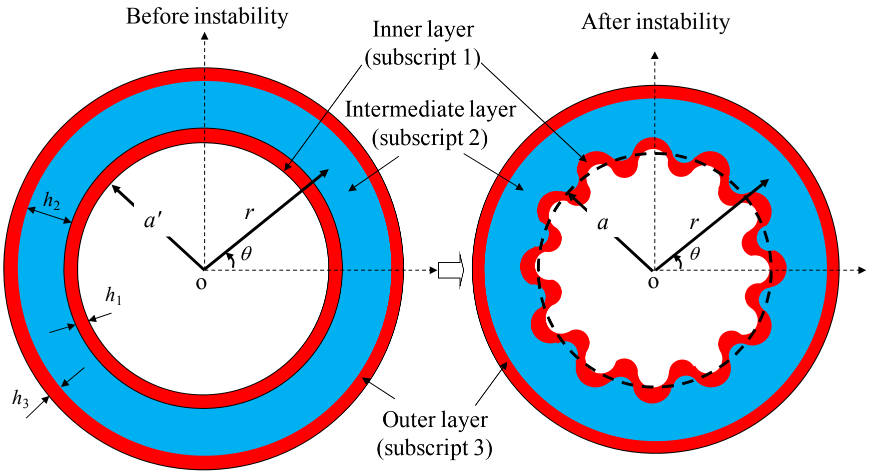

Fig. A.2. Schematic of the three-layer model before and after instability (three layers are denoted using the subscripts 1, 2, and 3).

A.2 Strain energy of HFM

The inner layer strain energy has two parts: the membrane and bending energies. Assuming the radius of inner layer is a' before shrinkage, the radius after shrinkage a is $\frac{a'}{(1+\varepsilon)}$, where ε is the solidification-induced equivalent pre-strain applied to the intermediate layer. As shown in Fig. 4.8, the radial displacement $u_r^{(1)}$ is defined as:

$$u_r^{(1)} = a + A\cos(k\theta) - a' \tag{A.1}$$

where A is the groove amplitude, $k = \frac{2\pi a}{\lambda}$ is the groove number (wave number), and λ is the wave length. The nonlinear membrane strain of the inner layer is defined as [Bogdanovich1993]:

$$\varepsilon_{\theta\theta} = \frac{\partial u_\theta^{(1)}}{a'\partial\theta} + \frac{u_r^{(1)}}{a'} + \frac{1}{2}\left(\frac{\partial u_r^{(1)}}{a'\partial\theta}\right)^2 \tag{A.2}$$

where $u_r^{(1)}$ and $u_\theta^{(1)}$ are the displacements in the r and θ directions. Per the $\varepsilon_{\theta\theta}$ uniformity assumption, $u_\theta^{(1)}$ can be further determined based on Eqs. (A.1) and (A.2):

$$u_\theta^{(1)} = -\frac{A}{k}\sin(k\theta) + \frac{A^2 k}{8a'}\sin(2k\theta) \tag{A.3}$$

By substituting Eqs. (A.1) and (A.3) into Eq. (A.2), it is found:

$$\varepsilon_{\theta\theta} = \frac{A^2k^2}{4a^2(1+\varepsilon)^2} - \frac{\varepsilon}{1+\varepsilon} \tag{A.4}$$

Based on Eq. (A.4), the membrane energy [Timoshenko1961] can be estimated as follows:

$$U_m = \frac{\overline{E}_1 h_1 a'}{2}\int_0^{2\pi} \varepsilon_{\theta\theta}^{\ 2} d\theta = \frac{\overline{E}_1 h_1 \pi\left[k^4A^4 - 8a^2k^2\left(\varepsilon+\varepsilon^2\right)A^2 + 16a^4\left(\varepsilon^4 + 2\varepsilon^3 + \varepsilon^2\right)\right]}{16a^3(1+\varepsilon)^3} \tag{A.5}$$

where $\overline{E}_1 = \frac{E_1}{1-\nu_1^{\ 2}}$. The tangential curvature change χ_θ [Bogdanovich1993] of any two points of the inner layer is:

$$\chi_\theta = -\frac{1}{a'^2}\frac{\partial^2 u_r^{(1)}}{\partial\theta^2} = \frac{Ak^2\cos(k\theta)}{a^2(1+\varepsilon)^2} \tag{A.6}$$

Based on Eq. (A.6), the bending energy [Timoshenko1961] can be further estimated as follows:

$$U_b = \frac{\overline{E}_1 h_1^3 a'}{24}\int_0^{2\pi} \chi_\theta^2 d\theta = \frac{\overline{E}_1 h_1^3 \pi}{24}\frac{A^2 k^4}{(1+\varepsilon)^3 a^3} \tag{A.7}$$

The intermediate layer here is assumed as a semi-infinite solid substrate after solidification, and this assumption can be verified based on the finite thickness solution as follows. For the intermediate layer, the boundary conditions at the inner/intermediate interface are the displacement continuity and zero shear stress as follows:

$$u_r^{(2)}\Big|_{r=a} = A\cos(k\theta),\ \ \sigma_{r\theta}\Big|_{r=a} = 0 \tag{A.8}$$

There is no displacement at the intermediate/outer interface during the process, so the boundary condition can be written as follows:

$$u_r^{(2)}\Big|_{r=H} = 0,\ \ u_\theta^{(2)}\Big|_{r=H} = 0 \tag{A.9}$$

where H is the radius of intermediate/outer interface. The Airy stress function given by the Michell solution [Barber2005] is expressed as:

$$\phi = \left(B_1 r^{k+2} + A_1 r^{-k+2} + B_2 r^k + A_2 r^{-k}\right)\cos(k\theta) \tag{A.10}$$

Both displacements and stresses can be obtained from the Michell solution, and the coefficients A_1, A_2, B_1, and B_2 can be determined based on the boundary conditions Eqs. (A.8) and (A.9). It should be noticed that in the HFM geometry, $\frac{a}{H} \sim \frac{1}{2}$, and k is large, which was around 50 in this study, so $\left(\frac{a}{H}\right)^k << 1$. Due to small $\left(\frac{a}{H}\right)^k$, the coefficients A_1, A_2, B_1, and B_2 can be expressed as follows:

$$A_1 = \frac{2A\mu_2(k+1)}{k(1+\kappa_2)+\kappa_2-1}a^{k-1},\ \ A_2 = -\frac{2A\mu_2(k-1)}{k(1+\kappa_2)+\kappa_2-1}a^{k+1},\ \ B_1 << 1, \text{and}\ \ B_2 << 1 \quad \text{(A.11)}$$

where $\mu_2 = \frac{E_2}{2(1+\nu_2)}$, and $\kappa_2 = 3-4\nu_2$ for this plane-strain case. Therefore the Airy stress function to be considered is the Airy stress function of a semi-infinite substrate, which confirms the assumption of semi-infinite intermediate layer.

As so, associated with A_1 and A_2 (Eq. A.11), the Cauchy stress tensor components can be deduced [Barber2005] as follows:

$$\sigma_{rr} = -C\left[k+2-k\left(\frac{a}{r}\right)^2\right]\cos(k\theta) \quad \text{(A.12)}$$

$$\sigma_{r\theta} = C\left[1-\left(\frac{a}{r}\right)^2\right]\sin(k\theta) \quad \text{(A.13)}$$

$$\sigma_{\theta\theta} = C\left[k-2-k\left(\frac{a}{r}\right)^2\right]\cos(k\theta) \quad \text{(A.14)}$$

where $C = \frac{2A\mu a^{k-1}(k^2-1)}{r^k[k(1+\kappa_2)+\kappa_2-1]}$, and the displacement field ($u_r^{(2)}, u_\theta^{(2)}$) is

$$u_r^{(2)} = D\left[(k+1)(\kappa_2+k-1)-(k-1)k\left(\frac{a}{r}\right)^2\right]\cos(k\theta) \quad \text{(A.15)}$$

$$u_\theta^{(2)} = D\left[-(k+1)(\kappa_2-k+1)-(k-1)k\left(\frac{a}{r}\right)^2\right]\sin(k\theta) \quad \text{(A.16)}$$

where $D = \frac{2Aa^{k-1}}{r^{k-1}[k(1+\kappa_2)+\kappa_2-1]}$. The strain energy of the intermediate layer U_s can be expressed as:

$$U_s = \int_0^{2\pi}\int_a^{\infty} \frac{1}{2}\bar{\bar{\sigma}} : \bar{\bar{\varepsilon}}\, r dr d\theta \tag{A.17}$$

where $\bar{\bar{\sigma}}$ and $\bar{\bar{\varepsilon}}$ are the stress and strain tensors of the intermediate layer, respectively. Using Gauss' theorem with the specified boundary conditions, this intermediate layer strain energy can be expressed as follows:

$$U_s = \frac{1}{2}\int_S \vec{n} \cdot \bar{\bar{\sigma}} \cdot \vec{u}^{(2)} dS = -\frac{1}{2}\int_0^{2\pi} \sigma_{rr}\big|_{r=a} u_r^{(2)}\big|_{r=a} a d\theta = \frac{\pi E_2 A^2 \left(k^2 - 1\right)}{2\left[2k\left(1-\nu_2\right)+1-2\nu_2\right]\left(1+\nu_2\right)} \tag{A.18}$$

where $\vec{n}$ is the normal vector, $\vec{u}^{(2)}$ is the displacement vector, and S is the inner surface of the intermediate layer.

The total energy is based on the inner and intermediate layers while the outer layer is considered as a rigid boundary for the whole system, then the total energy can be represented as a function of the groove number *k* and the amplitude *A* as follows:

$$U_{total}(k, A) = U_m(k, A) + U_b(k, A) + U_s(k, A) \tag{A.19}$$

By substituting Eqs. (A.5), (A.7), and (A.18) into Eq. (A.19), the total energy is rewritten in the following form:

$$U_{total}(k, A) = \frac{\bar{E}_1 h_1 \pi}{16a^3(1+\varepsilon)^3}\left(k^4 A^4 + f A^2\right) + \frac{\bar{E}_1 h_1 \pi a \varepsilon^2}{1+\varepsilon} \tag{A.20}$$

where

$$f = -8a^2\varepsilon(1+\varepsilon)k^2 + \frac{2}{3}h_1^2 k^4 + \frac{8E_2\left(k^2-1\right)a^3(1+\varepsilon)^3}{\left[2k\left(1-\nu_2\right)+1-2\nu_2\right]\left(1+\nu_2\right)\bar{E}_1 h_1} \tag{A.21}$$

The total energy (Eq. A.20) is a fourth order polynomial of *A*. The groove number *k* and the amplitude A are to be determined by minimizing the total energy:

$$\frac{\partial U_{total}(k,A)}{\partial A}=0\,,\ \frac{\partial U_{total}(k,A)}{\partial k}=0 \tag{A.22}$$

or

$$f+2A^2k^4=0\,,\ \frac{f}{k}-\frac{1}{2}\frac{\partial f}{\partial k}=0 \tag{A.23}$$

When $f > 0$, the minimum of total energy can be only obtained at $A = 0$, that is, there is no groove on inner layer. When $f < 0$, the minimum of total energy can be obtained at a positive amplitude:

$$A=\sqrt{-\frac{f}{2k^4}} \tag{A.24}$$

Once the amplitude A is determined, the groove number k can be obtained accordingly by solving Eq. (A.23).

A.3 Shrinkage induced buckling in PU/DMSO/water HFMs

In this study, it is considered that the HFM intermediate layer is the last part to completely solidify and may shrink lastly due to mass transfer through both the inner and outer surfaces. The typical phase separation-induced polymeric membrane shrinkage has been determined experimentally around 2% [Wu2006, Menut2008]. The intermediate layer solidification-induced equivalent pre-strain ε is also taken as 2% in this PU/DMSO/water-based fabrication study. It should be pointed out that this equivalent pre-strain has to be experimentally determined for better modeling accuracy.

For the model validation purpose, the Young's modulus of fabricated HFMs [Long2008] was measured using an Electroforce 3200 tension test machine (Electroforce 3200, Bose, MN, USA) with a crosshead speed of 10 mm/min and a clamp distance 10 mm. The average Young's modulus E_{ave} was found around 10^7 Pa, which is of the same order of typical HFMs [Cabasso1976, Tsai2001]. Since it is difficult to determine the Young's modulus for each layer, it is assumed in this study that the porous intermediate layer has a lower Young's modulus comparing with the dense inner and outer skin layers. For simplicity, the inner and outer layers are considered to have a same Young's modulus ($E_1 = E_3$), and a Young's modulus ratio is further introduced: $\eta = E_1/E_2 = E_1/E_3$. The experimentally measured average E_{ave} is a function of η and the thickness of layers:

$$E_{ave} = \frac{E_1\left[(a'+h_1)^2 - a'^2\right] + E_2\left[(a'+h_1+h_2)^2 - (a'+h_1)^2\right] + E_3\left[(a'+h)^2 - (a'+h_1+h_2)^2\right]}{(a'+h)^2 - a'^2} \qquad \text{(A.25)}$$

where $h = h_1 + h_2 + h_3$. E_1 (E_3) and E_2 can be determined using Eq. (A.25) given E_{ave} and η. The Poisson's ratio of both inner and intermediate layers was taken as $v_1 = v_2 = 0.3$ based on the measurement of typical HFMs [Cabasso1976]. Based on the experiment observations, the thickness of the inner and outer layers (h_1 and h_3) is assumed as βh, and the thickness of the intermediate layer (h_2) as $(1\text{-}2\beta)h$, where β is taken as 0.05 based on the experimental observations.

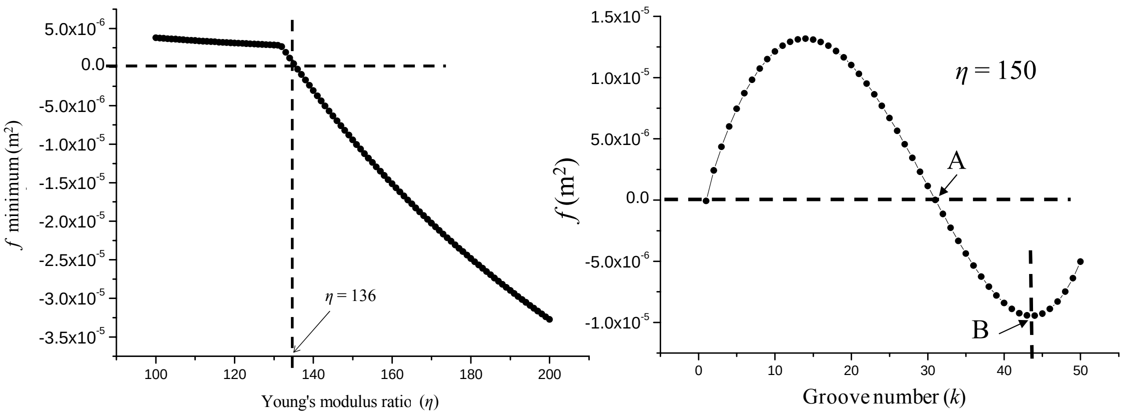

(A) (B)

Fig. A.3. (A) Effect of the Young's modulus ratio η on the f minimum value ($2 < k < 60$) and (B) effect of the groove number on f ($\eta = 150$ and $\beta = 0.05$).

For any given HFM geometry, both f which is dependent on η as shown in Eq. (A.21) and $\frac{\partial f}{\partial k}$ should be negative for grooves to form as specified by Eq. (A.23). Fig. A.3 shows the relationship between f and η. The case considered in the figure corresponds to the following conditions: 12.5 w/w% polymer solution concentration, 4 ml/min inner nonsolvent flow rate, and 1.2 ml/min polymer solution flow rate (Table A.1). It can be seen that f is only negative within a certain η range under given process conditions. While η is to be experimentally determined in the future, it is taken as 150 in this study to illustrate the proposed modeling approach. As $E_1 >> E_2$, the ratio η is of the order 10^2, so 150 is considered to be a reasonable approximation. From Fig. A.3B, it is found that only the groove range AB satisfies both the groove forming requirements: $f < 0$ and $\frac{\partial f}{\partial k} < 0$, which means that grooves can only form under certain operating conditions for a given material system. The exact groove number and amplitude can be determined by solving Eq. (A.23). Under certain fabrication conditions, the HFM material properties and geometry lead to a positive f when k is positive, thus no groove can form under these fabrication conditions. Therefore, this buckling model not only can predict the groove number and the amplitude, but also can explain qualitatively why under certain conditions no groove can form.

Fig. A.4 further illustrates the measured and predicted groove numbers for $\eta = 150$ under different flow rates and polymer concentration ratios as specified in Table A.1. A reasonable prediction accuracy of groove number has been observed for the experimental cases studied. Therefore, based on the buckling-induced instability mechanism, the HFM groove number is modeled by studying the buckling of a thin elastic film on a soft compliant substrate under the effect of shrinkage.

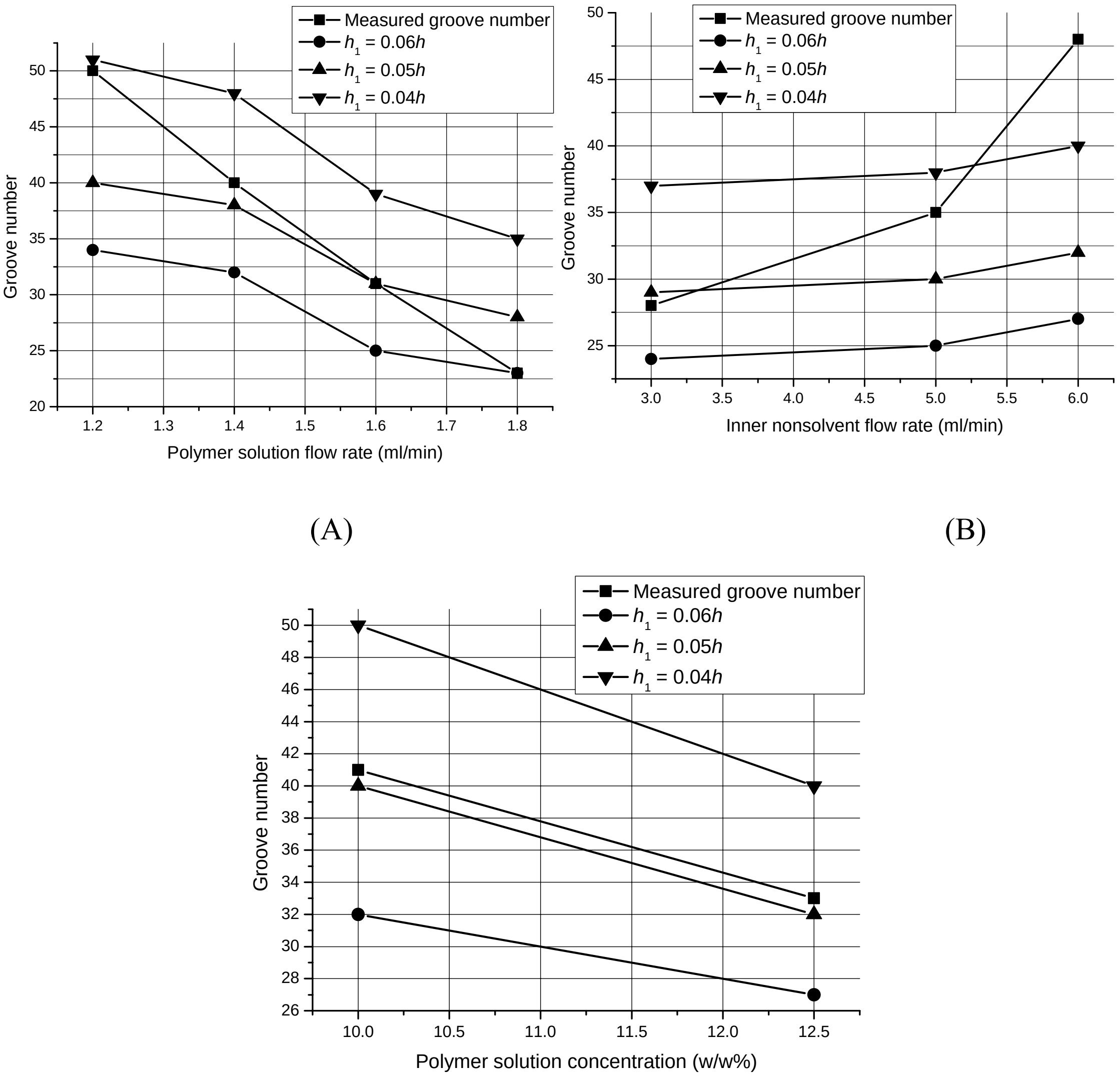

(A) (B)

(C)

Fig. A.4. Groove number comparison between the measurements and predictions (η = 150 and β = 0.05) per each fabrication condition: (A) polymer solution flow rate, (B) inner nonsolvent flow rate, and (C) polymer concentration.

Table A.1. PU/DMSO/water HFM fabrication conditions and experimental observations.

Fabrication conditions (under a 10 mm air-gap)		Inner diameter (mm)	Outer diameter (mm)	Average groove number
Effect of polymer solution flow rate • 12.5 w/w% polymer solution concentration • 4 ml/min inner nonsolvent flow rate	Polymer solution flow rate (ml/min)			
	0.8	1.54	1.72	No groove
	1.0	1.44	1.65	No groove
	1.2	1.41	1.60	50
	1.4	1.33	1.52	40
	1.6	1.25	1.47	31
	1.8	1.19	1.42	23
	2.0	1.12	1.38	No groove
Effect of inner nonsolvent flow rate • 12.5 w/w% polymer solution concentration • 1.6 ml/min polymer solution flow rate	Inner nonsolvent flow rate (ml/min)			
	2.0	1.10	1.36	No groove
	3.0	1.20	1.42	28
	4.0	1.33	1.52	34
	5.0	1.34	1.58	35
	6.0	1.42	1.66	48
	7.0	1.49	1.71	No groove
Effect of polymer solution concentration • 1.6 ml/min polymer solution flow rate • 4 ml/min inner nonsolvent flow rate	Polymer solution concentration			
	10 w/w%	1.38	1.57	41
	12.5 w/w%	1.30	1.52	33
	15 w/w%	1.23	1.46	No groove

A.4 Summary

The buckling instability is studied for PU/DMSO/water HFM fabrication. The buckling takes place during the polymer solution solidification, which will lead to the final grooved cross section of HFM. The PU/DMSO/water HFM is described by a three-layer model, and the buckling is introduced by solidification-induced shrinkage of the intermediate layer. A reasonable modeling accuracy of groove number is observed compared to experimental results of PU/DMSO/water HFM fabrication. Therefore, the model developed here gives a reasonable explanation of the groove formation in HFM fabrication for certain fluids.

Appendix B

Equations and derivations for axonal outgrowth model

In this section, the expressions of u_i and ω_i given by Eqs. (5.17) and (5.18) are derived. The expression of the rotation rate of an axon cross section defined by Eq. (5.4) as

$$\dot{\vec{d}}_p = \vec{\omega} \times \vec{d}_p \quad (i = 1, 2, 3) \tag{B.1}$$

For illustration, when $p = 3$,

$$\dot{\vec{d}}_3 = \vec{\omega} \times \vec{d}_3 = \left(\sum_{i=1}^{3} \omega_i \vec{d}_i \right) \times \vec{d}_3 = -\omega_1 \vec{d}_2 + \omega_2 \vec{d}_1 \tag{B.2}$$

Thus, it is deduced that

$$\dot{\vec{d}}_3 = \frac{\partial \vec{d}_3}{\partial t} = \frac{\partial \vec{d}_3}{\partial \hat{q}} \frac{\partial \hat{q}}{\partial t} = \frac{\partial \vec{d}_3}{\partial \hat{q}} \dot{\hat{q}} = -\omega_1 \vec{d}_2 + \omega_2 \vec{d}_1 \tag{B.3}$$

The projection of Eq. (B.3) onto $\vec{d}_1$ and $\vec{d}_2$ yields

$$\omega_1 = -\left[\left(\frac{\partial \vec{d}_3}{\partial \hat{q}} \right)^T \vec{d}_2 \right] \cdot \dot{\hat{q}} \tag{B.4}$$

where

$$\frac{\partial \vec{d}_3}{\partial \hat{q}} = \begin{pmatrix} \frac{\partial d_{3x}}{\partial q_1} & \frac{\partial d_{3x}}{\partial q_2} & \frac{\partial d_{3x}}{\partial q_3} & \frac{\partial d_{3x}}{\partial q_4} \\ \frac{\partial d_{3y}}{\partial q_1} & \frac{\partial d_{3y}}{\partial q_2} & \frac{\partial d_{3y}}{\partial q_3} & \frac{\partial d_{3y}}{\partial q_4} \\ \frac{\partial d_{3z}}{\partial q_1} & \frac{\partial d_{3z}}{\partial q_2} & \frac{\partial d_{3z}}{\partial q_3} & \frac{\partial d_{3z}}{\partial q_4} \end{pmatrix} = 2 \begin{pmatrix} q_3 & q_4 & q_1 & q_2 \\ -q_4 & q_3 & q_2 & -q_1 \\ -q_1 & -q_2 & q_3 & q_4 \end{pmatrix} \tag{B.5}$$

Substituting Eqs. (5.16) and (B.5) into Eq. (B.4), it can be deduced that

$$\omega_1 = 2\|\hat{q}\|\left[q_4, q_3, -q_2, -q_1\right]\cdot\left[\dot{q}\right] = 2\left(\begin{bmatrix} 0 & 0 & 0 & 1 \\ 0 & 0 & 1 & 0 \\ 0 & -1 & 0 & 0 \\ -1 & 0 & 0 & 0 \end{bmatrix}\begin{bmatrix} q_1 \\ q_2 \\ q_3 \\ q_4 \end{bmatrix}\right)^T \cdot\left[\dot{q}\right] \tag{B.6}$$

Comparing two expressions of ω_1 given by Eqs. (5.18) and (B.6), as $\|\hat{q}\| = 1$, the matrix $[B_1]$ can be obtained $\left[B_1\right] = \begin{bmatrix} 0 & 0 & 0 & 1 \\ 0 & 0 & 1 & 0 \\ 0 & -1 & 0 & 0 \\ -1 & 0 & 0 & 0 \end{bmatrix}$, and similarly $\left[B_2\right] = \begin{bmatrix} 0 & 0 & -1 & 0 \\ 0 & 0 & 0 & 1 \\ 1 & 0 & 0 & 0 \\ 0 & -1 & 0 & 0 \end{bmatrix}$, $\left[B_3\right] = \begin{bmatrix} 0 & 1 & 0 & 0 \\ -1 & 0 & 0 & 0 \\ 0 & 0 & 0 & 1 \\ 0 & 0 & -1 & 0 \end{bmatrix}$.

The virtual work of internal forces of the *i*th segment is deduced from the expression of the stretching and bending energies of any segment *i* by Eqs. (5.30) and (5.31) as

$$U_{sj} = \frac{K_s l_j}{2}\left(\frac{1}{l_j}\left\|\vec{r}_{(j+1)} - \vec{r}_j\right\| - 1\right)^2, j = 1 \text{ to } N\text{-}1 \tag{B.7}$$

$$U_{bj} = \frac{l_j^q}{2}\sum_{p=1}^{3} K_p \left\{\left[\left[B_p\right]\left(\left[q_{(j+1)}\right] + \left[q_j\right]\right)\right]^T \cdot \frac{\left[q_{(j+1)}\right] - \left[q_j\right]}{l_j^q}\right\}^2, j = 1 \text{ to } N\text{-}1 \tag{B.8}$$

Thus, the partial derivatives in Eq. (5.32) are:

$$\frac{\partial U_{sj}}{\partial r_{xj}} = -K_s\left(\frac{1}{l_j}\left\|\vec{r}_{(j+1)} - \vec{r}_j\right\| - 1\right)\frac{\left(r_{x(j+1)} - r_{xj}\right)}{\left\|\vec{r}_{(j+1)} - \vec{r}_j\right\|} \tag{B.9}$$

$$\frac{\partial U_{sj}}{\partial r_{yj}} = -K_s\left(\frac{1}{l_j}\left\|\vec{r}_{(j+1)} - \vec{r}_j\right\| - 1\right)\frac{\left[r_{y(j+1)} - r_{yj} + \frac{dr_{zj}}{dr_{yj}}\left(r_{z(j+1)} - r_{zj}\right)\right]}{\left\|\vec{r}_{(j+1)} - \vec{r}_j\right\|} \tag{B.10}$$

$$\frac{\partial U_{bj}}{\partial q_{1j}} = \sum_{p=1}^{3}\frac{K_p}{l_j^q}\left\{\left[\left[B_p\right]\left(\left[q_{(j+1)}\right]+\left[q_j\right]\right)\right]^T \cdot \left(\left[q_{(j+1)}\right]-\left[q_j\right]\right)\right\}\left\{\left(\left[B_p\right]\begin{bmatrix}1\\0\\0\\0\end{bmatrix}\right)^T \cdot \left(\left[q_{(j+1)}\right]-\left[q_j\right]\right)+\left[\left[B_p\right]\left(\left[q_{(j+1)}\right]+\left[q_j\right]\right)\right]^T \cdot \begin{bmatrix}-1\\0\\0\\0\end{bmatrix}\right\} \tag{B.11}$$

The other partial derivatives with respect to q_{2i}, q_{3i}, and q_{4i} are obtained similarly.

The virtual work of internal forces in one segment can be obtained based on the generalized force (Eq. 5.35) exerted on the *i*th node ($i = 1$ to N) defined by:

$$f_{xi} = -\eta_1\dot{r}_{xi}\text{, and }\ f_{yi} = -\eta_1\left[1+\left(\frac{dr_{zi}}{dr_{yi}}\right)^2\right]\dot{r}_{yi} \tag{B.12}$$

Based on Eqs. (5.18) and (5.36), and $\delta\vec{\varphi}_j = \sum_{p=1}^{3}\left\{2\left(\left[B_p\right]\left[q_j\right]\right)^T \cdot \left[\delta q_j\right]\right\}\vec{d}_{pj}$, the generalized moment exerted on the middle cross section of *j*th segment ($j = 1$ to N-1) is

$$M_{1j} = -2\eta_2\left[\omega_{1j}q_{4j} - \omega_{2j}q_{3j} + \omega_{3j}q_{2j}\right] = -4\eta_2\left[q_{4j}\left(\left[B_1\right]\left[q_j\right]\right)^T - q_{3j}\left(\left[B_2\right]\left[q_j\right]\right)^T + q_{2j}\left(\left[B_3\right]\left[q_j\right]\right)^T\right]\cdot\left[\dot{q}_j\right]$$

$$M_{2j} = -2\eta_2\left[\omega_{1j}q_{3j} + \omega_{2j}q_{4j} - \omega_{3j}q_{1j}\right] = -4\eta_2\left[q_{3j}\left(\left[B_1\right]\left[q_j\right]\right)^T + q_{4j}\left(\left[B_2\right]\left[q_j\right]\right)^T - q_{1j}\left(\left[B_3\right]\left[q_j\right]\right)^T\right]\cdot\left[\dot{q}_j\right]$$

(B.13)

$$M_{3j} = -2\eta_2\left[-\omega_{1j}q_{2j} + \omega_{2j}q_{1j} + \omega_{3j}q_{4j}\right] = -4\eta_2\left[\left(-q_{2j}\right)\left(\left[B_1\right]\left[q_j\right]\right)^T + q_{1j}\left(\left[B_2\right]\left[q_j\right]\right)^T + q_{4j}\left(\left[B_3\right]\left[q_j\right]\right)^T\right]\cdot\left[\dot{q}_j\right]$$

$$M_{4j} = -2\eta_2\left[-\omega_{1j}q_{1j} - \omega_{2j}q_{2j} - \omega_{3j}q_{3j}\right] = -4\eta_2\left[-q_{1j}\left(\left[B_1\right]\left[q_j\right]\right)^T - q_{2j}\left(\left[B_2\right]\left[q_j\right]\right)^T - q_{3j}\left(\left[B_3\right]\left[q_j\right]\right)^T\right]\cdot\left[\dot{q}_j\right]$$

Based on Eqs. (5.38)-(5.40), the different partial derivatives needed to express the virtual work principle as in Eq. (5.42) are given by

$$\frac{\partial C_{1j}}{\partial r_{xj}} = \frac{-1}{\left\| \vec{r}_{(j+1)} - \vec{r}_j \right\|} + \frac{\left(r_{x(j+1)} - r_{xj} \right)^2}{\left\| \vec{r}_{(j+1)} - \vec{r}_j \right\|^3} \tag{B.14}$$

$$\frac{\partial C_{1j}}{\partial r_{yj}} = \frac{\left(r_{x(j+1)} - r_{xj} \right) \left[r_{y(j+1)} - r_{yj} + \left(\frac{dr_{zj}}{dr_{yj}} \right) \left(r_{z(j+1)} - r_{zj} \right) \right]}{\left\| \vec{r}_{(j+1)} - \vec{r}_j \right\|^3} \tag{B.15}$$

$$\frac{\partial C_{1j}}{\partial q_{1j}} = -2q_{3j}, \quad \frac{\partial C_{1j}}{\partial q_{2j}} = -2q_{4j}, \quad \frac{\partial C_{1j}}{\partial q_{3j}} = -2q_{1j}, \quad \frac{\partial C_{1j}}{\partial q_{4j}} = -2q_{2j} \tag{B.16}$$

$$\frac{\partial C_{1j}}{\partial r_{x(j+1)}} = \frac{1}{\left\| \vec{r}_{(j+1)} - \vec{r}_j \right\|} - \frac{\left(r_{x(j+1)} - r_{xj} \right)^2}{\left\| \vec{r}_{(j+1)} - \vec{r}_j \right\|^3} \tag{B.17}$$

$$\frac{\partial C_{1j}}{\partial r_{y(j+1)}} = -\frac{\left(r_{x(j+1)} - r_{xj} \right) \left[r_{y(j+1)} - r_{yj} + \left(\frac{dr_{z(j+1)}}{dr_{y(j+1)}} \right) \left(r_{z(j+1)} - r_{zj} \right) \right]}{\left\| \vec{r}_{(j+1)} - \vec{r}_j \right\|^3} \tag{B.18}$$

$$\frac{\partial C_{2j}}{\partial r_{xj}} = \frac{\left(r_{x(j+1)} - r_{xj} \right) \left(r_{y(j+1)} - r_{yj} \right)}{\left\| \vec{r}_{(j+1)} - \vec{r}_j \right\|^3} \tag{B.19}$$

$$\frac{\partial C_{2j}}{\partial r_{yj}} = \frac{-1}{\left\| \vec{r}_{(j+1)} - \vec{r}_j \right\|} + \frac{\left(r_{y(j+1)} - r_{yj} \right) \left[r_{y(j+1)} - r_{yj} + \left(\frac{dr_{zj}}{dr_{yj}} \right) \left(r_{z(j+1)} - r_{zj} \right) \right]}{\left\| \vec{r}_{(j+1)} - \vec{r}_j \right\|^3} \tag{B.20}$$

$$\frac{\partial C_{2j}}{\partial q_{1j}} = 2q_{4j}, \quad \frac{\partial C_{2j}}{\partial q_{2j}} = -2q_{3j}, \quad \frac{\partial C_{2j}}{\partial q_{3j}} = -2q_{2j}, \quad \frac{\partial C_{2j}}{\partial q_{4j}} = 2q_{1j} \tag{B.21}$$

$$\frac{\partial C_{2j}}{\partial r_{x(j+1)}} = -\frac{\left(r_{x(j+1)} - r_{xj} \right) \left(r_{y(j+1)} - r_{yj} \right)}{\left\| \vec{r}_{(j+1)} - \vec{r}_j \right\|^3} \tag{B.22}$$

$$\frac{\partial C_{2j}}{\partial r_{y(j+1)}} = \frac{1}{\left\| \vec{r}_{(j+1)} - \vec{r}_j \right\|} - \frac{\left(r_{y(j+1)} - r_{yj} \right) \left[r_{y(j+1)} - r_{yj} + \left(\frac{dr_{z(j+1)}}{dr_{y(j+1)}} \right) \left(r_{z(j+1)} - r_{zj} \right) \right]}{\left\| \vec{r}_{(j+1)} - \vec{r}_j \right\|^3} \tag{B.23}$$

$$\frac{\partial C_{3j}}{\partial r_{xj}} = \frac{\left(r_{x(j+1)} - r_{xj}\right)\left(r_{z(j+1)} - r_{zj}\right)}{\left\|\vec{r}_{(j+1)} - \vec{r}_j\right\|^3} \tag{B.24}$$

$$\frac{\partial C_{3j}}{\partial r_{yj}} = \frac{-\dfrac{dr_{zj}}{dr_{yj}}}{\left\|\vec{r}_{(j+1)} - \vec{r}_j\right\|} + \frac{\left(r_{z(j+1)} - r_{zj}\right)\left[r_{y(j+1)} - r_{yj} + \left(\dfrac{dr_{zj}}{dr_{yj}}\right)\left(r_{z(j+1)} - r_{zj}\right)\right]}{\left\|\vec{r}_{(j+1)} - \vec{r}_j\right\|^3} \tag{B.25}$$

$$\frac{\partial C_{3j}}{\partial q_{1j}} = 2q_{1j}, \quad \frac{\partial C_{3j}}{\partial q_{2j}} = 2q_{2j}, \quad \frac{\partial C_{3j}}{\partial q_{3j}} = -2q_{3j}, \quad \frac{\partial C_{3j}}{\partial q_{4j}} = -2q_{4j} \tag{B.26}$$

$$\frac{\partial C_{3j}}{\partial r_{x(j+1)}} = -\frac{\left(r_{x(j+1)} - r_{xj}\right)\left(r_{z(j+1)} - r_{zj}\right)}{\left\|\vec{r}_{(j+1)} - \vec{r}_j\right\|^3} \tag{B.27}$$

$$\frac{\partial C_{3j}}{\partial r_{y(j+1)}} = \frac{\dfrac{dr_{z(j+1)}}{dr_{y(j+1)}}}{\left\|\vec{r}_{(j+1)} - \vec{r}_j\right\|} - \frac{\left(r_{z(j+1)} - r_{zj}\right)\left[r_{y(j+1)} - r_{yj} + \left(\dfrac{dr_{z(j+1)}}{dr_{y(j+1)}}\right)\left(r_{z(j+1)} - r_{zj}\right)\right]}{\left\|\vec{r}_{(j+1)} - \vec{r}_j\right\|^3} \tag{B.28}$$

REFERENCES

[Aeschlimann2000] Aeschlimann M., 2000, "Biophysical Models of Axonal Pathfinding," Ph.D. thesis, University of Lausanne, Switzerland.

[Ananthakrishnan2007] Ananthakrishnan, R., and Ehrlicher, A., 2007, "The Forces Behind Cell Movement," International Journal of Biological Sciences, Vol. 3, pp. 303-317.

[Antman1995] Antman, S. S., 1995, Nonlinear Problems of Elasticity, Springer, Verlag.

[Arnold1996] Arnold, M., Boccaccini, A. R., and Ondracek, G., 1996, "Prediction of the Poisson's Ratio of Porous Materials", Journal of Materials Science, Vol. 31, pp. 1643-1646.

[Balgude2001] Balgude, A. P., Yu, X., Szymanski, A., and Bellamkonda, R. V., 2001, "Agarose Gel Stiffness Determines Rate of DRG Neurite Extension in 3D Cultures," Biomaterials, Vol. 22, pp. 1077-1084.

[Barber2005] Barber, J. R., 2003, *Elasticity*, Kluwer Academic Publishers, New York.

[Bogdanovich1993] Bogdanovich, A., 1993, *Non-linear Dynamic Problems for Composite Cylindrical Shells*, Elsevier, London.

[Bonyadi2007] Bonyadi, S., Chung, T. S., and Krantz, W. B., 2007, “Investigation of Corrugation Phenomenon in the Inner Contour of Hollow Fibers during the Non-solvent induced Phase-Separation Process,” Journal Membrane Science, Vol. 299, pp. 200-210.

[Bregman1998] Bregman, B. S., 1998, “Regeneration in the Spinal Cord,” Current Opinion in Neurobiology, Vol. 8, pp. 800-807.

[Brushart1995] Brushart, T. M., Mathur, V., Sood, R., Koschorke, G. M., 1995, “Dispersion of Regenerating Axons across Enclosed Neural Gaps,” The Journal of Hand Surgery, Vol. 20, pp. 557-564.

[Cabasso1976] Cabasso, I., Klein, E., and Smith, J. K., 1976, “Polysulfone Hollow Fibers. I. Spinning and Properties,” Journal of Applied Polymer Science, Vol. 20, pp. 2377-2394.

[Chan2008] Chan, C. E., and Odde, D. J., 2008, “Traction Dynamics of Filopodia on Compliant Substrates,” Science, Vol. 322, pp. 1687-1691.

[Chang1998] Chang, S., Rodionov, V. I., Borisy, G. G., and Popov, S. V., 1998, “Transport and Turnover of Microtubules in Frog Neurons Depend on the Pattern of Axonal Growth,” Journal of Neuroscience, Vol. 18, pp. 821-829.

[Chang2007] Chang, J., Shepherd, D. X., and Zhang, J. J., 2007, “Cosserat-Beam-Based Dynamic Response Modelling,” Computer Animation and Virtual Worlds, Vol. 18, pp. 429-436.

[Cheng2003] Cheng, H., Abo, M., and Okubo, A., 2003, “Development of Dimethyl Sulfoxide Biosensor Using A Mediatorimmobilized Enzyme Electrode,” Analyst, Vol. 128, pp. 724-727.

[Chung1997] Chung, T., and Hu, X., 1997, “Effect of Air-Gap Distance on the Morphology and Thermal Properties of Polyethersulfone Hollow Fibers,” Journal of Applied Polymer Science, Vol. 66, pp. 1067-1077.

[Cohen Addad1999] Cohen Addad, J. P., and Panine, P, 1999, “Pore Generation in Asymmetric Polymeric Membranes Correlation with Solvent Mobilities: Correlation with Solvent Mobilities,” Polymer Bulletin, Vol. 42, pp. 345-352.

[Culfaz2010] Culfaz, P. Z., Rolevink, E., van Rijn, C., Lammertink, R. G. H., and Wessling, M., 2010, “Microstructured Hollow Fibers for Ultrafiltration,” Journal of Membrane Science, Vol. 347, pp. 32-41.

[Davies1963] Davies, T. V., and Rideal, E. K., 1963 In *Interfacial phenomena*; Academic Press.

[de Ruiter2009] de Ruiter, G. C. W., Malessy, M. J. A., Yaszemski, M. J., Windebank, A. J., and Spinner, R. J., 2009, “Designing Ideal Conduits for Peripheral Nerve Repair,” Neurosurg Focus, Vol. 26, pp. E5.

[Dennerll1988] Dennerll, T. J., Joshi, H. C., Steel, V. L., Buxbaum, R. E., and Heidemann, S. R., 1988, “Tension and Compression in the Cytoskeleton of PC-12 Neurites. II: Quantitative Measurements.” Journal of Cell Biology, Vol. 107, pp. 665-674.

[Dennerll1989] Dennerll, T. J., Lamoureux, P., Buxbaum, R. E., and Heidemann, S. R., 1989, “The Cytomechanics of Axonal Elongation and Retraction,” Journal of Cell Biology, Vol. 109, pp. 3073-3083.

[Dent2003] Dent, E. W., and Gertler, F. B., 2003, “Cytoskeletal Dynamics and Transport in Growth Cone Motility and Axon Guidance,” Neuron, Vol. 40, pp. 209-227.

[Filler2004] Filler, A. G., 2004, *Do You Really Need Back Surgery: A Surgeon's Guide to Neck and Back Pain and How to Choose Your Treatment*, Oxford University Press, USA.

[Fleer1993] Fleer, G. J., Cohen-Stuart, M. A., Scheutjens, J. M. H. M., Cosgrove, T., and Vincent, B., 1993, *Polymer at interfaces*, Chapman & Hall.

[Forciniti2009] Forciniti L., Schmidt C. E., and Zaman M. H., 2009, “Computational Model Provides Insight into the Distinct Responses of Neurons to Chemical and Topographical Cues,” Annals of Biomedical Engineering, Vol. 37, pp. 363-374.

[Franze2010] Franze, K., and Guck, J., 2010, “The Biophysics of Neuronal Growth,” Report of Progress in Physics, Vol. 73, pp. 094601-1-19.

[Goldner2006] Goldner, J. S., Bruder, J. M., Li, G., Gazzola, D., and Hoffman-Kim, D., 2006, “Neurite Bridging Across Micropatterned Grooves,” Biomaterials, Vol. 27, pp. 460-472.

[Graham2006] Graham, B. P., and van Ooyen, A., 2006, “Mathematical Modelling and Numerical Simulation of the Morphological Development of Neurons,” BMC Neuroscience, Vol. 7, pp. S9.

[Groenewold2001] Groenewold, J., 2001, “Wrinkling of Plates Coupled with Soft Elastic Media,” Physica A, Vol. 298, pp. 32-45.

[Heidemann1994] Heidemann, S. R., and Buxbaum, R. E., 1994, “Mechanical Tension as A Regulator of Axonal Development,” Neurotoxicology, Vol. 15, pp. 95-107.

[Hennenberg1977] Hennenberg, M., Sørensen, T. S., and Sanfeld, A., 1977, “Deformational Instability of a Plane Interface with Transfer of Matter,” Journal of the Chemical Society-Faraday Transactions II, Vol. 73, pp. 48-66.

[Hoffman-Kim2010] Hoffman-Kim, D., Mitchel, J. A., and Bellamkonda, R. V., 2010, “Topography, Cell Response, and Nerve Regeneration,” Annual Review of Biomedical Engineering, Vol. 12, pp. 203-231.

[Houchin-Ray2007] Houchin-Ray, T., Swift, L. A., Jang, J., and Shea, L. D., 2007, “Patterned PLG Substrates for Localized DNA Delivery and Directed Neurite Extension,” Biomaterials, Vol. 28, pp. 2603-2611.

[Hsu2007] Hsu, S., Lu, P. S., Ni, H., and Su, C., 2007, “Fabrication and Evaluation of Microgrooved Polymers as Peripheral Nerve Conduits,” Biomedical Microdevices, Vol. 9, pp. 665-674.

[Huang2005] Huang, R., 2005, “Kinetic Wrinkling of An Elastic Film on A Viscoelastic Substrate,” Journal of the Mechanics and Physics of Solids, Vol. 53, pp. 63-89.

[Johansson2006] Johansson, F., Carlberg, P., Danielsen, N., Montelius, L., and Kanje, M., 2006, “Axonal Outgrowth on Nano-Imprinted Patterns,” Biomaterials, Vol. 27, pp. 1251-1258.

[Kardomateas2005] Kardomateas, G. A., and Simitses, G. J., 2005, “Buckling of Long Sandwich Cylindrical Shells under External Pressure,” ASME Journal of Applied Mechanics, Vol. 72, pp. 493-499.

[Kofron2010] Kofron, C. M., Liu, Y., Lopez-Fagundo, C. Y., Mitchel, J. A., and Hoffan-Kim, D., 2010, "Neurite Outgrowth at the Biomimetic Interface," Annals of Biomedical Engineering, Vol. 38, pp. 2210-2225.

[Lamoureux2010] Lamoureux, P. L., O'Toole, M. R., Heidemann, S. R., and Miller, K. E., 2010, "Slowing of Axonal Regeneration Is Correlated with Increased Axonal Viscosity during Aging," BMC Neuroscience, Vol. 11, pp. 140.

[Li2005] Li, N., and Folch, A., 2005, "Integration of Topographical and Biochemical Cues by Axons during Growth on Microfabricated 3-D Substrates," Experimental Cell Research, Vol. 311, pp. 307-316.

[Long2008] Long, Y., Zhang, N., Huang, Y., and Wen, X., 2008, "Formation of Highly Aligned Grooves on Inner Surface of Semipermeable Hollow Fiber Membrane for Directional Axonal Outgrowth," ASME Journal of Manufacturing Science and Engineering, Vol. 130, pp. 021011-1-8.

[Lowery2009] Lowery, L. A., and Vactor, D. V., 2009, "The Trip of the Tip: Understanding the Growth Cone Machinery," Nature Reviews Molecular Cell Biology, Vol. 10, pp. 332-343.

[Lu1999] Lu, J., and Waite, P., 1999, "Advances in Spinal Cord Regeneration," Spine, Vol. 24, pp. 926-930.

[Machado1999] Machado, P. S. T., Habert, A. C., and Borges, C. P., 1999, “Membrane Formation Mechanism Based on Precipitation Kinetics and Membrane Morphology Flat and Hollow Fiber Polysulfone Membranes,” Journal of Membrane Science, Vol. 155, pp. 171-183.

[Mahoney2005] Mahoney, M. J., Chen, R. R., Tan, J., and Saltzman, W. M., 2005, “The Influence of Microchannels on Neurite Growth and Architecture,” Biomaterial, Vol. 2005, pp. 771-778.

[Maskery2005] Maskery, S., and Shinbrot, T., 2005, “Deterministic and Stochastic Elements of Axonal Guidance,” Annual Review of Biomedical Engineering, Vol. 7, pp. 187-221.

[McKelvey1997] McKelvey, S. A., Clausi, D. T., and Koros, W. J., 1997, “A Guide to Establishing Hollow Fiber Macroscopic Properties for Membrane Applications,” Journal Membrane Science, Vol. 124, pp. 223-232.

[Menut2008] Menut, P., Su, Y. S., Chinpa, W., Pochat-Bohatier, C., Deratani, A., Wang, D. M., Huguet, P., Kuo, C. Y., Lai, J. Y. and Dupuy, C., 2008, “A Top Surface Liquid Layer during Membrane Formation Using Vapor-Induced Phase Separation (VIPS) — Evidence and Mechanism of Formation,” Journal of Membrane Science, Vol. 310, pp. 278-288.

[Miller2001] Miller, C., Shanks, H., Witt, A., Rutkowski, G., and Mallapragada, S., 2001, "Oriented Schwann Cell Growth on Micropatterned Biodegradable Polymer Substrates," Biomaterials, Vol. 22, pp. 1263-1269.

[Mortimer2008] Mortimer, D., Fothergill, T., Puhic, Z., Richards, L. J., and Goodhill, G., 2008, "Growth Cone Chemotaxis," Trends In Neurosciences, Vol. 31, pp. 90-98.

[Mulder1996] Mulder, J., 1996, *Basic Principles of Membrane Technology*, Kluwer Academic Publishers, The Netherland.

[Ngo2003] Ngo, T. B., Waggoner, P. J., Romero, A. A., Nelson, K. D., Eberhart, R. C., and Smith, G. M., 2003, "Poly(L-Lactide) Microfilaments Enhance Peripheral Nerve Regeneration across Extended Nerve Lesions," Journal of Neuroscience Research, Vol. 72, pp. 227-238.

[Nijdam2005] Nijdam, W., de Jong, J., van Rijn, C. J. M., Visser, T., Versteeg, L., Kapantaidakis, G., Koops, G. –H., and Wessling, M., 2005, "High Performance Micro-Engineered Hollow Fiber Membranes by Smart Spinneret Design," Journal of Membrane Science, Vol. 256, pp. 209-215.

[O'Toole2008] O'Toole, M., Lamoureux, P., and Miller, K. E., 2008, "A Physical Model of Axonal Elongation: Force, Viscosity, and Adhesions Govern the Mode of Outgrowth," Biophysical Journal, Vol. 94, pp. 2610-2620.

[Pereira2000] Pereira, C. C., Nobrega, R., and Borges, C. P., 2000, “Spinning Process Variables and Polymer Solution Effects in the Die-Swell Phenomenon during Hollow Fiber Membranes Formation,” Brazilian Journal of Chemical Engineering, Vol. 17, pp 599-606.

[Pfister2007] Pfister, L. A., Papaloizos, M., Merkle, H. P., and Grander, B., 2007, “Nerve Conduits and Growth Factor Delivery in Peripheral Nerve Repair,” Journal of the Peripheral Nervous System, Vol. 12, pp. 65-82.

[Rajnicek1997] Rajnicek, A. M., Birtland, S., and McCaig, C. D., 1997, “Contact Guidance of CNS Neurites on Grooved Quartz: Influence of Groove Dimensions, Neuronal Age and Cell Type,” Journal of Cell Science, Vol. 110, pp. 2905-2913.

[Recknor2004] Recknor, J. B., Recknor, J. C., Sakaguchi, D. S., Mallapragada, S. K., 2004, “Oriented Astroglial Cell Growth on Micropatterned Polystyrene Substrates,” Biomaterials, Vol. 25, pp. 2753-2767.

[Rios1994] Rios, E. H., Aravena, M. H., and Barraza, R. G., 1994, “Amphipathic Polyelectrolytes at the n-Octane/Water Interface,” Journal of Colloid and Interface Science, Vol. 165, pp. 259-263.

[Rutkowski2004] Rutkowski, G. E., Miller, C. A., Jeftinija, S., and Mallapragada, S. K., 2004, “Synergistic Effects of Micropatterned Biodegradable Conduits and Schwann Cells on Sciatic Nerve Regeneration,” Journal of Neural Engineering, Vol. 1, pp. 151-157.

[Santoso2006] Santoso, Y. E., Chung, T. S., Wang, K. Y., and Weber, M., 2006, “The Investigation of Irregular Inner Skin Morphology of Hollow Fiber Membranes at High-Speed Spinning and the Solutions to Overcome It,” Journal Membrane Science, Vol. 282, pp. 383-392.

[Schmidt2003] Schmidt, C. E., and Leach, J. B., 2003, “Neural Tissue Engineering: Strategies for Repair and Regeneration,” Annual Review of Biomedical Engineering, Vol. 5, pp. 293-347.

[Shi2007] Shi, L., Wang, R., Cao, Y. M., Feng, C. S., Liang, D. T., and Tay, J. H., 2007, “Fabrication of Poly (Vinylidene Fluoride-co-Hexafluropropylene) (PVDF-HFP) Asymmetric Microporous Hollow Fiber Membranes,” Journal Membrane Science, Vol. 305, pp. 215-225.

[Slavtchev2006] Slavtchev, S., Kurteva, P. K., and Mendes, M. A., 2006, “Marangoni Instability of Liquid-liquid Systems with a Surface-Active Solute,” Colloids and Surfaces A, Vol. 282, pp. 37-49.

[Somasundaran2006] Somasundaran, P., and Hubbard, A. T., 2006, *Encyclopedia of Surface and Colloid Science*, Taylor & Francis.

[Song2008] Song, J., Jiang, H., Liu, Z. J., Khang, D. Y., Huang, Y., Rogers, J. A., Lu, C., and Koh, C. G., 2008, "Buckling of A Stiff Thin Film on A Compliant Substrate in Large Deformation," International Journal of Solids and Structures, Vol. 45, pp. 3107-3121.

[Sørensen1977] Sørensen, T. S., Hennenberg, M., and Sanfeld, A., 1977, "Deformational Instability of a Plane Interface with Perpendicular Linear and Exponential Concentration Gradients," Journal of Colloid and Interface Science, Vol. 61, pp. 62-76.

[Sørensen1978] Sørensen, T. S., Hennenberg, M., and Hansen, F. Y., 1978, "Deformational Instability of a Plane Interface with Transfer of Matter," Journal of The Chemical Society-Faraday Transactions II, Vol. 74, pp. 1005-1018.

[Spillman2007] Spillman, J., and Teschner, M., 2007, "CORDE: Cosserat Rod Elements for the Dynamic Simulation of One-Dimensional Elastic Objects," Proc. Eurographics/ ACM SIGGRAPH Symposium on Computer Animation, San Diego, USA, pp. 209-217.

[Sternling1959] Sternling, C. V., and Scriven, L. E., 1959, "Interfacial Turbulence: Hydrodynamic Stability and the Marangoni Effect," AIChE Journal, Vol. 5, pp. 514-523.

[Su2007] Su, Y., 2007, "Theoretical Studies of Hollow Fiber Spinning," Ph.D. thesis, The University of Toledo, Toledo, OH, USA.

[Taylor2005] Taylor, A. M., Blurton-Jones, M., Rhee, S. W., Cribbs, D. H., Cotman, C. W., and Jeon, N. L., 2005, "A Microfluidic Culture Platform for CNS Axonal Injury, Regeneration and Transport," Nature Methods, Vol. 2, pp. 599-605.

[Tessier-Lavigne1996] Tessier-Lavigne, M., and Goodman, C. S., 1996, "The Molecular Biology of Axon Guidance," Science, Vol. 274, pp. 1123-1133.

[Timoshenko1961] Timoshenko, S. P., 1961, *Theory of Elastic Stablity*, McGreaw-Hill, New York, USA.

[Timoshenko1970] Timoshenko, S. P., and Goodier, J. N., 1970, *Theory of Elasticity*, Third Edition, McGraw-Hill, New York, USA.

[Tresco2000] Tresco, P. A., 2000, "Tissue Engineering Strategies for Nervous System Repair," Progress in Brain Research, Vol. 128, pp. 349–363.

[Trinkaus1985] Trinkaus, J. P. 1985, "Further Thoughts on Directional Cell Movement during Morphogenesis," Journal of Neuroscience Research, Vol. 13, pp. 1-19.

[Tsai2001] Tsai, H. A., Huang, D. H., Ruaan, R. C., and Lai J. Y., 2001, "Mechanical Properties of Asymmetric Polysulfone Membranes Containing Surfactant as Additives," Industrial & Engineering Chemistry Research, Vol. 40, pp. 5917-5922.

[Tsai2006] Tsai, H. A., Kuo, C. Y., Lin, J. H., Wang, D. M., Deratani, A., Pochat-Bohatier, C., Lee, K. R., and Lai, J. Y., 2006, "Morphology Control of Polysulfone Hollow Fiber Membranes via Water Vapor Induced Phase Separation," Journal of Membrane Science, Vol. 278, pp. 390-400.

[Valkovska2000] Valkovska, M. S., and Danov, K. D., 2000, "Determination of Bulk and Surface Diffusion Coefficients from Experimental Data for Thin Liquid Film Drainage," Journal of Colloid and Interface Science, Vol. 223, pp. 314-316.

[van Veen1994] van Veen, M. P., and van Pelt, J., 1994, "Neuritic Growth Rate Described by Modeling Microtubule Dynamics," Bulletin of Mathematical Biology, Vol. 56, pp. 249-273.

[Vasconcelos2000] Vasconcelos, B. C. E., and Gay-Escoda, C., 2000, "Facial Nerve Repair with Expanded Polytetrafluoroethylene and Collagen Conduits: An Experimental Study in the Rabbit," Journal of Oral and Maxillofacial Surgery, Vol. 58, pp. 1257-1262.

[von Gottberg1995] von Gottberg, F. K, Hatton, T. A., Smith, K. A., 1995, "Surface Instabilities Due to Interfacial Chemical Reaction," Industrial and Engineering Chemistry Research, Vol. 34, pp. 3368-3379.

[Wang2009] Wang, X., Zhang, L., Sun, D., An, Q., and Chen, H., 2009, "Formation Mechanism and Crystallization of Poly(Vinylidene Fluoride) Membrane via Immersion Precipitation Method," Desalination, Vol. 236, pp. 170-178.

[Wang2010] Wang, S., and Cai, L., 2010, "Polymers for Fabricating Nerve Conduits," International Journal of Polymer Science, Vol. 2010, pp. 138686.

[Weh2004] Weh, L., and Venthur, A., 2004, "Evolution of Fractal-Like Surface Structures in Layers of Polyacrylonitrile Solutions by Interfacial Dynamic Processes," Journal of Colloid and Interface Science, Vol. 271, pp. 407-415.

[Wen2006] Wen, X., and Tresco, P. A., 2006, "Effect of Filament Diameter and Extracellular Matrix Molecule Precoating on Neurite Outgrowth and Schwann Cell Behavior on Multifilament Entubulation Bridging Device in Vitro," Journal of Biomedical Materials Research: Part A, Vol. 76, pp. 626-37.

[Wu2006] Wu, L. S., Sun, J. F., and Wang, Q. R., 2006, "Poly (vinylidene fluoride)/Polyethersulfone Blend Membranes: Effects of Solvent Sort, Polyethersulfone and Polyvinylpyrrolidone Concentration on Their Properties and Morphology," Journal of Membrane Science, Vol. 285, pp. 290-298.

[Yang2005] Yang, F., Murugan, R., Wang, S., and Ramakrishna, S., 2005, “Electrospinning of Nano/Micro Scale Poly (L-Lactic Acid) Aligned Fibers and Their Potential in Neural Tissue Engineering,” Biomaterials, Vol. 26, pp. 2603–2610.

[Zhang2005] Zhang, N., Zhang, C., and Wen, X., 2005, “Fabrication of Semi-Permeable Hollow Fiber Membranes with Highly Aligned Texture for Nerve Guidance,” Journal of Biomedical Materials Research, Part A, Vol. 75, pp. 941-949.

[Zheng1991] Zheng, J., Lamoureux, P., Santiago, V., Dennerll, T., Buxbaum, R., and Heidemann, S. R., 1991, “Tensile Regulation of Axonal Elongation and Initiation,” The Journal of Neuroscience, Vol. 11, pp. 1117-1125.

[Zhou2009] Zhou, F., Yuan, L., Huang, H., and Chen, H., 2009, “Phenomenon of ‘Contact Guidance’ on the Surface with Nano-Micro-Groove-Like Pattern and Cell Physiological Effects,” Chinese Science Bulletin, Vol. 54, pp. 3200-3205.

[Zupan2009] Zupan, E., Saje, M., and Zupan, D., 2009, “The Quaternion-Based Three-Dimensional Beam Theory,” Computer Methods in Applied Mechanics and Engineering, Vol. 198, pp. 3944-3956.